Design and Fabrication of Immunomodulatory Hydrogels for Regenerative Medicine

Sepideh Mohammadi

Department of Mechanical Engineering

McGill University

Montréal, Canada

August 2022

A dissertation submitted to McGill University in partial fulfillment of the requirements for the degree of Doctor of Philosophy

To the victims of flight PS752, who will never be forgotten · · ·

Abstract

Macrophages are centrally involved in wound healing, angiogenesis, tumor growth, and the restoration of a full organ in certain species. Following tissue damage, macrophages regulate tissue homeostasis through the activation of other immune cells in the site of injury, the phagocytosis of pathogens and dead cells, and the production of various cytokines and growth factors. The main objective of the present study was to design biomaterials to control macrophage polarization and enhance healing. Over the past decades, several studies have shown the importance of anti-inflammatory drugs, scaffold chemistry, mechanical features, topographical cues, and porosity in modulating the immune response towards favorable macrophage response following implantation. However, there exist long-standing challenges that hinder their translation into practical use. Challenges include the lack of interconnected micropores to promote cell ingrowth, the often invasive nature of delivery procedures, and harsh synthesis conditions that are incompatible with drug molecules. These limitations are addressed here through the use of multiphase hydrogels. The two approaches are (1) Development of injectable microgels for the modulation of macrophage activation through the sustained release of cytokine molecules; (2) Development of injectable micropore-forming hydrogels for the modulation of macrophage activation through a cytokine-free approach. The microgels were synthesized following a water-oil emulsion approach with well-defined shapes, dispersity, and tissue-mimetic stiffness. The incorporation of Laponite into the microgels enabled a tunable degradation rate and sustained drug delivery. The Laponite-loaded microgels were effective in attracting macrophages as well as promoting fibroblasts spreading, motility, and proliferation. The sustained, bioactive release of interleukine-10 regulated the activation of co-cultured macrophages while counteracting collagen production by the fibroblasts, thereby inhibiting fibrosis formation. Injectable, pore-forming double-network hydrogels were fabricated using stepwise gelation consisting of two sequential phase separation and crosslinking processes. Scaffolds fabricated from two natural biopolymers presented tissue mimetic stiffness and interconnected porosities, with pore diameters that could be varied by changing the concentration of the starting polymer gel and crosslinker. The porous

matrices supported fibroblast spreading and proliferation along with anti-inflammatory macrophage polarization. Their unique composition and rapid gelation allowed the structured hydrogels to achieve strong tissue adhesion and promoted rapid hemostasis following tissue injury. These new injectable microporous hydrogels constitute promising cell-instructive systems for tissue regeneration applications.

Résumé

Les macrophages jouent un rôle central dans la cicatrisation des plaies, l'angiogenèse, la croissance tumorale et la restauration d'un organe complet chez certaines espèces. Suite à des lésions tissulaires, les macrophages régulent l'homéostasie tissulaire en activant d'autres cellules immunitaires sur le site de la blessure, la phagocytose des agents pathogènes et des cellules mortes et la production de diverses cytokines et facteurs de croissance. L'objectif principal de la présente étude est de concevoir des biomatériaux pour contrôler la polarisation des macrophages afin d'améliorer la guérison. Au cours des dernières décennies, plusieurs études ont montré l'importance des anti-inflammatoires, de la chimie de l'échafaudage, des caractéristiques mécaniques, des indices topographiques et de la porosité dans la modulation de la réponse immunitaire vers une réponse favorable des macrophages après l'implantation. Cependant, il existe des défis de longue date qui entravent leur traduction en utilisation pratique. Les défis comprennent un manque de micropores interconnectés pour favoriser la croissance cellulaire, des procédures d'administration invasives et des conditions de synthèse difficiles incompatibles avec les molécules médicamenteuses. Ces limitations sont abordées ici grâce à l'utilisation d'hydrogels multiphases. Les deux approches sont (1) Développement de microgels injectables pour la modulation de l'activation des macrophages par la libération prolongée de molécules de cytokines; (2) Développement d'hydrogels injectables formant des micropores pour la modulation de l'activation des macrophages par une approche sans cytokines. Les microgels ont été synthétisés selon une approche d'émulsion eau-huile avec des formes, une dispersité et une rigidité mimétique des tissus bien définies. L'incorporation de Laponite dans les microgels a permis un taux de dégradation réglable et une administration soutenue du médicament. Les microgels chargés de Laponite étaient efficaces pour attirer les macrophages ainsi que pour favoriser la propagation, la motilité et la prolifération des fibroblastes. La libération bioactive soutenue d'interleukine-10 a régulé l'activation des macrophages co-cultivés tout en neutralisant la production de collagène par les fibroblastes, inhibant ainsi la formation de fibrose. Des hydrogels à double réseau injectables et porogènes ont été fabriqués à l'aide d'une gélification par étapes consistant en deux processus

séquentiels de séparation de phase et de réticulation. Les échafaudages fabriqués à partir de deux biopolymères naturels présentaient une rigidité mimétique tissulaire et des porosités interconnectées, avec des diamètres de pores qui pouvaient varier en modifiant la concentration du gel polymère de départ et de l'agent de réticulation. Les matrices poreuses ont soutenu la propagation des fibroblastes, la prolifération ainsi que la polarisation des macrophages anti-inflammatoires. Leur composition unique et leur gélification rapide ont permis aux hydrogels structurés d'obtenir une forte adhérence tissulaire et ont favorisé une hémostase rapide après une lésion tissulaire. Ces nouveaux hydrogels microporeux injectables constituent des systèmes prometteurs d'instruction cellulaire pour des applications de régénération tissulaire.

Contributions and Claims of Originality

The current Ph.D. thesis aims to develop immunomodulatory hydrogels for improving tissue repair using two approaches. Therefore, each person's contributions are explained in the context of each approach.

The first approach was the development of injectable microgels for the modulation of macrophage activation through the sustained release of cytokine molecules. To accomplish this aim, S. Mohammadi and L. Mongeau conceived the idea and designed the study. S. Mohammadi developed the materials and method, conducted the experiments and analyzed the results. H. Ravanbakhsh helped with performing rheometry and live cell imaging. G. Bao performed atomic force microscopy, and S. Taheri helped with conducting microCT imaging and analysis. L. Mongeau supervised the project.

The second approach was the development of injectable micropore-forming hydrogels for the modulation of macrophage activation through a cytokine-free approach. For fulfilling this aim, S. Mohammadi, G. Bao, J. Li, and L. Mongeau conceived the idea and designed the study. S. Mohammadi and G. Bao developed the materials and methods. S. Mohammadi conducted the cellular experiments, physical characterization and degradation studies. G. Bao performed mechanical characterization and animal studies. S. Mohammadi and G. Bao analyzed the results. L. Mongeau was the supervisor of the project.

Acknowledgements

I would like to express my deep and sincere gratitude to my amazing Ph.D. supervisor, Prof. Luc Mongeau, for his kind support, guidance, constructive feedback, and encouragement during this project. His positive outlook and confidence in my research inspired me and gave me confidence. He provided me with the marvellous opportunity to earn several new skills, learn many new concepts, follow my interests and find my research path. I feel extremely fortunate to be part of his wonderful, multidisciplinary research group and to contribute to sharing ideas and creating knowledge and effective solutions under his supervision.

I am also deeply thankful to Prof. Jianyu Li (School of Mechanical engineering, McGill University) for his kind guidance, support, and motivation throughout my studies. I wish to show my appreciation to Prof. Albert Descoteaux (INRS Armand-Frappier Health and Biotechnology Centre) for his valuable comments on this project. I would like to thank Prof. Susan Thibeault (Department of Surgery, University of Wisconsin-Madison) for providing human vocal fold fibroblasts. I would also like to express my sincere gratitude to my PhD defence committee members.

Special thanks to Dr. Guangyu Bao for his invaluable friendship and treasured support, which was really influential in shaping my experiments and critiquing my results. I would also like to extend my thanks to my other colleagues at McGill Biomechanics Research Laboratory and Laboratory of Biomaterials Engineering, including Huijie Wang, Hossein Ravanbakhsh, Sara Nejati, Huiyu (Bella) Chen, Swen Groen, Sareh Taheri, Alicia Reyes, Pooya Saberi, Aria Hajiahmadi, Kaustuv Basu, Zixin He, Abigail Vikstorm, Mitchell Strong, Xuan Li, Yin Liu, Shuaibing Jiang, Zhenwei Ma, and Zhen Yang.

This research would not have been possible without the generous support of various funding agencies, including the National Institutes of Health (NIH), Natural Sciences and Engineering Research Council (NSERC), McGill Engineering Doctoral Award (MEDA), and

Fonds de recherche du Québec - Nature et technologies (FRQNT). The content is solely the responsibility of the authors and does not necessarily represent the official views of the National Institutes of Health. I would also like to thank the Advanced Bioimaging Facility (ABIF, McGill University), the Facility for Electron Microscopy Research (FEMR, McGill University), the McGill Institute of Advanced Materials (MIAM), and the McGill Center for Materials Characterization (MMC) for providing access to their facilities.

My warm and heartfelt thanks go to my parents, Ali and Shokouh, whose constant love and unconditional support keep me motivated and confident to follow my dreams. My accomplishments and success are because they believed in me. Hats off to my brother, Babak, for being there for me as far back as I can remember till today, for keeping me grounded, reminding me of what is important in life, and for paving the way for my adventures. I owe my deepest gratitude to Milad, my best friend, for always listening to my concerns and complaints, for doing everything to help me even after long days at work, and for cracking jokes during difficult times. Finally, I would like to thank my lovely cat, Ms. Shadow, for keeping me company during the many hours of the writing process at my apartment.

Abbreviations

^{1}H-NMR proton nuclear magnetic resonance

2D two dimensional

3D three dimensional

APS Ammonium persulfate

BSA bovine serum albumin

DI deionized

DMEM Dulbecco's Modified Eagle Medium

DMSO dimethyl sulfoxide

ECM extracellular matrix

EDX energy dispersive x-ray analysis

FBS fetal bovine serum

GelMA gelatin methacrylamide

Gel-PSN gelatin-based porous single-network

HAMA hyaluronic acid methacrylamide

HM hybrid microgel

HNM hybrid nanocomposite microgel

HVFF human vocal fold fibroblast

IL-10 interleukine-10

MEM minimum essential medium

MMP matrix metalloproteinase

mTG microbial transglutaminase

MTT 3-(4,5-dimethylthiazol-2-yl)-2,5-diphenyl-2H-tetrazolium bromide

NDN nanoporous double-network hydrogel

NSN non-porous single-network

PBS phosphate-buffered saline

PDN porous double-network

PEO polyethylene oxide

PMA Phorbol 12-myristate 13-acetate

PM Pure microgel

PS phosphate solution

PSN porous single-network

RGD arginine-glycine-aspartic

SC sodium bicarbonate

SEM scanning electron microscopy

TCP tissue culture plate

TEMED tetramethylethylenediamine

TGF-β1 transforming growth factor-beta 1

μCT micro-computed tomography

Table of Contents

List of Figures

List of Tables

Chapter 1 Introduction

The present chapter consists of four sections. First, the thesis organization and the arrangement of the chapters are described. Second, the problem of interest is stated. The barriers that hinder the clinical applications of the current immunomodulatory hydrogels and the rationale for the present study to overcome the stated obstacles are introduced. Third, a comprehensive review of the previous relevant studies is presented. Finally, the hypothesis underlying the project and the specific aims of the thesis are elaborated. The sentences in quotations are verbatim of the author's publications (reference [1]).

1.1 Thesis organization

This study is structured in five chapters, including the introduction, methods, results and discussion, and conclusion. Chapter 1 begins by explaining the rationale for studying the problem of interest, continuing with a comprehensive review of the available literature. It is then followed by revealing the challenges in the field of immunotherapy and immunomodulatory biomaterials and proposing solutions to address those obstacles. The literature survey section is further divided into four main subsections. In the first subsection, the wound healing process, scarring, and its effect on tissue integrity are discussed in a review of previous studies. In the second part, the roles of diverse macrophage populations in tissue repair and fibrosis is described. Anti-fibrosis role of interleukine-10 (IL-10) for efficient tissue regeneration is then discussed. Specifically, recent advances in immunomodulatory biomaterials for attenuating scarring and fibrosis are summarized. The last part of the literature survey provides an overview of how the immune system reacts to an implant and the tailoring of biomaterials for migrating foreign body responses. Lastly, the scope of the thesis is clarified by articulating the thesis's specific aims.

Chapter 2 provides information on the experimental methods used throughout this study. The experimental methods are classified into material synthesis, non-biological methods, and biological methods depending upon whether cells, tissues, or animals were used in the experiment.

The non-biological experiments comprise nuclear magnetic resonance (NMR) spectroscopy, scanning electron microscopy (SEM), rheometry, atomic force microscopy (AFM), swelling tests, biodegradation assays, pore size measurement, zeta potential measurement, and Elisa analysis, while the biological tests include cell culture, viability, adhesion, migration, differentiation, collagen production, tissue adhesion, and hemostasis. The details of statistical analysis and image processing methods are also explained in this chapter.

In chapter 3, the results pertaining to hybrid nanocomposite microgels (HNMs) are presented, including their physical properties, structural features, rheological behavior, drug release profile, and biological interactions with living cells. Initially, the effect of Laponite nanoparticles on the structural, mechanical, and drug release properties of the microgels is studied. “It is demonstrated that the porous interstitial spaces between microgels promote fibroblast proliferation and fast trafficking. The incorporation of hyaluronic acid further enhances macrophage infiltration.” The effects of loading IL-10 in Laponite nanoparticles on attenuating scar-like collagen production through polarizing co-cultured macrophages are assessed.

The results related to the porous double-network gels (PDNs) are presented in Chapter 4. Therein, microstructure features that were used for optimizing the fibroblast spreading and proliferation are discussed. The porous structure is shown to enhance adhesion and pro-healing phenotype differentiation of encapsulated macrophages. The adhesion performance and hemostasis capability of the PDNs are further demonstrated through adhesion energy testing and the rat tail bleeding model.

Chapter 5 summarizes the main results and emphasizes the conclusions of the thesis. The contributions to the knowledge in the field of immunomodulatory biomaterials and regenerative medicine are clarified, and a comprehensive discussion on the perspective and the future direction of biomaterial-based immunotherapy for improved wound healing is presented.

1.2 Motivation

“Wound healing governs tissue repair following different injuries, including heart attack, spinal cord injury, skin burn, and gunshot wounds. Similarly, scarring tissue that may form during the wound healing process causes dysfunctions wherever it happens [2-4].” Scarring and tissue fibrosis have become a significant cause of depression, disability, and mortality worldwide. Treatments for promoting wound healing while preventing scar formation are critically needed in healthcare but remain long-standing challenges. Several studies have confirmed the regulating effect of the immune system on the healing response of different tissues to injury, including the extent of scarring and the recovery of the organ structure and function. In lower vertebrates, an intact immune system is needed for the restoration of various body parts such as the salamander limb, zebrafish fin, and zebrafish heart. Moreover, the ability of scar-less wound healing has been well documented in all mammalian embryos studied to date. This ability is lost as the immune system develops and the fetus approaches late gestation. The postnatal mammals are unable to completely regenerate damaged tissue except for the bone, liver, and mucosal sites. There are also numerous differences among the inflammatory responses of scar-less wound healings and wound healings leading to scar formation in mammalian adults. “Therefore, the modulation of immune responses via biomaterials and drug delivery systems is becoming a very plausible strategy for supporting current regenerative therapies or being used as an alternative to stem cells and growth factors [5-7].”

Within the basic paradigm of tissue engineering, cells play the central role in generating the new tissue by producing various growth factors, proteinases, chemokines, cytokines, and extracellular matrix (ECM) components. A highly porous scaffold with an interconnected network of microscopic pores is needed to facilitate cell infiltration, maintain cell viability, enable nutrient and waste diffusion, and ultimately promote connected tissue growth. The cells would produce their own ECM and secrete enzymes to degrade the biomaterial simultaneously, therefore promoting cells self-assembly into neonatal tissue and the merging of the neonatal tissue to the original injury site [8]. “In contrast, Nanoporous gels provide only a limited diffusion layer

thickness (~600 μm) for oxygen and nutrients, thereby hindering cellular infiltration and mobility." This limits the depth of tissue regeneration to a few millimetres at best, hampering applications for deep wounds [9]. Material delivery may also affect the biomaterial's functionality and could possibly restrict their clinical applications. Tissue damage during insertion surgery creates the initial wave of inflammatory response attracting cells to the injury site. The adsorbed extravasated blood proteins provide the first cell-interacting layer on the implant. Therefore, there is a direct relationship between implantation trauma and the degree of foreign body response (FBR) [10, 11]. While implantation trauma is not entirely avoidable, one of the most successful approaches to reduce FBR is to design biomaterials that are well suited for insertion. In this regard, injectable hydrogels that can be implanted minimally invasive, yet provide a tissue-like microenvironment for new tissues' growth and restore the shape and size of irregular cavities, are advantageous for regenerative therapies [12]. As a result, the first objective of this study was to develop biocompatible multiphase hydrogel systems that enable the *in situ* formation of a biodegradable scaffold while simultaneously generating microporous structure within the injection site.

Injectable porous hydrogels may be designed to allow local delivery of immunomodulatory drugs due to their ease of delivery and uniform tissue-like three-dimensional (3D) network [13]. "But these hydrogels have a mesh size larger than a typical protein molecule. Because of this, the protein has a weak interaction with the hydrogel polymer backbone, leading to fast diffusion and burst release [14]." The sustained release of drug molecules is usually achieved by stabilizing a polymer network, followed by either encapsulation into another polymer phase or covalent conjugation to the polymer backbone. The drug molecules are thereby vulnerable to harsh conditions and crosslinking chemistries. "Although these strategies offer controlled protein release, the crosslinking chemistries can crossreact with encapsulated proteins, and the required harsh conditions may result in a bioactivity loss of proteins." In the next phase of this research, we incorporated Laponite nanoparticles within the polymeric network of granular hydrogels to provide the sustained release of bioactive drug molecules. A novel hybrid nanocomposite microgel

system was designed and fabricated to modulate macrophage phenotype through sustained release of an immunomodulatory agent.

Recent studies have shown the importance of either mechanical features or environmental confinement in modulating the response of immune cells. The fabricated porous structures are designed and performed in-vitro prior to cell incorporation or transplantation into the body and require forming into the shape and size of the implantation site. They are not amenable to the encapsulation of cells and bioactive agents due to the harsh processing condition and toxic raw chemicals used in their fabrication [15]. On the other hand, pure hydrogels are usually too soft and weak for applications as scaffolds for load-bearing tissue regeneration. Their weakness is exacerbated in injectable gels relative to preformed hydrogels [16]. In the past decades, great attention has been devoted to reinforcing the mechanics of injectable hydrogels through the inclusion of fibril components, inorganic nanomaterials, and the employment of double-network design. Specifically, double-network hydrogels exhibit exceptional mechanical toughness by building a dissipative network within a stretchy network. Such materials are developed in a way that a brittle dissipative network can break to deconcentrate stress throughout the network while a ductile, coiled network endures large deformation [17]. A new biofabrication method that addresses the above-mentioned issues and satisfies the tissue adhesiveness and hemostasis requirements is constituted the last phase of the present work. Therein, the design and performance of an injectable porous double network gel with immune regulating properties are reported.

1.3 Literature survey

1.3.1 Wound healing, scarring, and fibrosis

Wound healing is a biological process that takes place after injury. It consists of four connected and overlying phases: 1) homeostasis; 2) inflammation; 3) proliferation (in which scar may form); 4) Remodelling (**Figure 1-1**)[17]. Immediately after an injury, hemostasis begins with vascular constriction and fibrin clot formation. The injury site is occupied with tissue debris, fluid, and clotted blood. The strength of the wound closure depends mostly on fibrin. It is often

insufficient to bond the sides of the wound together. Mechanical methods such as sutures must be utilized to close the wound. The clot and surrounding tissue release pro-inflammatory cytokines and various growth factors [2, 18, 19].

Once bleeding is controlled, symptoms of inflammation, such as redness, swelling, heat, and pain, appear. The dilatation of vessels and the associated increased vessel wall permeability create edema and allow inflammatory cells to infiltrate the wound area. Polymorphonuclear cells support the defence against bacteria, while macrophages remove the debris and regulate the inflammatory response during wound healing. Near the end of this phase, perivascular mesenchymal cells differentiate into fibroblasts and migrate into the injury site. Some collagenous components can be observed in this phase and following a couple of days of injury [18, 20].

The production of ECM generally begins after the inflammation subsides and during the proliferation phase. This additional matrix deposition results in the formation of new red, granular connective tissue on the surface of the wound. This so-called granulation tissue consists of endothelial cells, fibroblasts, macrophages, differentiated from blood monocytes and tissue-resident macrophages, and connective ECM components. Granulation tissue formation allows epithelial cells to migrate across the new tissue and the initiation of reepithelialization. The endothelial cells contribute to angiogenesis, while the fibroblasts and epithelial cells lay down new collagen, elastin, fibronectin, and glycosaminoglycans such as hyaluronic acid. As old damaged collagen is enzymatically degraded, new collagen is synthesized with a peak period around the fifth to the seventh day of healing. Collagen fibrils are first deposited with random orientation, therefore they possess little mechanical strength. Little by little, enzymatic crosslinking stabilizes the microfibrils into fibrils which are later assembled into fibers. The collagens gradually acquire a more systematic pattern and higher mechanical strength. The production and breakdown of connective tissue elements reach an equilibrium after around two to three weeks. The number of fibroblasts and macrophages diminishes as the healing proceeds into the last phase [18, 21-23].

The remodelling phase and the transition from immature scar to mature scar occur after robust proliferation and ECM synthesis anywhere between six months and one year after wounding. During this phase, The ECM undergoes continuous remodelling to conform to the native tissue architecture, although the regularity of the original fiber structure in normal tissue is never fully recovered. The scar tissue consists of dense connective tissue in which collagen fibers dominate. The collagen content does not increase anymore, but the fibrils continue their maturation. They increase in diameter, which parallels an increase in mechanical strength, although less rapidly than during the proliferation phase. The prevalence of collagen type I formation over collagen type III might also contribute to an increase in strength. Furthermore, many of the newly formed capillaries regress to regain a normal vascular density. Wound contraction happens during all stages of wound healing. It is largely mediated by myofibroblasts. The remodelling process is highly sensitive to mechanical (stretching) stimuli, and the collagen fiber pattern aligns in the direction of the applied stresses [18, 24, 25].

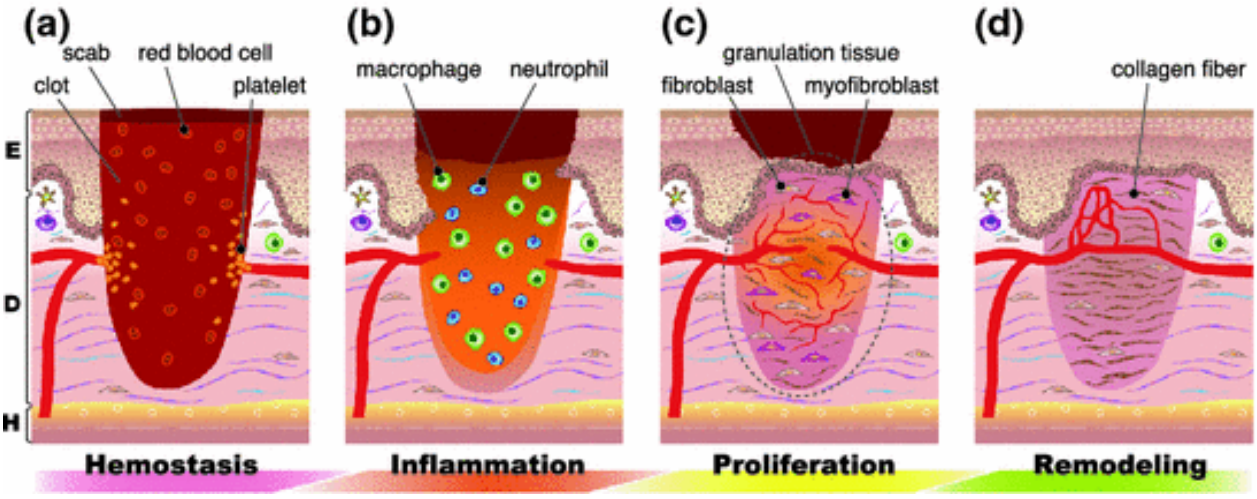

Figure 1-1 Schematic illustration of four phases of wound healing, including a) hemostasis, b) inflammation, c) proliferation, and d) remodelling; Reprinted from [26]; An open-access article distributed under the terms of the Creative Commons Attribution License (CC BY).

The formation of a scar is the most common consequence of soft tissue injury upon incisional wound healing in soft tissue. Scars consist of dense connective tissue. The major constituents of scar do not differ substantially from tissue to tissue [27]. On the other hand, the degree of vascularization and functional properties of scar-tissue combination are very different from one tissue to another and determine the healing rate. [18, 28, 29]. The main purpose of the wound-healing process following a soft tissue injury is to bridge the wound edges to close the wound. This takes place in mammals by filling the opening with a scar of collagenous connective tissue [18]. Optical coherence tomography of skin wounds following 30 days of healing revealed a bridge-like structure that extends above and below the neighboring fat layer and integrates with the intact dermis and muscle tissues [30, 31]. This di-fork structure creates superior stress-buffering to the underlying tissues. This reflects scar intelligence to compensate for the loss of hypodermis and muscle tissue by developing into a di-fork [32, 33].

Pulmonary fibrosis is a lung disease in which scar formation leads to the progressive and irreversible destruction of lung tissue. This thickened, stiff tissue eventually results in the interruption of gas exchange and organ failure [34-36]. While both the elastin and collagen contents increase during fibrosis, the viscoelastic properties of the lung are mainly dependent on the alterations in the content of collagen and proteoglycans [37, 38]. Due to their negative charge, Proteoglycans are greatly responsive to local osmolarity. They collapse and become inflated under hypertonic and hypotonic conditions, respectively. As a result, they impede the folding of collagen structures in the direction of applied strain providing the elasticity of the tissue [39]. Collagen deposition in fibrosis increases the fraction of stiff collagen fibers in clusters within a matrix of proteoglycans. When the fraction further increases, the collagen fibers spread into a network and form unbroken chains. The network adopts a homogeneous configuration to become increasingly heterogeneous over time [39, 40].

Due to their anatomic location and physiological function, the vocal folds are exposed to a wide range of harmful stimuli that may cause scarring. The formation of scar tissue significantly changes the composition and biomechanics of the ECM irreversibly and destroys the delicate tri-

layered micro-structure of the Lamina propria [3, 41]. According to histological findings, intact vocal fold tissue contains hyaluronic acid, elastin, and a parallel architecture of collagen fibers. As a result of scarring, the hyaluronic acid level significantly decreases [42, 43]. High density and organized elastin fibers will also be replaced by low density, fragmented, and disorganized fibers [44-46]. Tightly packed, chaotic, interwoven collagen fibers will be formed with the prevalence of collagen type I over collagen type III [47]. Collagen III fibrils have been found to possess a smaller average diameter and young moduli (50 nm, 200 kPa) compared to collagen I (200 nm, 1000 kPa) [48]. These collagen structures also show a difference in surface Young's moduli measured by atomic force microscope (AFM). This altered structure creates mucosal wave initiation/propagation abnormalities, resulting in hoarse, breathy, and little sustainable voice [49].

1.3.2 Macrophages in wound healing

"Monocytes and macrophages are key agents in tissue repair [50]. Following tissue damage, macrophages regulate tissue homeostasis by the activation of other immune cells at the site of injury, the phagocytosis of pathogens and dead cells, and the production of various cytokines and growth factors. Macrophages are critical for wound healing, angiogenesis, organ regeneration, and tumor growth. They may even help restore entire limbs, for example, in the salamander [51, 52]. Macrophages modulate fibrosis and scarring over different stages of wound healing through cell-cell and cell- ECM interactions [53]. A relatively small population of macrophages resides in most tissues in an inactivated state (M0). Larger cohorts are recruited after tissue injury through differentiation from circulating monocytes. The resident and recruited M0 macrophages proliferate and differentiate into a spectrum of subtypes ranging from the pro-inflammatory M1 to the anti-inflammatory M2 state that dynamically adjusts to microenvironmental signals. The M2 macrophages can be further sorted into M2a-c phenotypes [5] (**Figure 1-2**)."

The M1 phenotype, referred to as 'classically activated' macrophage, is typically induced by pro-inflammatory cytokines such as Interferon-γ (IFN-γ) and microbial products such as lipopolysaccharides. Crucial for the early stages of wound healing, M1 macrophages help to kill

the pathogens and propagate the initial response by secreting pro-inflammatory factors such as IL-1, IL-6, and TNF-α. They also release ROS at the injury site to degrade foreign material. Moreover, they are known to be responsible for initiating angiogenesis through the secretion of factors such as VEGF. However, their chronic activation leads to an escalation of the pro-inflammatory response, which harms neighboring cells and delays wound healing. In the case of biomaterial implantation, prolonged M1 activation results in chronic inflammatory events, granuloma, and fibrous encapsulation [7, 54, 55].

The M2 phenotype of macrophages, also known as 'alternatively activated,' emerges near the end of the inflammatory response and serves to resolve inflammation, promote healing and recover tissue homeostasis characterized by severe to no scar. The M2 macrophages are further categorized into subsets, including M2a, M2b, and M2c, based on the environmental stimuli and their main function [6, 51].

The M2a subtype, induced by IL-4/IL-13, consists of the pro-wound healing or pro-fibrotic macrophages. Together with M1, the M2a subtype plays a key role in the inflammatory phase of wound healing. They produce elevated levels of pro-inflammatory cytokines such as arginase-1 and Ym1 in the early stage. The M2a macrophages synthesize collagen precursors and TGF-β, which stimulates fibroblast collagen production. Moreover, M2a macrophages are capable of secreting factors such as IGF-1 and TIMP1. They produce certain ECM components such as collagen type VI and fibronectin. Thus, they contribute significantly to cellular proliferation and ECM synthesis, which is needed during the proliferative phase. They also express high amounts of PDGF, which is associated with the recruitment of pericytes for vessel maturation [55-58].

The M2b macrophages are produced by simultaneous exposure to immune complexes and Toll-like receptor/IL-1 receptor. During later stages of the proliferative phase, M2b mediated interleukine-10 (IL-10) release suppresses inflammation and stimulates M2c or pro-resolving macrophage activation. Recent studies on human burn wounds revealed that genes involved in M2c phenotype increase at later stages of injury (7-17 days), suggesting that M2c macrophages play a major role as they help in the last phase of wound healing. The M2c is the main regulator

of the remodelling phase and produces high levels of IL-10, different types of matrix metalloproteinase (MMP), and TGF-β. They perform many essential functions. They cease T cell proliferation, minimize fibrosis by inducing apoptosis of myofibroblasts, aid in collagen reorganization, promote vessel sprouting and remodelling, and restore the balance between MMP and tissue inhibitor of metalloproteinase (TIMP) and hence, bring back tissue homeostasis. Further investigations are still required to understand the exact functions and timing of the M2c phenotype in wound healing and tissue regeneration [55, 57, 59].

"Recent progress in methods for the controlled harnessing of local macrophages includes the design of biomaterial-based strategies for effective tissue regeneration. Long- and short-term release of immunomodulatory cytokines from a decellularized bone scaffold promoted sequential activation of M1 and M2 macrophages and directed their angiogenic behavior towards murine model vascularization [60]. The incorporation of an imidazole group into a synthetic hydrogel increased its interaction with the local macrophages via their histamine-receptor binding sites. Moreover, the activation of MMP produced by macrophages within the fibrotic ECM resulted in matrix remodelling and the complete regeneration of cystic cavities in a rat spinal cord injury model [61]."

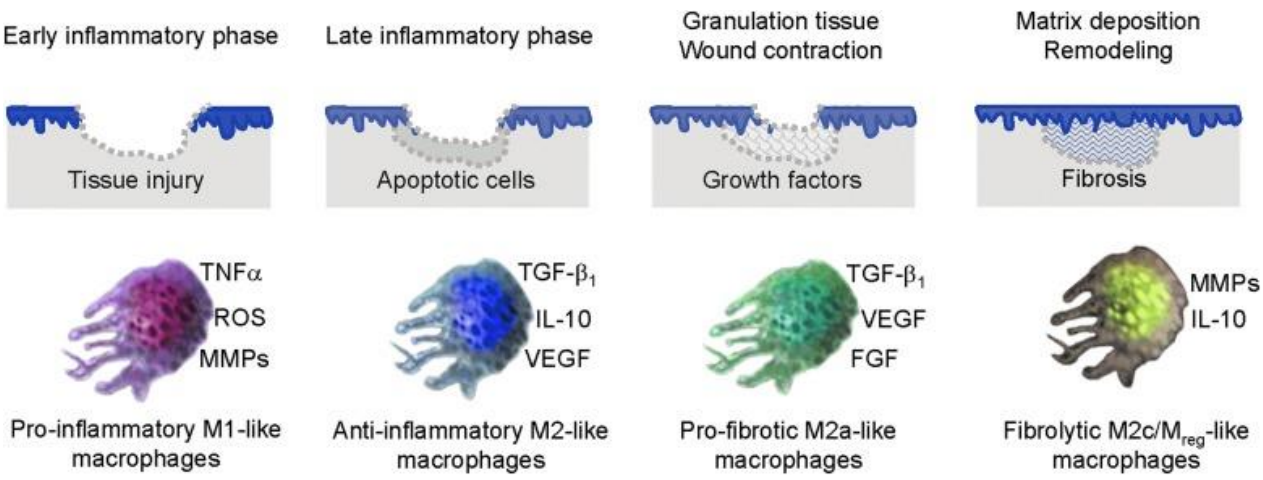

Figure 1-2 Schematic illustration of main macrophage phenotypes involved in wound healing; Reprinted from [62]; An open-access article distributed under the terms of the Creative Commons Attribution License (CC BY).

1.3.3 Interleukin-10 and its immunoregulatory effect in fibrosis

"During each stage of wound healing, transforming growth factor-beta 1 (TGF-β1) is released by different macrophage phenotypes, resulting in fibroblast attraction and differentiation into myofibroblasts. Acting as a double-edged sword, TGF-β1 promotes wound repair but may also result in scarring [63]. The cytokine IL-10, another crucial regulator of wound healing, is predominantly secreted by pro-regenerative macrophage type M2c [64]. On one hand, the secretion of IL-10 has been observed to diminish inflammatory response in the inflammatory phase within 3 h after injury. It has, on the other hand, prevented the further proliferation of myofibroblasts and collagen-I production in the proliferative phase 72 h after injury [65, 66]."

"The anti-fibrosis effect of IL-10 has previously been revealed both in animal experiments and in clinical trials, where IL-10 wound treatment lowers inflammatory reaction and leads to regeneration through scar-free healing [67]. *In vitro* co-culture models of human fibroblasts and macrophages with IL-10 have revealed inhibitory effects on pro-inflammatory cytokine production, deactivation, and even de-differentiating effects on myofibroblasts.[66] The range of activity of IL-10 is limited to its immediate vicinity. To ensure its rapid availability at the wound site [68], it is advantageous to enable neighboring immune cells to produce IL-10. But one major obstacle to using IL-10 in clinical application is the very short half-life (2.7 to 4.5 h) of its soluble homodimer *in vivo*. This is due to its high rate of degradation at acidic pHs or low protein concentrations commonly found in inflamed tissue [69]. Therefore, the modulation of the local immune cell population after injury through local delivery of IL-10 via implanted biomaterials is becoming a very plausible strategy for supporting current regenerative therapies or being used as an alternative to stem cells and growth factors [5]."

"In this regard, injectable hydrogels, a class of polymer scaffolds with tissue-like properties, are advantageous for the local delivery of IL-10 and the restoration of the shape of irregular cavities with minimal invasiveness. Bioactive hydrogels laden with IL-10 can reduce inflammation, promote angiogenesis, and prevent fibrosis in different tissues. For example, the physical

entrapment of IL-10 into gelatin-based hydrogels reduced the pro-inflammatory responses of macrophages and led to scar-less axon growth in a complete transaction mouse model [70]. IL-10-laden hyaluronic acid-based hydrogels reduced fibrosis in a murine model of chronic kidney disease [71]. But most hydrogels have a mesh size larger than the size of a typical protein molecule. Because of this, the protein has a weak interaction with the hydrogel polymer backbone, leading to fast diffusion and burst release [14]."

"One frequently used strategy to circumvent this drawback is to encapsulate proteins in another phase (e.g., polymeric microspheres), and then incorporate this phase into the main hydrogel. The loading of IL-10 into microgels and their release from the composite gel were found to improve scar thickness, cardiac function, and vascularization in a rat model with myocardial infarction [72]. Another approach is to conjugate the drug to the polymer. The reversible binding of IL-10 to a heparin-based hydrogel has prevented and even partially reversed lung fibrosis in a mouse model of bleomycin-induced lung injury [73]. The chemical crosslinking of IL-10 and another pro-resolving factor (AT-RvD1) with polyethylene glycol (PEG)-based hydrogel improved vascularization and increased the population of M2 macrophages and IL-10-producing dendritic cells in the mouse dorsal skinfold chamber [67]."

1.3.4 Foreign body response and design of immune-instructive biomaterials

The foreign body response (FBR) is a dynamic process of the local or systemic host response to the immunological rejection of implanted biomaterials [74] (**Figure 1-3**). The degree of the FBR is a decisive factor determining the biocompatibility of the biomaterial and depends on the degree to which the homeostasis of the host tissue was interrupted by the injury as well as the composition and structure of the introduced biomaterial [75]. Within seconds of biomaterial's insertion, plasma proteins become non-specifically adsorbed into the surfaces of the foreign body and form a matrix with dynamically changing composition, rich in growth factors and chemokines. Neutrophils can identify the formed matrix through complement activation and migrate into the

area within a few minutes. Neutrophils adhere to the protein layer and secrete factors that serially recruit monocytes to stimulate the progression of the inflammatory response [11, 76].

Monocytes begin to differentiate into M0 macrophages, which proliferate in the lesion site upon arrival. Within two days of implantation, the initial wave of neutrophils disappears, giving way to the macrophages to become central orchestrators of the innate immune response.[11] These macrophages become classically activated (M1) and self-maintain by proliferating and producing chemoattractants that recruit further monocytes and tissue-resident macrophages. The new population supports pathogen killing and propagation of the acute inflammatory response by producing reactive species such as nitric oxide (NO) and pro-inflammatory species such as tumor necrosis factor-α (TNF-α). After that, macrophages polarize to alternatively activate M2 macrophages that allow them to resolve the inflammation, promote healing and recover tissue homeostasis by producing high levels of IL-10 and TGF-β [11, 77].

Alternatively, the foreign material provokes a severe acute inflammatory response in which M1 macrophages continue to populate the area and begin to adhere and flatten over the free surfaces of the biomaterial. The bounded and activated macrophages release chemoattractive agents, which continue to recruit more macrophages and degrade the implanted material. However, the unsuccessful degradation of the foreign body by phagocytosis results in the fusion of macrophages into foreign body giant cells. Being unable to digest the bulky implanted material, macrophages instead secrete degrading enzymes and reactive oxygen species (ROS) in an effort to destroy the foreign body and instead phagocytose the resulting fragments [11, 76, 78]. Within 4–7 days after implantation, when macrophages fail to break down the implant, the inflammatory response transitions into its chronic stage in which macrophages switch from M1 to M2 phenotype [76, 78]. During FBR, however, M2 macrophages instead play a central role in forming a fibroblast-rich collagenous fibrous matrix around the biomaterial to stop the interactions between the implant surface and surrounding tissues [79]. This fibrous capsule hampers the exchanges of nutrients, oxygen, and wastes between the inserted material and host tissue. Also, it impedes the functionality of the controlled drug release devices and cell-bearing constructs [76]. Thus, the

extent and time frame of the inflammation response is highly detrimental to the outcome of the biomaterial-mediated tissue regeneration, in which macrophages play a pivotal role [79].

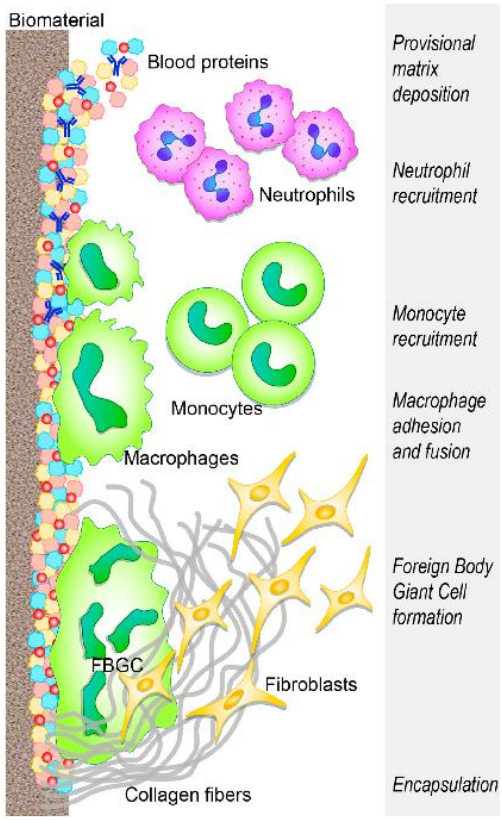

Figure 1-3 Schematic illustration of the development of the foreign body reaction to a biomaterial; Reprinted from[80]; An open-access article distributed under the terms of the Creative Commons Attribution License (CC BY).

Topographical cues, mechanical features, and porosity are also important factors. They modulate the immune response to the foreign implanted biomaterials, and they mitigate the FBR. Cells are able to sense biophysical cues and physical features of their microenvironment and adjust their activity through continuously remodelling their cytoskeleton. As an example, fibroblast contraction produces a dynamic force source in the matrix that induces and governs macrophage migration. Macrophages adapt to the physical features of their microenvironment by modifying cell shape and elasticity, which is closely tied to their phenotypes [81]. Harnessing these tools,

many research groups have investigated the effect of bulk properties, topographies, and geometries on macrophage behavior (**Table 1-1**).

Table 1-1 Mechanical property impacts on macrophage behavior (Adapted from [81] under the terms of the John Wiley and Sons license, license number: 5352850038953.)

Physical property modified	**Specific strategy**	**Observed effect**	**Refs.**
Material stiffness		Increasing stiffness (>100 kPa) increases inflammatory macrophage behavior.	[82-85]
		Ultrasoft (30 Pa) collagen gels induce inflammatory behavior in comparison to higher degree of crosslinking comparatives (100 Pa).	[86]
Surface Topography	Regular patterning	Nano- and micrograting of implant surface regulate macrophage cell shape. Smooth surfaces do not induce inflammasome activation. Elongated cell shape is associated with prohealing phenotype.	[87-91]
		Microstructured surface induced proinflammatory macrophage phenotype.	[92, 93]
	Random surface texture	Randomly nanotextured implant did not affect activation of macrophages.	[92]
		Random alignment induced macrophage/foreign body giant cell reactions in vivo. Rough surfaces upregulated M1 marker expression in macrophage and IL-1 secretion.	[91, 92, 94]

Implant Geometry	Implant size	Particle/sphere size can regulate macrophage phagocytosis. Smaller particles increased secretion of inflammatory molecules in vitro and macrophage infiltration in vivo.	[95-98]
	Fiber thickness	Fibers with diameters less than 6 μm induced small fibrous capsule formation.	[99, 100]
	Implant shape	Implant shape can regulate macrophage phagocytosis. Shapes with sharp edges increased degradative enzyme activity in vivo. Spherical implant minimized foreign body response.	[101-103]
	Pore size	Implant pore size could regulate vascularization and macrophage polarization.	[104-106]

Channeled two-dimensional (2D) substrates resulted in elongated macrophages with higher expression of CD206 and release of IL-4 compared to well-spread macrophages cultured on unpatterned substrates. Further studies showed the critical role of actin-associated contractility in the regulation of macrophage polarization by cell shape. Results also showed a correlation between M2 polarization and increased cell elongation [87]. The influence of substrate stiffness was evaluated on macrophage polarization through their 2D culture on polyacrylamide Hydrogels. Through modulating the ROS-initiated NF-κB pathway, soft substrates (2 kPa) promoted M1 activation along with the production of ROS and TNF-α, while stiffer gels (35 kPa) supported M2 polarization and production of more IL-4 and TGF-β. Subcutaneous delivery of the gels in a mouse

model also confirmed the presence of M1 cells around the hydrogels with low substrate stiffness with more M2 phenotype near the stiff gels [107].

The role of fiber and pore dimensions was investigated in the polarization of seeded macrophages on electrospun polydioxanone scaffolds. Results showed that increased fiber/pore size (from 0.35/1 um to 3/15 um) was linked with elevated expression of the M2 marker Arginase 1 as well as production of the angiogenic cytokines VEGF, bFGF, and TGF-b1. The same study also showed that the large fiber/pore size scaffolds polarize M1s to M2 phenotype through a MyD88-dependant mechanism [108]. In another study, freeze-dried collagen/chitosan scaffolds with various pore sizes were developed by changing the freezing regime. Scaffolds with an average pore size of 360 um exhibited a higher degree of M1-to-M2 transition and greater potential to promote angiogenesis *in vitro* and vascularization in a mouse subcutaneous transplantation compared to their counterparts with 160 um pore size [109].

The combined effects of pore size and stiffness on macrophage polarization were first investigated using gelatin cryogels. Macrophages within softer gels with small pores (20 kPa, 30 μm) exhibited the M1 phenotype, whereas the M2 phenotype was induced by stiffer matrixes with large pores (190 kPa, 80 μm). In a mouse model, the subcutaneous implantation of the gels showed that the greatest number of M1 macrophages and neutrophils occurred on day four within the scaffolds with soft and small pores. In contrast, scaffolds with large and stiff pores (190 kPa, 80 μm) showed the highest level of collagen deposition on day eight. These findings suggested that scaffolds with large and stiff pores could inhibit inflammation in the early stages but may later induce fibrosis during the healing process [110]. Using 3D printed scaffolds with various pore sizes and stiffness, the interplay between these two parameters was again investigated in macrophage polarization. In a rat subcutaneous model, soft scaffolds (<5 kPa) promoted M1 phenotype differentiation *in vitro* and chronic inflammation after six weeks of implantation. In contrast, stiffer (>40 kPa) scaffolds with similar porosities supported M2 macrophage activation *in vitro* and promoted tissue formation and vascularization *in vivo*. The introduction of pores with diameters between 10 and 20 um results in a polarization of cultured macrophages towards M2,

with the production of IL-10 and TGF-β. *In vivo* studies also showed a significant reduction in the thickness of a fibrotic capsule thickness with increasing porosity [79].

1.4 Research objectives

The main objective of the present study was to design and fabricate immune-regulating injectable microporous hydrogels using multiphase biomaterials to enhance their compatibility for regenerative medicine applications. To this end, hydrogels' formula, as well as their fabrication method, were designed and optimized. Specifically, Laponite was used as a drug carrier and a reinforcing agent to fabricate nanocomposite hydrogels, which were postulated to improve wound healing outcomes and scarring parameters. Furthermore, we propose a double network hydrogel system that enables cytokine-free modulation of the immune response. The feasibility and efficacy of the hydrogels were assessed through a set of cell viability, cell differentiation, and tissue interaction experiments. We envision that the outcome of this dissertation makes a significant contribution towards the clinical translation of immunomodulatory biomaterials. The specific aims of this project were defined as follows.

Specific aim 1: The first aim was the development of injectable microgels for the modulation of macrophage activation through the sustained release of cytokine molecules. A hybrid nanocomposite microgel (HNM) was designed based on three main criteria of sustained cytokine release, cytocompatibility, and macrophage attraction. The addition of Laponite could change the mechanical, physical, and drug release properties of the HNM. To evaluate the biological performance of the HNM, first, the peripheral effects of adding Laponite to the nanocomposite microgels were investigated. Next, the main parameters influencing new tissue formation within the scaffold were evaluated. Cell proliferation, adhesion, motility, and infiltration were analyzed to capture their dependency on the microgel composition and interstitial porous space. The immunomodulatory effect of the drug-loaded HNM was further investigated in fibroblast and macrophage co-culture systems through the paracrine effect. By implementing

quantification methods to evaluate biological performance, it was demonstrated that the HNM modulates the optimal immune function for fibrosis-free tissue repair.

Specific aim 2: The second aim was the development of injectable micropore-forming hydrogels for the modulation of macrophage activation through a cytokine-free approach. Porous double-network (PDN) gels were created that meet the cytocompatibility requirements, in-situ pore-forming, and immune regulation effect. Alterations in the prepolymer compositions affected the porous structure and rheological behavior of the PDN. We then examined the effect of the PDNs with different formulations on cell adhesion and proliferation. Furthermore, we analyzed the influence of hydrogel composition and structural features on modulating macrophage phenotype. Finally, the adhesive properties and hemostasis capacity of the PDN were assessed for wound closure applications. These data are instructive for the rational design of multifunctional hydrogels for wound healing.

Chapter 2 Methodology

This chapter describes the experimental and numerical methods used throughout the dissertation. The procedures related to materials synthesis, imaging methods, mechanical tests, physical characterization, and cell-related experiments are presented. The chapter is divided into four main sections, including materials synthesis, non-biological experiments, biological experiments, and data analysis. Unless otherwise noted, all materials were purchased from Sigma-Aldrich. The sentences in quotations are verbatim of the author's publications (reference [1]).

2.1 Materials synthesis

2.1.1 Synthesis of polymer precursors

"Gelatin methacrylamide (GelMA) was prepared based on the procedure described in Ref.[111]. Briefly, 10 g of gelatin powder (type A from porcine skin, Sigma, USA) was dissolved in 100 mL phosphate-buffered saline (PBS) and stirred for 1 hour at 50 °C. Methacrylic anhydride (15 ml) was added to the gelatin solution at the rate of 0.5ml/min. The mixture was stirred at 50 °C for another 2 hours and diluted 10-fold through the addition of warm PBS (40 °C) to stop the substitution reaction. The resulting solution was dialyzed against deionized (DI) water through a dialysis tubing of 12-14 kDa molecular weight cut-off (Fisher Scientific, USA) for seven days at 37 °C to remove the low-molecular-weight impurities such as unreacted methacrylic anhydride and methacrylic acid byproducts. Finally, the dialyzed solution was freeze-dried and stored at −80 °C until used."

"Hyaluronic acid methacrylamide (HAMA) was synthesized via the modification of Seidlits et al.[112] In short, 1 g of hyaluronic acid powder (molecular weight 2000 kDa) was dissolved in 100 ml of DI water while stirring on ice overnight. After complete dissolution, dimethylformamide (DMF, Sigma, Valkenswaard, the Netherlands) was added dropwise to obtain a water/DMF ratio of 1/1 (v/v). Subsequently, 5 mL of methacrylic anhydride was gradually added to the solution under magnetic stirring. The reaction pH was then adjusted between 8 and 9 using

0.5 M NaOH. The solution was stirred on ice for 12 hrs. After this, the solution was purified by dialysis against DI water (cellulose membrane, MWCO 12–14 kDa) for five days at 4°C, freeze-dried, and stored at −80 °C until further use."

"The degree of methacrylation (DM) of GelMA and HAMA was quantified using a high-resolution proton nuclear magnetic resonance (^{1}H-NMR) spectrometer (Bruker DPX 400) at 1H resonance frequency of 500 MHz. GelMA and gelatin were dissolved in deuterium oxide (D_2O) at a 30 mg/mL final concentration and analyzed at 40 °C. HAMA and hyaluronic acid were dissolved in D_2O at 5 mg/ml, and the ^{1}H NMR spectra were obtained at room temperature. The DM values of GelMA and Gelatin were calculated from the areas of the lysine methylene peaks using the MestreNova NMR analysis program (version 14.2.1, Mestrelabs Research, SL, Spain) using the equation $\text{DM}\ (\%) = \left[1 - \frac{peak\ area\ of\ lysine\ methylene\ groups\ of\ GelMA}{peak\ area\ of\ lysine\ methylene\ groups\ of\ gelatin}\right] \times 100$ [113]."

"The DM is identified as the amount of methacryloyl groups per hyaluronic acid repeating unit. It was calculated from the summed area of the peaks of methacrylate group relative to the integrated area of the hyaluronic acid group peak [114]."

2.1.2 Microgel synthesis

"A solution of GelMA and HAMA was prepared in which the final concentrations of each polymer were 2.5% (w/v) (**Table 2-1**). For comparison, 5% (w/v) pure GelMA solution was also prepared. For complete dissolution, the HAMA solution was stirred at 4 °C for 24 h, and the GelMA solution was heated at 37 °C for 10 minutes. The Laponite (LAPONITE XLG, BYK Additives & Instruments, USA) was dispersed in DI water and stirred vigorously for 30 minutes to obtain stable solutions. For cytokine loading, IL-10 (Peprotech, USA, 2µg per 100µl gel) was premixed with different concentrations of Laponite dispersion (0, 0.5, 1, and 2 wt%). Laponite solutions were then mixed with the GelMA-HAMA solution with a 1:1 ratio. This final gel precursor solution was mixed with polymerization initiator tetramethylethylenediamine (TEMED, 0.5% w/v) and pipetted into a round-bottom flask containing 10 mL 2% span-80 in soybean oil continuously stirring at 500-1500 rpm to generate a stable emulsion. Subsequently, 5ml

ammonium persulfate (APS, 0.25% w/v) was added to the flask's contents and kept under the same stirring condition for 5 minutes. Afterward, the microgels were collected by cell strainers (200-300 um), washed with hexadecane to remove surfactant, and water to remove oil residue."

Table 2-1 Microgel synthesis reagents.

	Hydrogel precursor	Oil phase
PM	2.5% GelMA in PBS	2% span-80 in oil
HM	2.5% GelMA + 2.5% HAMA in PBS	
$HNM_{0.5}$	0.5% Laponite + 2.5% GelMA + 2.5% HAMA in PBS	
HNM_1	1% Laponite + 2.5% GelMA + 2.5% HAMA in PBS	
HNM_2	2% Laponite + 2.5% GelMA + 2.5% HAMA in PBS	

2.1.3 Hydrogel synthesis

If not noted otherwise, the solutions and reagents used in the current work were purchased from Sigma-Aldrich and used as received without further purification. Chitosan (DDA: 95%, medium and high molecular weight) was purchased from Xi'an Lyphar Biotech. Chitosan powder (2.5 wt%) was added to 0.2 M acetic acid and rotated overnight to obtain a homogeneous solution. Various concentrations of gelatin (G2500) were dissolved in the chitosan solution at 37 ˚C to prepare PDN precursors. To prepare the basic gelling agent, a phosphate solution (PS) was prepared by mixing 0.1 M sodium phosphate dibasic (Na2HPO4, S7907) and 0.1 M sodium phosphate monobasic (NaH2PO4, S8282) with a volume ratio of 50:3. Sodium bicarbonate (SC, S233-500, Fisher Scientific) was then added to the phosphate solution, and the pH was adjusted with 1 M HCl to 9.5. The gelling solutions were then completed by adding different concentrations of microbial transglutaminase (mTG, Activa-TI, Ajinomoto North America Inc., Illinois, US) into the buffer solution. Hydrogels of various compositions were formed using a syringe connector and through mixing precursor solutions and their associated gelling agent at a 3:1 volume ratio. For

pure gelatin hydrogels, polyethylene oxide powder (PEO, 189456) was dissolved in the phosphate buffer saline solution (PBS) at a concentration of 2%. The aqueous two-phase precursors were prepared by mixing the PEO solution and the gelatin solution (7.5 wt% in PBS) with the volume ratios of 10:1, 2:1, and 1:1. The hydrogels were prepared by mixing the precursors and mTG solution with a volume ratio of 3:1. The exact ingredients for each formulation are listed in the table **Table 2-2**.

Table 2-2 Hydrogel synthesis reagents

	Hydrogel precursor	**Gelling agent**
NSN	7.50% gelatin in PBS	25% mTG in PBS
PSN	2.5% chitosan in 0.2 M acetic acid	0.445 M SC in PS
$PDN_{1.25, L}$	1.25% gelatin + 2.5% chitosan in 0.2 M acetic acid	0.445 M SC + 5% mTG in PS
$PDN_{1.25, H}$	1.25% gelatin + 2.5% chitosan in 0.2 M acetic acid	0.445 M SC + 10% mTG in PS
$PDN_{2.5, L}$	2.50% gelatin + 2.5% chitosan in 0.2 M acetic acid	0.445 M SC + 10% mTG in PS
$PDN_{2.5, H}$	2.50% gelatin + 2.5% chitosan in 0.2 M acetic acid	0.445 M SC + 15% mTG in PS
$PDN_{3.75, L}$	3.75% gelatin + 2.5% chitosan in 0.2 M acetic acid	0.445 M SC + 15% mTG in PS
$PDN_{3.75, H}$	5.00% gelatin + 2.5% chitosan in 0.2 M acetic acid	0.445 M SC + 20% mTG in PS
$PDN_{5, H}$	3.75% gelatin + 2.5% chitosan in 0.2 M acetic acid	0.445 M SC + 20% mTG in PS
$PDN_{5, H}$	5.00% gelatin + 2.5% chitosan in 0.2 M acetic acid	0.445 M SC + 25% mTG in PS
Gel- PSN_1	6.82% gelatin + 0.18% PEO in PBS	22.72% mTG in PBS
Gel- PSN_2	5% gelatin + 0.67% PEO in PBS	16.67% mTG in PBS
Gel- PSN_3	3.75% gelatin + 1.00% PEO in PBS	12.50% mTG in PBS

2.2 Non-biological experiments

2.2.1 Rheological properties

"The rheological properties of hydrogel samples were measured using a single head rotational rheometer (Discovery Hybrid HR-2, TA Instrument, DE) equipped with a 20 mm parallel plate. A volume of 560 µl of each sample was prepared and injected immediately to completely fill the gap and form a 1 mm-thick layer between the two plates. Strain-sweep tests were performed after a soaking period of 5 minutes at 37 °C to ensure complete curing. The dynamic shear modulus was determined in oscillatory mode at a deformation frequency of 1 rad/s with varying strain amplitudes from 1% to 100%. The shear storage modulus (G′), indicative of elasticity, and the shear loss modulus (G″), indicative of damping, were measured within the linear viscosity range."

"To examine the shear-thinning properties of packed microgels, viscosity was measured over a shear rate ranging from 0 to 50 s^{-1}. Shear recovery experiments were performed at periodically low (1%), and high (500%) strains at a constant frequency of 1 Hz."

"An atomic force microscope (JPK NanoWizard 3, Berlin, Germany) was used to perform nano-indentation tests to estimate the microscale Young's modulus of the sample. The measurements were conducted under PBS to maintain the hydration state. Rectangular silicon cantilevers with 25-µm in-diameter spherical beads attached as probes were used (Novascan, IA, USA). Cantilevers with a nominal spring constant of 0.6 N/m were used. The spring constants of the cantilevers were determined using a thermal noise method before the experiments. Indentation experiments were performed at 150 nm depth and at a number of locations for each sample. The Hertzian contact model was used to extract Young's moduli."

"Gelation kinetics and amplitude sweeps were measured using a single head rotational rheometer (Discovery Hybrid HR-2, TA Instrument, DE) with a 10 mm parallel plate. A volume of 560 µl of each sample was prepared and injected immediately to form a 1 mm-thick layer between the two plates." A solvent trap was used to avoid water evaporation from the sample

throughout the duration of the test. A time-sweep analysis was performed immediately after injection at a frequency of 0.1 Hz and 0.1% strain at 37 °C over a 2 h period to ensure complete curing. Strain-sweep tests (0.01 to 100%) with a loading frequency of 0.1 Hz were then performed with a 0.1% of shear strain at 37°C. "The dynamic shear modulus was determined in oscillatory mode at a deformation frequency of 1 rad/s with varying strain amplitudes from 1% to 100%. The shear storage modulus (G′), indicative of elasticity, and the shear loss modulus (G″), indicative of damping, were measured within the linear viscosity range."

2.2.2 Tissue injection simulation

"Agarose gel was used to simulate soft tissue samples. Agarose powder (0.5% (w/w)) was added to a beaker of PBS and stirred at 95 °C for 10 minutes. The solution was cast into glass vials with an internal diameter of 2 cm and cooled to room temperature. The gels were left for 1 hour at 37 °C before use. $HNM_{0.5}$ at 15% (w/w) in DI water was injected using a 21G hypodermic needle into agarose gel at 37 °C."

2.2.3 Adhesion energy

To measure the adhesion energy, hydrogels and substrates were cut into strips of 15 mm in width and 1.5 mm in thickness with 80 mm in length. Hydrogels were brought into contact with various tissues for 30 minutes and then tested with an Instron machine (10 N or 1 kN load cell) with peeling tests for T-peeling tests. The displacement rate was 100 mm $minute^{-1}$. The adhesion energy of the tissue strips was determined by dividing two times the average force at the plateau (F_{avg}) by the thickness of the specimen: $\Gamma = 2F_{avg}/\mathrm{W}$.

2.2.4 Pores and structures

"For morphology analysis, microgels were imaged by optical microscopy. Then images, each containing ~10 microgels, were analyzed using image analysis software (Image-j). The

circularity of the microparticles (C) was calculated in terms of the area and perimeter of their contour using the following the equation $C = 4\pi \times \frac{area}{perimeter^2}$ [115]."

"Roundness is the same as circularity, except that it is not sensitive to irregular boundaries. Microgels were analyzed using the "fit ellipse" feature of ImageJ software. Roundness (R) was then determined using the area of the microgels contours and the major diameter of the best fitting ellipses using the equation $R = 4\pi \times \frac{area}{\pi \times [major\ diameter]^2}$ [115]."

"The microstructure and composition of the microgels were examined with a high-resolution field-emission scanning electron microscope (F50, FEI) with energy dispersive x-ray analysis (EDX). Microgels were first attached to glass coverslips using Poly-L-Lysine Hydrobromide with a molecular weight in the range of 70-150 kD (Electron Microscopy Sciences, USA).[116] Dehydration was carried out by sequential immersion of the samples inside 30, 50, 70, 80, 90, and 100% ethanol. To preserve the original structure, ethanol was removed using a CO2 supercritical point dryer (CPD030, Leica). Samples mounted on metal were sputter-coated with a 4 nm- layer of platinum using a sputter coater (ACE600, Leica) to increase surface conductivity."

"The microgels' porosity was determined using the liquid displacement method with pure ethanol, as it penetrates into the microgels without inducing any swelling or shrinkage. Dehydrated samples with known weight (W1) were immersed in pure ethanol for 24 h and their wet weight (W2) was measured after removing the extra ethanol. The porosity was calculated using the equation $Porosity\% = \frac{W_1 - W_2}{\rho V} \times 100\%$, where ρ is ethanol's density and V is the microgels volume."

"A quantitative micro-computed tomography specimen imaging scanner (SkyScan 1172 Bruker micro-CT, Belgium) was used to image the distribution of the nanoclays in the Microgel-based scaffolds. The swollen microgels were loaded into a 1.5 ml microtube and were imaged through a 360° flat-field corrected scan with a rotational step size of 0.45°. A medium resolution

scan of 11 μm (pixel size) was selected at 40 kV and 250 μA without a filter. The volumetric reconstruction (NRecon, Micro Photonics) was conducted with a beam hardening correction of 12, a ring artifact correction of 4, and an auto-misalignment correction. The images acquired from the microCT scan were then processed using the Dragonfly software (Object Research Systems, Montreal, Quebec, Canada) and a grayscale intensity range of 50 to 85 (8-bit images) to remove background noise. Representative images of cross-sections of all samples were chosen to confirm the intercalation of nanoparticles in each scaffold type."

The gel structure was imaged using a confocal microscope (LSM 710, Zeiss). Rhodamine-B isothiocyanate (Cayman Chemical, 20653) was conjugated to chitosan polymeric chains following published protocols.[117] Gelatin was conjugated with Fluorescein-5 isothiocyanate (FITC, Thermo Fisher, F1907) fluorescent labels according to established protocols.[118, 119] Briefly, 1 wt% gelatin was initially dissolved in DI water at 40.C. the pH of the solution was adjusted to about 9.5 using 0.1 M sodium carbonate, allowing the reaction of gelatin chains with FITC. The FITC was dissolved in dimethyl sulfoxide (DMSO) at 50 mg ml^{-1}. Under stirring, 200 ul of the staining solution was added to the gelatin solution drop-by-drop, and then the stirring lasted 24 hours. Unconjugated FITC was removed by dialysis in a 12-14 kDa dialysis bag against DI water for 3 days. The stained solution was then freeze-dried at − 84 °C and kept at − 20 °C until further use. The Hydrogel samples were fabricated by mixing fluorescent-labeled polymer solutions and crosslinkers in a vial under vortexing and immediately transferring ~150 μL into a glass bottomed, 35-mm Petri dish (81158, Ibidi). Hydrogels were immersed under PBS and imaged with a 20x objective lens.

The hydrogel structure was also imaged using a field emission scanning electron microscope (F50, FEI). The samples were dehydrated by immersion inside a 0, 50, 70, 80, 90, and 100% ethanol series. Hydrogels were dried inside a CO2 supercritical point dryer (CPD030, Leica) to eliminate the ethanol within the hydrogels. The dried specimens were placed inside a high-resolution sputter coater (ACE600, Leica) and coated with a 4 nm, electrically conductive layer of Pt.

2.2.5 Swelling

"To determine the swelling ratio of different samples, triplicate groups of fully swollen microgels or hydrogels were weighed and immersed in PBS solution (pH = 7.4) at 37 °C with gentle orbital shaking at 75 RPM. At pre-determined time intervals, the excess water on the surface was removed using a filter paper, and the samples were immediately weighed. The swelling ratio (SR) was calculated as grams of water per gram of dry hydrogel (g/g) using the equation $SR = \frac{W_S - W_d}{W_d}$ where W_s and W_d are the weights of the samples at the swollen and dried state, respectively."

2.2.6 Degradation

"For biodegradation assays, about 1 mL microgels were initially weighed (W_i) and then incubated in 5 mL MMP-2 enzyme at 37 °C in a horizontal orbital shaker under constant agitation at 200 rpm. The MMP-2 enzyme buffer was composed of 0.5 nM MMP-2 (PeproTech, USA), 50 mM HEPES, 10 mM $CaCl_2$, 20% glycerol, and 0.005% tween 20. The enzyme solutions were refreshed every other day, and the remained microgels were collected at each time point. The samples were washed three times for 5 minutes with PBS, freeze-dried, and weighed (W_f). The percentage of the remaining weight was calculated as $\frac{W_f}{W_i} \times 100\%$."

For biodegradation tests, around 200 mL of hydrogel was incubated in a 1.5 mL enzyme solution at 37 °C in a horizontal orbital shaker under constant agitation at 200 rpm. The average dry weight of the fresh gels was considered as the initial weight. The enzyme solution was composed of 50 µg/ml lysozyme (Sigma, L4919) and 50 µg/ml collagenase (Sigma, 1148089) in PBS. The enzyme solutions were refreshed every other day, and the remained gels were collected at each time point, freeze-dried, and weighed (W_f). The remaining weight percentage was calculated by dividing the dry weight of the degraded gels by the dry weight of the original gels.

2.2.7 Drug release

"The Zeta potential of the Laponite and IL-10 – loaded nanoplatelets (3 µg of IL-10 per mg of Laponite) was measured in DI water using a Zetasizer Nano ZS (Malvern) equipped with a folded capillary zeta cell (DTS10170). Before the experiment, the dispersions were prepared using 5 minutes vortexing, 10 minutes ultrasonication, and 10 minutes vigorous stirring. The obtained data were analyzed using the Data Transfer Assistance (DTA) software (Malvern Zetasizer Limited, Malvern, UK) following a dynamic light scattering method at 25 °C."

"The controlled release property of the loaded IL-10 was assessed using ELISA. The IL-10-loaded microgels were immersed in a 1% bovine serum albumin solution in PBS (release buffer) in 37 °C incubators. The supernatants from the incubation solutions were collected and frozen at −20 °C. A fresh release buffer was added to the samples at the indicated timepoints. According to the manufacturer's specifications, the withdrawn release buffers were then assayed for protein using Human IL-10 ELISA Development Kits (Abcam, USA). The quantitative IL-10 measurement was performed through monitoring the optical density with a Synergy HTX multi-mode reader (Biotek, USA) at 450 nm."

2.3 Biological experiments

2.3.1 Cell culture

"Immortalized human vocal fold fibroblasts (HVFFs) were cultured in Dulbecco's Modified Eagle Medium (DMEM, Corning, NY) supplemented with 10% fetal bovine serum (FBS) and 1% penicillin/streptomycin. Human monocytic THP-1 cells were cultured in Roswell Park Memorial Institute medium (RPMI 1640) supplemented with 10% FBS, 1% penicillin-streptomycin, 10 mM HEPES, and 1 mM sodium pyruvate. Cells were maintained in 75- or 25-cm^2 culture flasks at 37°C in a humidified incubator containing 5% CO2. The medium was replaced every 3 days." The HVFFs detaching was performed during routine passage or cellular studies using 0.25% trypsin-EDTA when the cultures reached a confluency of about 70%.

2.3.2 HVFFs proliferation

"For cell culture studies, all materials either arrived sterile, were sterilized by autoclaving, or were filter sterilized. Cells were grown on the microgels over periods of either 1, 7, or 14 days. The medium was changed every two days, and 3-(4,5-dimethylthiazol-2-yl)-2,5-diphenyl-2H-tetrazolium bromide (MTT) assays were used to measure cell proliferation. At each time point, the medium in each well was replaced by 100 μL of fresh culture medium containing 10 μL of 0.5 mg mL^{-1} MTT solution. After incubation for 4 h at 37°C, the received formazan crystals were dissolved by the addition of 100 μL of DMSO to each well. The solution from each well was placed in a 96-well culture plate, and the optical density was measured at 580 nm on a Synergy HTX multi-mode reader."

The HVFFs were added to the hydrogel mixtures during vortexing quickly after the precursors with gelling agents were mixed. The mixtures with the cellular concentration of 1 million/ml were rapidly transferred to Petri dishes to form a thin layer. The mixtures were then cured at 37 C for 0.5 h, followed by the addition of a complete cell culture medium. HVFF s were stained by a LIVE/DEAD viability kit (L3224, Invitrogen) inside 3D matrices on Day 14. Imaging of fixed HVFFs was performed using a confocal laser scanning microscope (LSM710TM, Zeiss, Germany).

2.3.3 HVFFs morphology

"To investigate the morphological characteristics of cells, HVFFs were seeded on the surface of microgels with a coating density of 10000 cells/cm^2. The HVFFs were added to the hydrogel mixtures at a concentration of 1 million/ml. After incubation for 3 days, the scaffolds were washed twice with pre-warmed PBS and fixed with 4% paraformaldehyde for 20 minutes. The fixed samples were rewashed with PBS twice, then permeabilized with 0.5% Triton X-100 for 15 minutes. The samples were then blocked in 1% bovine serum albumin (BSA, A1595) for 1 hour. The F-actin stress fibers and nuclei were stained with Alexa Fluor 488 phalloidin using a

1:200 dilution for 45 minutes and Hoechst 33342 (H3570, Invitrogen) using a 1:2000 dilution for 10 minutes. After staining, the cell–microgel constructs were rinsed twice with PBS."

2.3.4 HVFFs motility and macrophage recruitment

"For the cell motility study, live cells were stained using a Vybrant® DiO cell-labelling solution (Invitrogen, Carlsbad, CA). A volume of 200 µl cell solution, with a cell concentration of 50,000 fibroblasts per ml, was added to each well of an 8-well µ-slide (Ibidi, Martinsried, Germany) to cover the microgels.[120] A confocal laser scanning microscope (Zeiss LSM710, Oberkochen, Germany) was used to track cells' movement for 8 hours. The acquisition and analysis of the time-lapse images were performed using Zen 2.6 (Zeiss, Oberkochen, Germany) and Imaris 8.3.1 (Bitplane, Zurich, Switzerland), respectively."

"For macrophage recruitment studies, THP-1 cells were first stained with Vybrant® Dil cell-labelling solution (Invitrogen, Carlsbad, CA). For differentiation to inactivated macrophage (M0) phenotype, 200 nM Phorbol 12-myristate 13-acetate (PMA) was added to the cell solution and immediately added to the 8-well culture plate containing microgels."

2.3.5 Macrophage morphology and M2 marker expression

Monocytes were added to the hydrogel mixtures at the concentration of 3 million/mL. For differentiation to M0 phenotype, 200 nM PMA was added to the Petri dishes containing THP-1-encapsulated gels. After 3 days, the medium was changed, and the cells were incubated for another 3 days. At that time, the F-actin stress fibers were stained with Alexa Fluor 488 phalloidin using a 1:200 dilution. Cells were then incubated with Alexa Fluor® 488 Anti- CD206 antibody (1: 200, ab-195191, Abcam, USA) for 1 hour. Samples were then stained with Hoechst 33342 and imaged using a confocal microscope.

2.3.6 Co-cultures of HVFFs with macrophages

"Monocytes were plated at 4 million cells per 60 mm petri dish and allowed to differentiate and adhere over 3 days. At that time, fibroblast-seeded microgels were placed into Petri dishes containing macrophages using transwell inserts. The system was then co-cultured in complete RPMI, with the medium changed every three days. After 8 days, the attached macrophages were stained with mouse anti-CD163 monoclonal antibody (1: 200, ab-182422, Abcam, USA). After 1 hour of incubation, the unbound antibody was rinsed off with PBS, and the cells were incubated with secondary antibody (1:200, Alexa Fluor 488 goat anti-rabbit IgG, Invitrogen, A11034). Samples were then stained with Hoechst 33342 and imaged using a confocal microscope. Fibroblast-containing gels were removed from the transwell inserts, fixed, permeabilized, and blocked. The samples were further incubated in a solution of collagen-I primary antibody (1:50, Abcam, ab34710) for 1h at room temperature. Then, the samples were washed with PBS thrice and incubated with secondary antibodies (1:200, Alexa Fluor 488 goat anti-rabbit IgG, Invitrogen, A11034). After removing the staining solution, the samples were washed thrice again with PBS and stained with Hoechst 33342. Quantification of CD163 and collagen-I fluorescence (the sum of the signal intensities) was performed using Imaris. Macrophage supernatants were collected two days after removing the transwell inserts and assessed for IL-10 release using ELISA."

2.3.7 In vivo studies

This experiment was approved by the McGill University Animal Care Committee (Protocol # 2019-8098) and performed according to the Canadian Council on Animal Care guidelines. Female Sprague Dawley rats (250-300 g) were used for all the *in vivo* rat studies.

2.3.8 Rat tail bleeding model

For hemostatic sealing of the deep incisional hepatic injury, the rats were anesthetized using isoflurane (4% isoflurane in oxygen) in an induction chamber. Anesthesia was maintained at 2% isoflurane using a nose cone during the surgery, and the rats were placed over a heating pad for the duration of the surgery. Then, 30% length of the tails were transected with a sharp surgical

blade. Immediately after wiping off the blood using gauze, the hemostatic testing agent was applied to the lesion site. The amount of blood loss and the time period required to reach hemostasis were recorded for each group. After surgery, the rats were euthanized using 5% isoflurane induction followed by CO2 inhalation.

2.4 Data analysis

2.4.1 Imaging processing

The 3D reconstruction of the encapsulated cells and the gel structure was carried out using Imaris. Pore size was examined by measuring 50 pores for each condition using the length measurement tool in ImageJ. Porosity measurement was done by first converting the fluorescent images to binary images and then dividing the number of white pixels by the total number of white and black pixels. Cell circularity was calculated automatically using Image-j and by setting the proper threshold on the single-channel (F-actin) confocal images to define the edges of the cells. Individual cells were identified using the "Surfaces" function of Imaris. Cell diameter was set to 10 um for macrophages and 20 um for fibroblasts, and then each object was identified, counted, or tracked. Cell viability and density were calculated from the automatic cell counting, while cellular speed and displacement were measured from the tracks. Fluorescent intensity was measured using an object-based 3D-surface segmentation method using Imaris

2.4.2 Statistical analysis

"A sample size of $N \geq 3$ was used for all tests. Error bars indicate the standard deviation (SD) of the mean. Statistical analysis was performed using an unpaired Student's t-test or one-way or two-way ANOVA followed by Tukey's post-test using GraphPad Prism 9 (GraphPad Software, Inc., CA). P values < 0.05 were considered statistically significant."

Chapter 3 Hybrid nanocomposite microgels for sustained cytokine delivery

This chapter discusses the influence of cytokine-loaded microgels on cell function. Different groups of injectable hybrid nanocomposite microgels (HNMs) were subjected to a series of physical, rheological, drug release, biodegradation, and biological tests. Cell adhesion, proliferation, motility, and recruitment in the granular hydrogels' three-dimensional (3D) network were assessed. The immunoregulatory effect of the microgels with different Laponite concentrations was determined in a fibroblast/macrophage co-culture model. The results support the plausibility of using cytokine-loaded composite microgels as an injectable immunomodulatory scaffold for regenerative therapy. The sentences in quotations are verbatim of the author's publications (reference [1]).

3.1 Functionalization of the prepolymers

"As a precursor to the fabrication of microgels, the chemical properties of gelatin, hyaluronic acid, GelMA, and HAMA were characterized. **Figure 3-1**a shows the ^{1}H NMR spectrum of gelatin and GelMA. The effect of methacrylation on the chemical structure of the gelatin molecules is identified by three salient changes in the peaks of the gelatin spectra. The peaks a (5.8 ppm and 6.2 ppm) correspond to the acrylic protons (2H) from $=$CH2 functional groups of the methacryloyl grafts of lysine and hydroxyl lysine. The peak b is related to the methyl protons (3H) of methacrylate around 1.8−2.1 ppm. The peak c around 2.8 ppm and 3.2 ppm corresponds to the lysine methylene protons (2H) [113, 121-123]. It was observed that the peaks a + a' were formed, and the intensity of peak b increased following methacrylation with the methacrylic anhydride. The dispersion of peak c in the GelMA spectrum, on the other hand, confirmed the elimination of lysine methylene (NH_2) and the complete linkage of lysine groups with methacrylic anhydride. Overall, the ^{1}H-NMR spectra confirmed the complete methacryloyl

functionalization of gelatin. The degree of methacrylation of GelMA was around 78 %, similar to the previous report [124].”

“The molecules of hyaluronic acid were modified through the esterification of the primary alcohol group of the N-acetyl-D-glucosamine monomer with methacrylic anhydride basic pH conditions [125]. The HAMA spectrum displayed peaks corresponding to acrylic protons of methacryloyl grafts between 5.8–6.3 ppm, absent in the spectrum of hyaluronic acid (**Figure 3-1**b). Peak b, corresponding to methyl protons of methacrylate (1.8 ppm), was present in the spectrum of HAMA but not hyaluronic acid. Peak c, at 2.1 ppm, was substantially smaller in the spectrum of HAMA, indicating that many methyl groups of the acetamido moiety of the N-acetyl-D-glucosamine unit were functionalized. Furthermore, the signals from the combination of ten protons in the hyaluronic acid backbone (3–4.2 ppm) were reduced [126-128]. The degree of modification of HAMA was calculated as ≈ 23 %.”

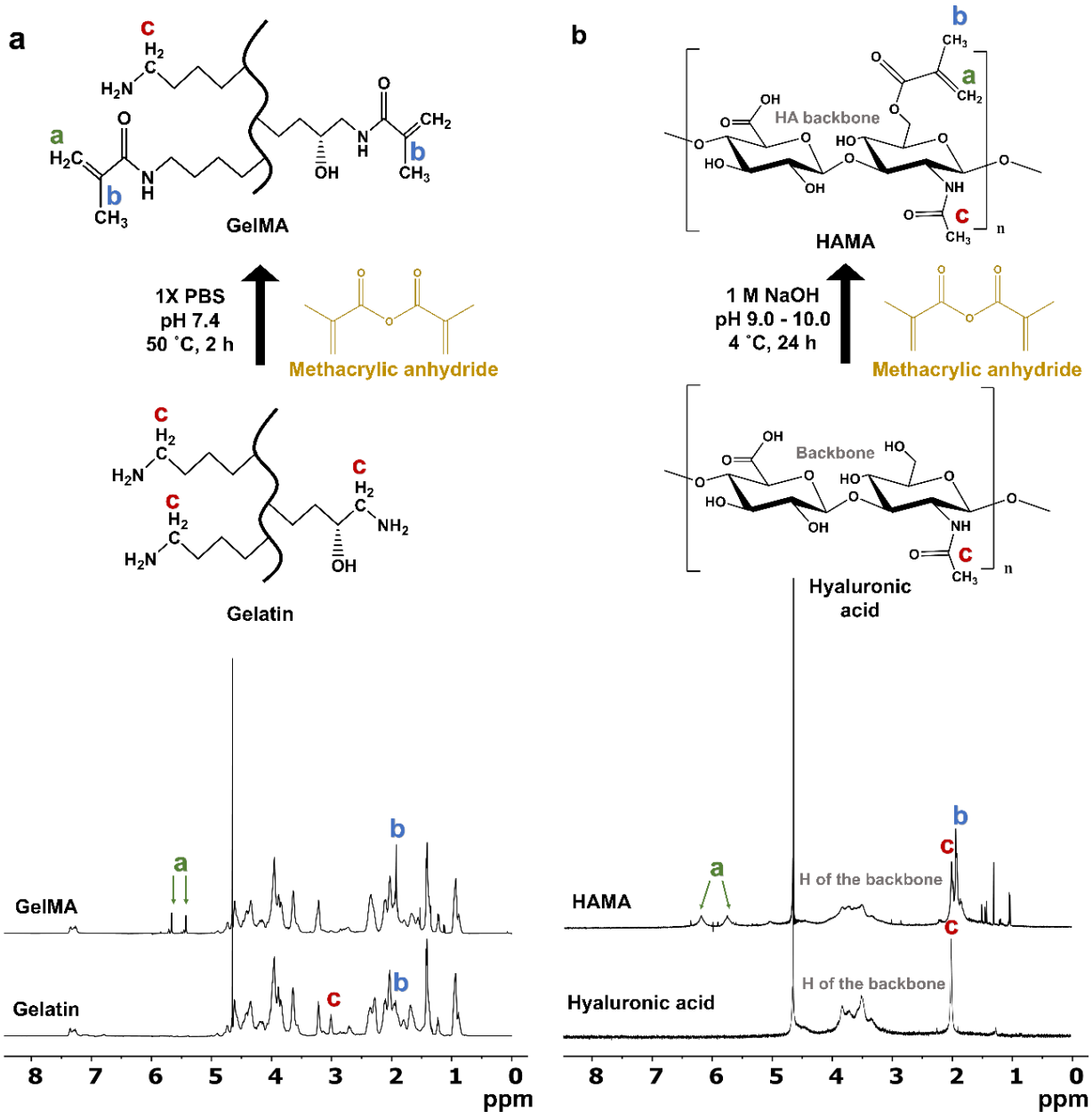

Figure 3-1 "[1]H NMR spectra of gelatin, hyaluronic acid, and their methacrylamide forms prepared in D2O. (a) [1]H NMR spectra of gelatin (bottom) and GelMA (top). (b) [1]H NMR spectra of hyaluronic acid (bottom) and HAMA (top)."

3.2 Synthesis of microgels

"To synthesize HNMs, precursor solutions were prepared by mixing different amounts of IL-10 -loaded Laponite with GelMA/HAMA polymer solution. To ensure polymer network formation at room temperature, tetramethylethylenediamine (TEMED) was added to the microgel precursor, thereby forming a redox initiator system. Aqueous droplets were produced using the batch emulsification method and by the addition of the precursor solution to the oil phase while stirring the solution. Crosslinked beads instantly formed upon the addition of the ammonium persulfate (APS) solution to the emulsion through the use of APS as the initiator and TEMED as the accelerator of APS radical formation. We denoted the resulting microgels as HNMx, where x stands for the w/v percentage of Laponite content. The concentration of polymer for all the conditions was fixed at 5%. Hybrid microsphere (HM) without Laponite, and pure microsphere (PM) containing 5% GelMA, were also synthesized as controls."

3.3 Structural properties

"Structural characteristics such as porosity and nanoparticles distribution have a major impact on the physical, mechanical, and biological properties of the resulting nanocomposite gels [129-132]. In all cases, the obtained microgels had an average diameter ranging from 200 to 300 μm (**Figure 3-2**). They were well-dispersed and acquired a well-defined spherical shape. When the microgels are in a jammed state, the interstitial space among the packed beads results in inter-connected pores with sizes between 70 μm to 120 μm which is in the range of pore size suitable for wound healing [133]. One of the main requirements for endogenous tissue regeneration is the infiltration of the neighboring cells into the repair site containing a scaffold that presents cell-modulating signals. The structural advantage of using granular hydrogels over microporous bulk hydrogels is the flexibility to control pore architecture independently of local stiffness and degradability [134, 135]."

“The effects of hyaluronic acid microgel size were previously studied on dermal fibroblasts [136]. Seeding fibroblasts in gels with mid-sized (60–100 μm) and large (100–200 μm) beads enhanced spreading, proliferation, and transgene expression relative to gels with smaller particle sizes (20–60 μm). In another recent study, poly(ethylene glycol) microgels containing a fibronectin-derived adhesive peptide were generated with average diameters of 100 and 10 μm.[137] Nearly 50% of pores in the 100 μm and 10 μm networks were observed to have major axes in the range of 22 - 120 μm and 6 - 14.0 μm, respectively. Furthermore, the 100 μm networks resulted in higher interstitial porosity (~ 29%) compared to the 10 μm gel (~ 12%).“

“The non-composite microspheres were nearly transparent. At the same time, Laponite-containing groups displayed a more opaque and ground-glass shape, leading to the appearance of bulk clay morphologies for the highest concentration. Furthermore, small voids are disorderly distributed within the microspheres in the absence of hyaluronic acid, likely because of primary droplets' low viscosity [138]. The viscosity ratio of the internal phase (water) to the external phase (oil) plays a key role in determining the size of the formed particles. Here, the internal phase became more and more vicious by increasing the Laponite concentration in the polymer solution. This led to increased interfacial tension, which is a measure of the needed work to create new surfaces [139]. In the present case, the higher threshold to the creation of new surfaces was compensated by increasing the rotation speed of the stirring bar from 500 to 1500 rpm. But slight imperfections such as pointy edges, protrusions, or ellipsoidal particles, were observed in the samples with high Laponite concentrations [139, 140].”

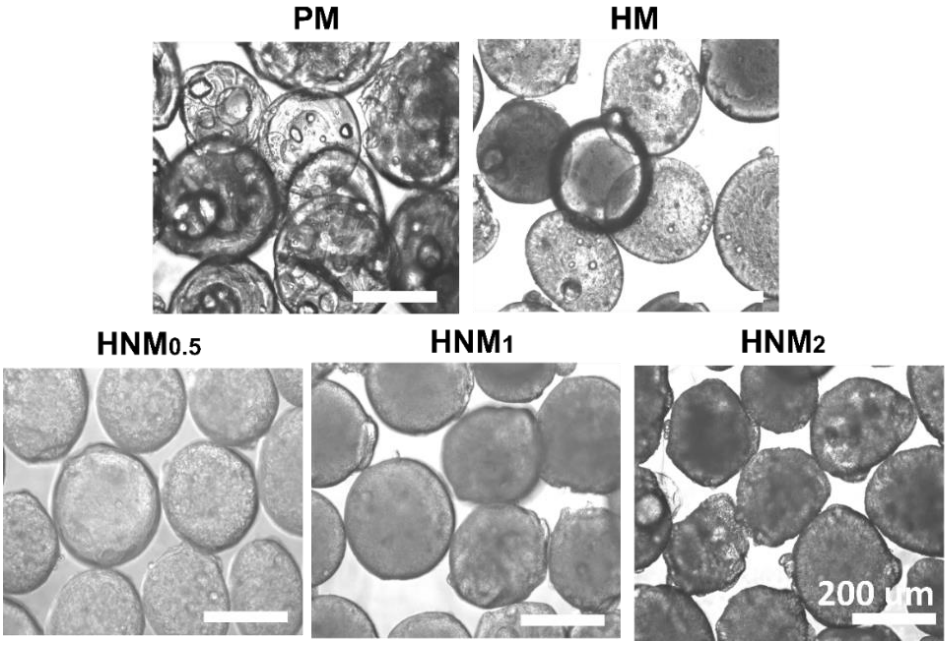

Figure 3-2 "Light Microscopy of different microgels."

"Laponite XLG ($Na^{+}0.7[(Si8Mg5.5Li0.3)O20\ (OH)4]$-0.7) is a synthetic smectite clay consisting of variously oriented and flake-like particles (**Figure 3-3**). Referring to previous studies, the plate-like morphology was most likely the result of the stacking of octahedral and tetrahedral nanocrystal layers [141]. The measurement of platelet size shows that the average thickness of small particles seen by SEM is 10–15 nm, with plate width in the range of 50–200 nm. The elemental percentage shown in **Table 3-1** demonstrates a strong signal for the oxygen (O), Magnesium (Mg), silicon (Si), and sodium (Na) atoms."

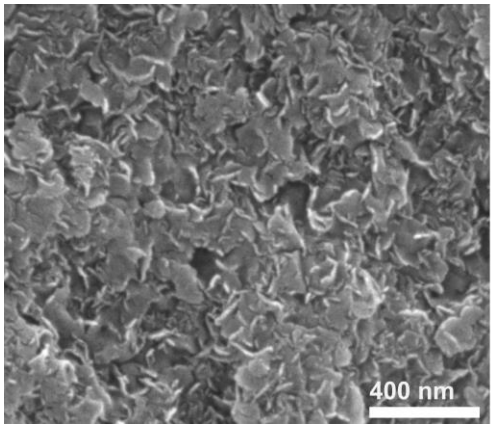

Figure 3-3 “SEM micrograph of Laponite.”

“The morphology and the microstructure of the microgels are depicted in **Figure 3-4**a. Based on the results, 2 wt% concentration of Laponite resulted in highly clamped microparticles with many irregular bulges on the surface. The concentration of 1 wt% also developed a cookie-like morphology. The microparticles with the highest circularity/roundness were formed using concentrations of 0 and 1 wt% (**Figure 3-4**b). Production of microparticles with controllable shape and size also becomes important when designing high-viscosity macromolecular solutions for a microfluidic device. In this case, the work required for generating uniform droplets may be provided by altering the flow rate ratio of the liquid phase to the oil phase [142].”

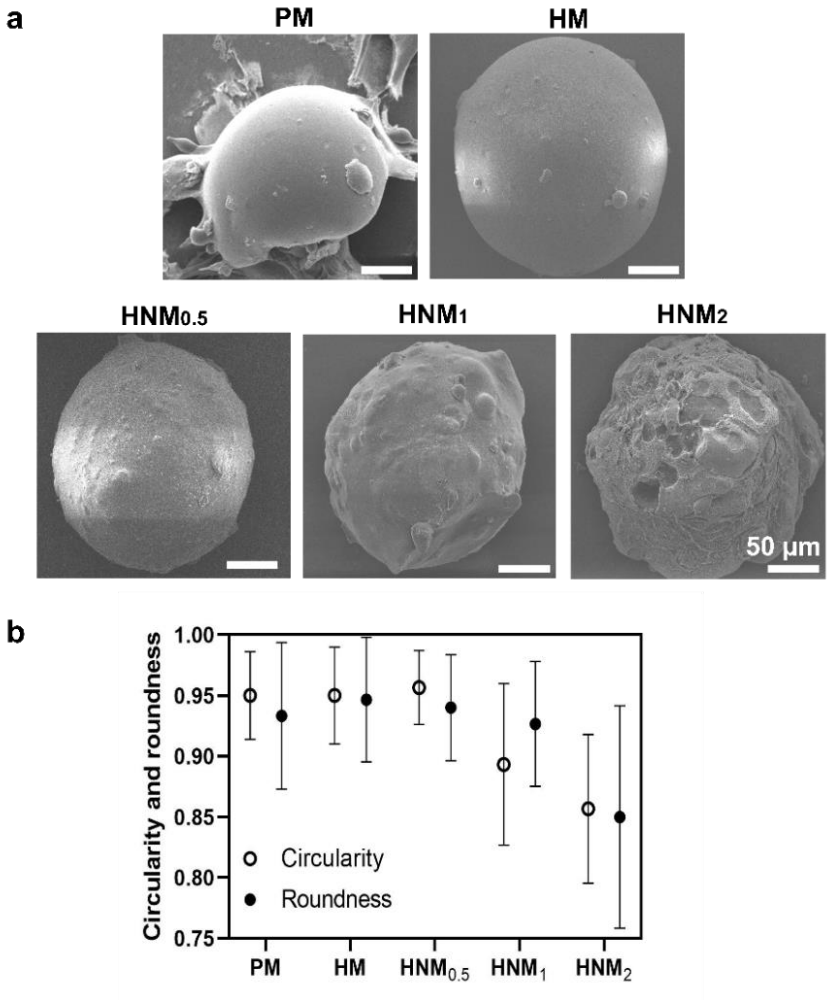

Figure 3-4 "(a) Low magnification SEM images showing the morphology and porous structures of PM, HM, and HNMs. (b) Analyses of the microgels' shape, Sample size, N = 4."

"As shown by images with higher magnification (**Figure 3-5**a**)**, the PM was nonporous and homogenous, with only a few holes on the surface. The addition of HAMA produced several small, non-uniformly distributed pores. The $HNM_{0.5}$ microspheres, on the other hand, had a uniform distribution of interconnected pores with an average diameter of ~ 380 nm (**Figure 3-5**b). This suggests that the $HNM_{0.5}$ sample might have a higher swelling ratio than the single-phase microgels, as eventually confirmed as described in the next section. The micrographs of the HNM_1

nanocomposites revealed a rather net-like structure with visibly smaller pores (~ 267 nm), which can be the result of Laponite nanoparticles' crosslinking at this concentration. The insertion of 2 % of Laponite XLG into the polymer matrix caused the pores to become larger (~ 502 nm) than HNM_1. But the pores were structurally irregular. The red arrows show the small circular inclusions observed in nanocomposite samples that could indicate Laponite positions. These high contrast entities were examined with an SEM–EDX technique, where the spectrum illustrates a great percentage of Laponite-related elements. These results support that the visible features under SEM are clay and not contamination. As expected, the PM and HM had only carbon (C) and oxygen (O) elements (**Table 3-1**). Although the EDX technique is semi-quantitative, it clearly indicates higher Mg, Si, and Na levels in the hydrogels containing higher nano clay levels."

"Figure 3-5 c displays the porosity measurement of the microgels. A porosity of ~ 12% was estimated for PM, while it was ~ 24% for HM. The presence of hyaluronic acid increases the polymer blend's swelling capacity, resulting in an improved porous structure. By adjusting the concentration of Laponite, the porosity can be tuned over a range of ~ 33-56%. This could be explained by the higher number of interconnected pores creating a greater pore volume in HNMs."

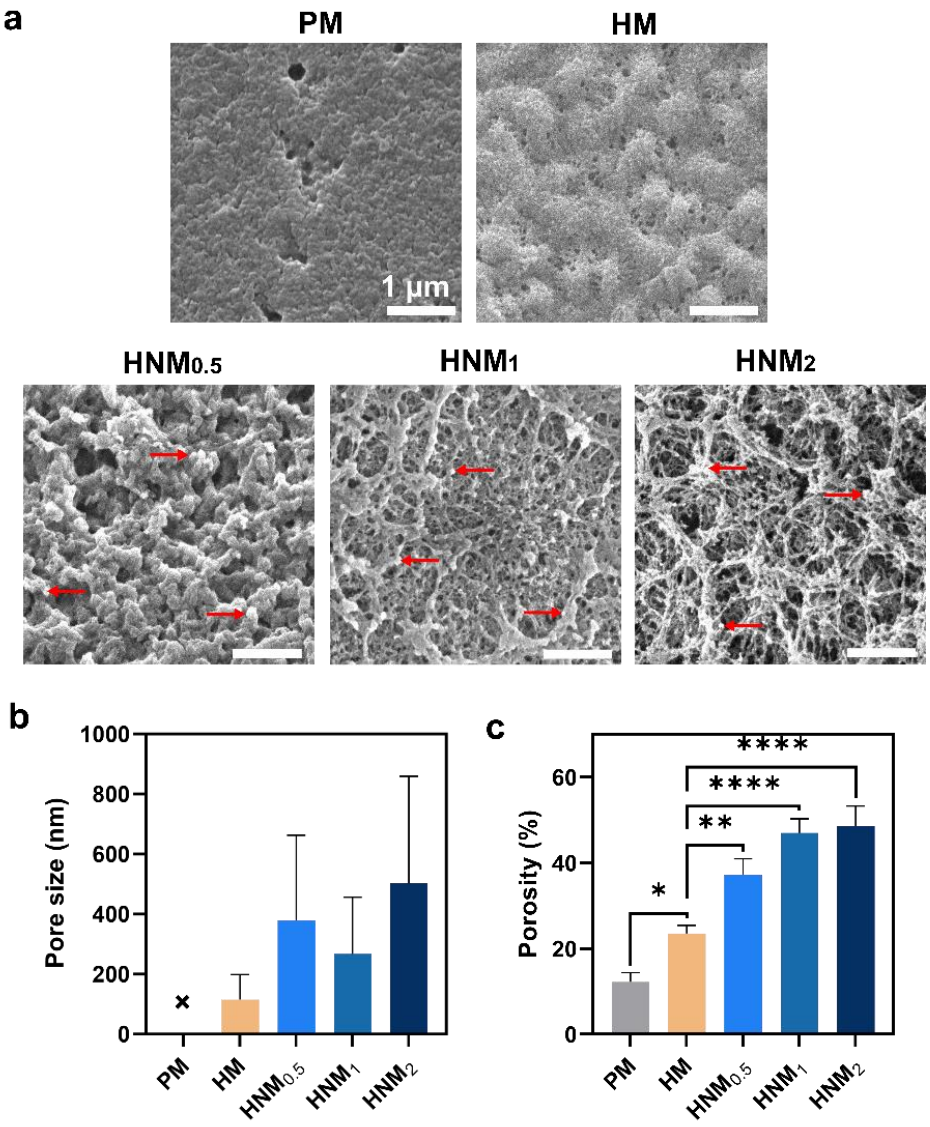

Figure 3-5 "(a) High magnification SEM images showing the morphology and porous structures of PM, HM, and HNMs. (b) Pore size and (c) porosity of PM, HM, and HNMs." * represents $P < 0.05$, ** $P < 0.01$, *** $P < 0.001$, **** $P < 0.0001$, n.s. means $P \geq 0.05$, Sample size, $N = 4$.

Table 3-1 "Analysis of EDX of the Laponite, HM, and different HNMs."

	Elements (% atomic mass)				
Samples	**Carbon ©**	**Oxygen (O)**	**Magnesium (Mg)**	**Silicon (Si)**	**Sodium (Na)**
Laponite	-	60.62 ± 6.18	21.08 ± 4.86	15.79 ± 5.32	2.21 ± 15.64
HM	68.00 ± 7.64	16.49± 13.94	-	-	0.72 ± 18.47
$HNM_{0.5}$	36.20 ± 7.48	34.79 ± 10.54	0.50 ± 30.58	1.04 ± 16.03	1.89 ± 14.64
HNM_1	43.53 ± 6.80	34.65 ± 9.93	0.40 ± 28.49	1.14 ± 11.76	2.22 ± 13.51
HNM_2	42.31± 7.77	30.78 ± 10.01	1.74 ± 10.56	2.23 ± 7.94	3.47 ± 13.06

"The nano clay distribution within the nanocomposite microgels was further characterized using a MicroCT system [143]. Micro-computed tomography (μCT) is widely used to study hard tissues or high-density materials that provide sufficient contrast. Nevertheless, a similar use for soft tissues or water-absorbing polymers hydrogels is hindered as a result of their water-like and low X-ray attenuation. Due to their high atomic number of elements, nanoparticles are widely used as contrast developing agents *in vivo* μCT imaging [144, 145]. Here, the microgels' contrast was naturally enhanced by incorporating Laponite nano clays into the swollen polymer network. Although the μCT does not enable the identification of separate nanoparticles, stacking the nanoparticles in the gel gives rise to a zone with a much greater density than the surrounding area, thereby allowing density variation detection by the μCT system [146]. **Figure 3-6**a reveals that the gel groups without nanoparticles are dark, while the Laponite-containing microgels appear bright, showing the uniform distribution of Laponite nanoparticles inside the polymer matrix. Nanoplatelets in $HNM_{0.5}$ were well distributed; only a few aggregates can be observed. More agglomeration of particles was formed at higher concentrations. The area fraction (%) of

agglomerates significantly increased from ~ 4% in HNM_1 to ~ 10% by incorporation of 2% Laponite in the polymer matrix (**Figure 3-6**b). The result further suggests the great potential of this nanomaterial-based drug delivery system for non-invasive monitoring of wound healing in small animal models using μCT [147].”

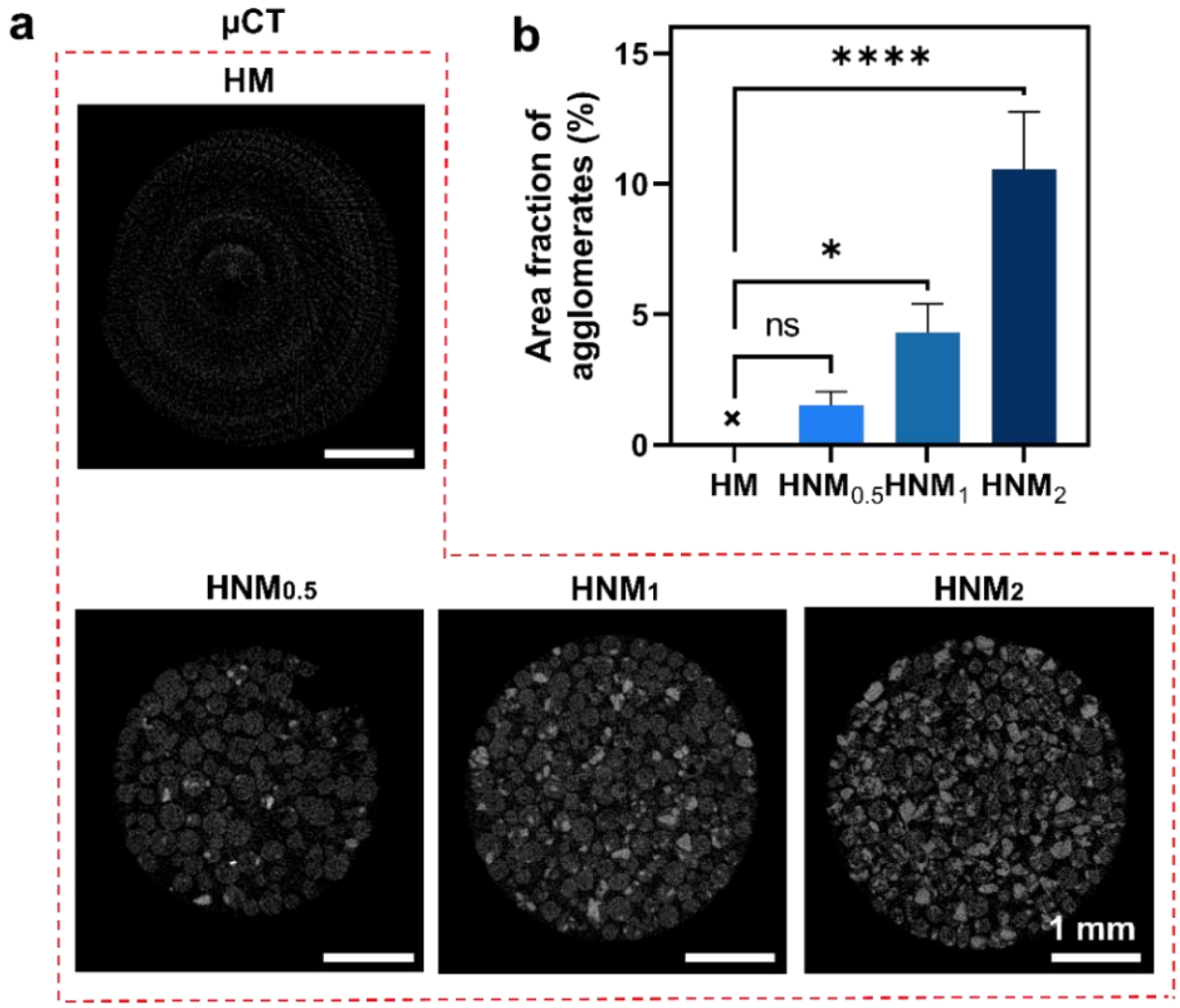

Figure 3-6 “(a) μCT images showing the nanoparticles distribution inside HM and HNMs. (b) Comparison of the area fraction of agglomerates among HM and HNMs.” * represents $P < 0.05$, **** $P < 0.0001$, n.s. means $P \geq 0.05$, Sample size, $N = 4$.

3.4 Injectability and mechanical properties

"In many cases, regenerative therapy requires administering drugs by minimally invasive approaches [148]. Synthesis and development of microcarriers in injectable forms are thus of vital importance for wound healing applications. The microgel suspensions exhibited shear-thinning behavior, which is important for extrusion through syringe-needle. For example, the viscosity of $HNM_{0.5}$ declined continuously from its highest value at the shear rate of 0.01 s^{-1} to the lowest value at 50 s^{-1} (**Figure 3-7**a). Additionally, the thixotropic property of the microgels was observed using a time oscillatory strain sweep test at periodic low strain (1%) and high strain (500%). The microgel suspension initially showed a solid-like, elastic state at small strain but went through an immediate and reversible transition to a fluid-like, viscous state ($G'' > G'$) upon transition to high strain (**Figure 3-7**b). This behavior can be explained by the disruption of the physical contacts between particles, which is much weaker than the chemical bonds within each microgel. The destruction and stabilization were performed for three cycles, and the microgel suspension recovered ~ 90% of its elastic property in the last cycle. This reversible and thixotropic behavior which is a characteristic of colloidal microgel suspensions enables the granular gel to flow from a needle and rapidly recover after deposition [149, 150]."

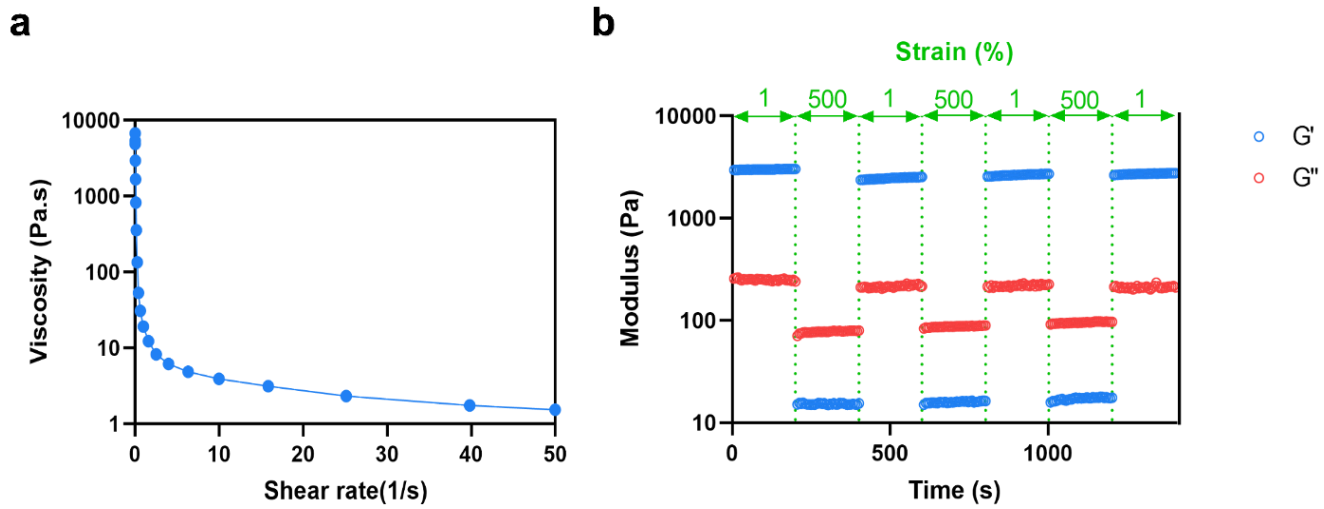

Figure 3-7 "(a) The viscosity of $HNM_{0.5}$ as a function of shear rate (0–50 s^{-1}). (b) shear-thinning and self-healing of $HNM_{0.5}$ through the alternative application of low (1% strain) and high (500% strain) strain cycles."

"For this purpose, the ability to inject microgels into the tissue mimic was assessed using a conventional needle (**Figure 3-8**). Agarose with 0.5% (w/v) was selected as the matrix for the *in vitro* experiment because its rheological properties and water content are similar to those of many soft biological tissues [151, 152]. The shear-thinning properties of microgels allowed the swollen HNMs to be injected through a 21G needle. The microgel aggregate formed a planar depot in close proximity to the needle tip caused by injection-induced fracturing of the agarose gel and the subsequent filling of the cavity by the microgels [151]. Moreover, perpendicular injection created microgel regurgitation in the direction of the puncture point. This phenomenon was observed in a previous study and attributed to the entering flow and the vertical backward flow collide, reducing the injection stream's momentum and stagnation pressure [153]."

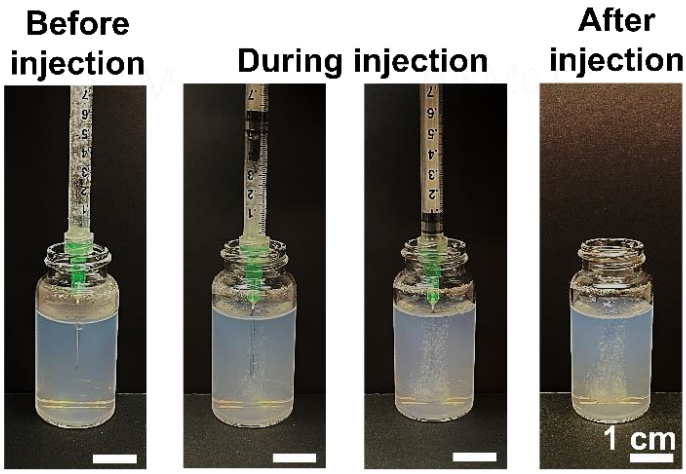

Figure 3-8 "Image showing injection of $HNM_{0.5}$ through 21G hypodermic needle into 37 °C agarose gel."

"The rheological properties of the hydrogels, defined by their dynamic storage modulus (G') and loss modulus (G"), were explored for various compositions. Their modulus-strain diagrams obtained using oscillatory strain amplitude sweep tests are depicted in **Figure 3-9**. Overall, the G' values (characterizing stored energy and elasticity) are much higher than those of G" (characterizing energy dissipation and viscosity), which is typical of highly crosslinked polymeric networks.[154, 155] The yield strain was calculated based on the linear viscoelastic regime (LVE) limit to determine the incipience of failure. This point indicates the beginning of plastic deformations of the samples [156]."

"The G' of PM was ~ 1290 Pa. This sample G' exhibited a linear behavior up to ~ 6.3% strain. The HM had a storage modulus and an LVE limit of ~ 13483 Pa and ~ 21.5 % strain, respectively. Considering the high molecular weight of the hyaluronic acid used in this study, HAMA chains formed a rigid hydrogel as a result of the increased crosslinking density. They also provided intermolecular and intramolecular entanglements, allowing the polymer network to be pulled further before the chains break and leading to an improved stretch ratio [157-159]."

"Results signify the potent role of Laponite content on the viscoelastic properties of the obtained hydrogels. The addition of Laponite to the hydrogel has increased both G′ (~ 15947 Pa) and the yield strain (~ 52.8 %) of the $HNM_{0.5}$. Both positive and negative charges on the Laponite surface lead to their interactions with various functional groups on polymer chains. The ability of the Laponite to provide interaction sites assisted the integration of individual components and toughened the hydrogel through increased energy dissipation capacity under strain. This, in conjugation with the high inherent stiffness of Laponite, explains the enhanced mechanical properties of $HNM_{0.5}$ [160]. The results show that the maximum storage modulus (~ 39116 Pa) was achieved at 1 wt% Laponite content, while the structure breakdown occurred at a lower strain level (~ 33.8 %). The addition of further Laponite content upon 2 wt% caused notably reduced G' (~ 25402 Pa) and yield strain (~ 13.4 %). This trend might be relatable to the agglomeration of excessive amounts of Laponite, which interfere with the interfacial interactions leading to the micro-phase components' separation and inhomogeneity of the structure [161, 162]."

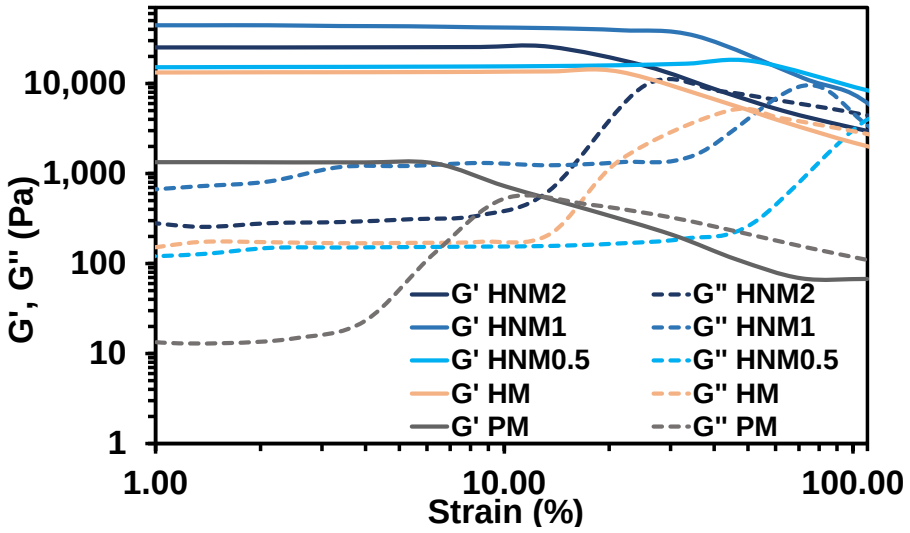

Figure 3-9 "Viscoelastic properties of the hydrogel samples."

"The surface stiffness over a microscopic region, at the micro-scale, commensurate with cellular focal adhesion may differ from the macro-scale bulk properties of hydrogel scaffolds. Therefore, nano- and micro-indentation approaches to quantify local mechanical properties provide useful information about the cell microenvironment.[163, 164] Consequently, nano-indentation was used to quantify the local moduli using atomic force microscopy (AFM). The modulus values were found to be ~ 1716 Pa, ~ 2509 Pa, ~ 4332 Pa, ~ 5666, and ~ 1913 Pa for PM, HM, $HNM_{0.5}$, HNM_1, and HNM_2, respectively (**Figure 3-10**). Due to the impacts of heterogeneity within the gels and the poroelastic nature of the materials, the results from AFM and rheology are not directly comparable [165]. However, Young's moduli measured via AFM follows the same trends as the shear moduli measured via rheology. These results show that nanoparticle loading in moderate concentration increases the storage modulus and the yield strain."

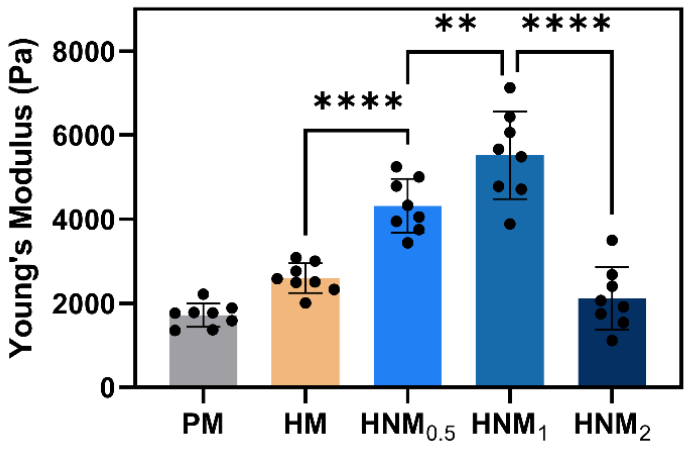

Figure 3-10 "Indentation moduli extracted from AFM mciroindentation experiments for hydrogel samples." ** represents $P < 0.01$, **** $P < 0.0001$, n.s. means $P \geq 0.05$, Sample size, $N = 10$.

3.5 Swelling, drug release, and biodegradation

"The rate and degree of hydrogel swelling are critical factors that reflect the level of polymer/crosslinking density, the hydrophilicity of polymer chains, and pore space. Optimal fluid absorption and stability in the physiological environment regulate the permeability and shape of bioimplants during wound healing and tissue regeneration. The swelling behavior of the microgels was recorded over 7 days, and the results are illustrated in **Figure 3-11**. It can be seen that the addition of HAMA contributed to a significant increase in the swelling ratio for the HM (~ 6.0 g/g) as compared with PM (~ 4.5 g/g). This can be ascribed to mixing high molecular weight HAMA with short-chain GelMA, creating a looser polymer network with a lower crosslinking degree [166]. Moreover, hyaluronic acid is composed of negatively charged polymeric chains with a great tendency to positively charged ions resulting in an osmotic pressure that adsorbs water into the polymer [167]."

"The introduction of Laponite caused the swelling ratio of $HNM_{0.5}$ to increase but that of HNM_1 to decrease. The swelling ratio of the nanohybrid gels increased when the Laponite particle concentration increased up to 0.5 wt% (~ 6.6 g/g), decreased in 1 wt% sample (~ 4.6 g/g), and later decreased (~ 5.4 g/g) upon additional increase the Laponite nanoparticle concentration to 2%. All HNMs reached an equilibrium state sooner than HM. The Laponite nanoplatelets interact with HAMA and GelMA chains through electrostatic interactions, which creates extra crosslinking sites in the polymer network and a consequent reduction in the swelling capacity of the HNMs. On the other hand, previous studies have shown the capability of each Laponite nanosheet to adsorb two ordered layers of water molecules between themselves [168]. This increases the hydrophilic regions of the polymer network and the overall swelling affinity of the system. These two outcomes have been found to vary the effects of different concentrations of Laponite in regulating the swelling rate and water retention capacity of the samples."

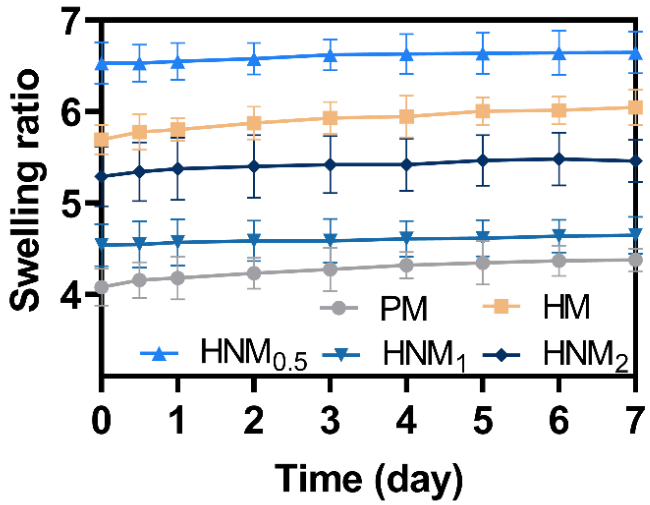

Figure 3-11 "The swelling ratio of different microgels immersed in PBS for seven days, Sample size, N = 4."

"Zeta potential, the net charge that arises at the interface between a solid surface and its liquid medium, is an important and applicable indicator of the surface modification of nanoparticles [169]. Here zeta potential measurement was used to prove Laponite – IL-10 binding (**Figure 3-12**). After drug loading, the zeta potential surged from −44.1 ± 6.1 of pristine Laponite to −36.3 ± 7.8. This could be attributed to the neutralization of a part of the negative charge of the nanoclay by electrostatic interaction with positively charged groups of IL-10 molecules [14, 170]."

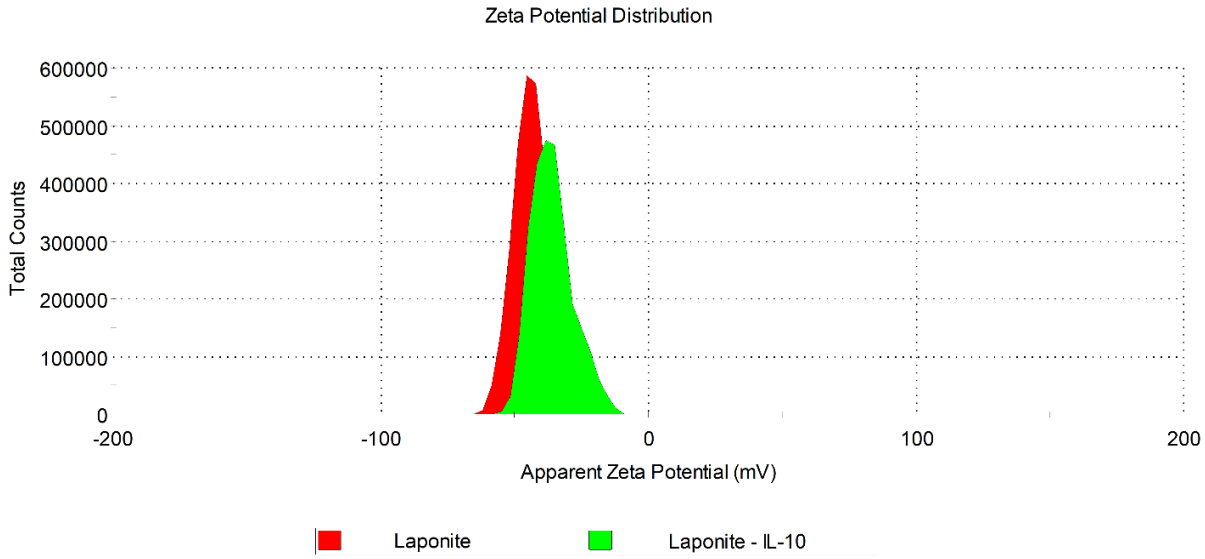

Figure 3-12 "Zeta analysis of pure Laponite and IL-10 – loaded Laponite, Sample size, N = 3."

"To test the ability of nanoclays to slow down the drug release rate from microgels, a fixed amount of IL-10 (2000 ng) was incubated with different concentrations of Laponite before incorporation into polymer solutions. The collection of newly formed HM microspheres resulted in ~ 150 ng protein loss, while Laponite-containing gels lost only ~ 10-50 ng, which is <3% of the encapsulated IL-10. Based on the release profiles, Laponite was able to reduce the rate of cytokine release (**Figure 3-13**). This observation was directly dependent on clay concentration. The IL-10 released from HM quickly stabilized at ~ 1100 ng on day 3, indicating diffusion-dominated drug release [171]. The remaining amount of IL-10 could have been lost during the washing step or ELISA detection. The introduction of Laponite suppressed the early burst release and provided a sustained release of IL-10. After 6 days, the $HNM_{0.5}$ group released ~ 990 ng IL-10. The gels with 1% and 2% concentration resulted in a slower release again (~ 850 ng and ~ 670 ng after 6 days). When blended with Laponite, the IL-10 molecules interact with the clay particles via physical absorption, electrostatic interaction, and hydrogen bonding, resulting in cytokine anchorage within the interlayer space of Laponite nanoplatelets [172]. The fast release from HNMs in the early period is because of the drug fixed in the nanoparticles laying on the superficial part

of the microgels, where the leaching depends only on the ion exchange reaction time and ensues rapidly. The latter slow-release period is related to the protein molecules coming from the inside of the matrix. In this case, the release rate is determined by the diffusion of the counter-anions going in, the exchange reaction, and the ease of diffusion of the drug itself going out [173, 174]."

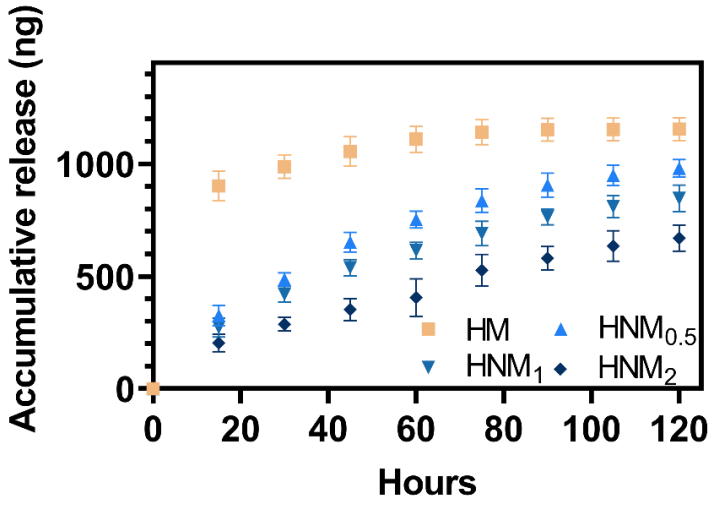

Figure 3-13 "IL-10 release profiles of HM and HNMs, Sample size, N = 4."

"We next investigated how the degradation rates commensurate with the wound healing period [175]. Gelatin-based hydrogels experience both hydrolysis and enzymatic degradation *in vivo* [176]. Thus, degradation studies in enzyme solution were performed *in vitro* by monitoring scaffolds' weight loss over 28 days. The degradation enzyme matrix metalloproteinase-2 (MMP-2) was chosen because it is highly expressed by macrophages during different stages of wound healing [177]. In contrast to all other MMPs, which do not have a gelatin-binding fibronectin domain, MMP-2 has three fibronectin-like inserts in the catalytic domain, which confer its gelatinase activity [178, 179]. According to the measured degradation profiles, shown in **Figure 3-14**, the PM had the highest degradation rate (up to ~ 78% at day 28). Water penetration into the gels caused the cleavage of hydrolysis-sensitive bonds (ester and amide bonds) and MMP-sensitive peptides. Over time, the formation of dangling chains followed by the disintegration of long

polymer molecules into short ones eventually produces oligomers with a low molecular weight that can exit the polymer network [180]. The addition of HAMA slowed the degradation of HM, which degraded only ~ 35% at Day 28. This may be due to the MMP insensitivity of hyaluronic acid, leading to a significant decrease in degradation rate compared to single-chain GelMA hydrogels [181]. The $HNM_{0.5}$ and the HNM_1 microspheres degraded ~ 72% and ~ 64%, respectively, at Day 28. Although nanoparticles could act as physical crosslinking sites within the gel network, the associated promotion of the hydrophilicity of the polymer matrix and the nanoporous structure tend to accelerate the degradation process. There was no significant difference between HNM_2 and HM because of the decreased final concentration of polymer in the 2% microgels."

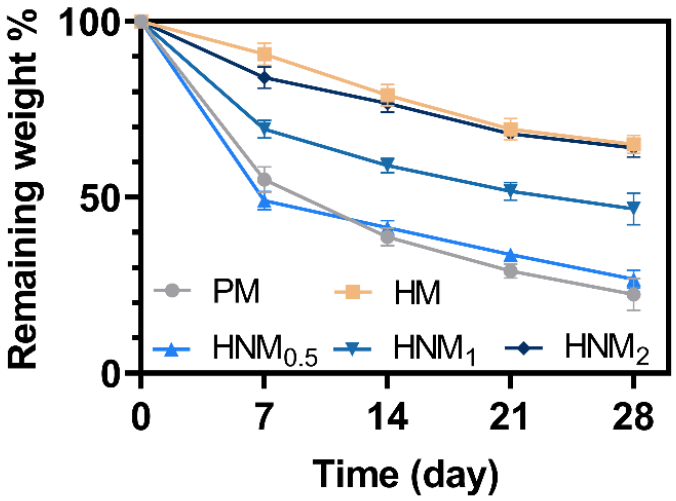

Figure 3-14 "Degradation profiles of different microgels, Sample size, N = 4."

"Morphologies of the microgels degraded for 21 days in enzyme solution are shown in **Figure 3-15**. All microgels demonstrated a noticeable reduction in diameter, which suggested that the degradation process was governed through a surface erosion mechanism. The HM and HNM_2 samples generally retained their spherical shape while the microgel structures in the other samples collapsed. Bridging interconnections were formed in most of the samples, indicating further

annealing of the microsphere hydrogels by degradation at 37℃. However, minimal fusion was observed in the microgels with the highest concentration of nanoparticles, possibly due to the reduced initial concentration of polymer in these samples."

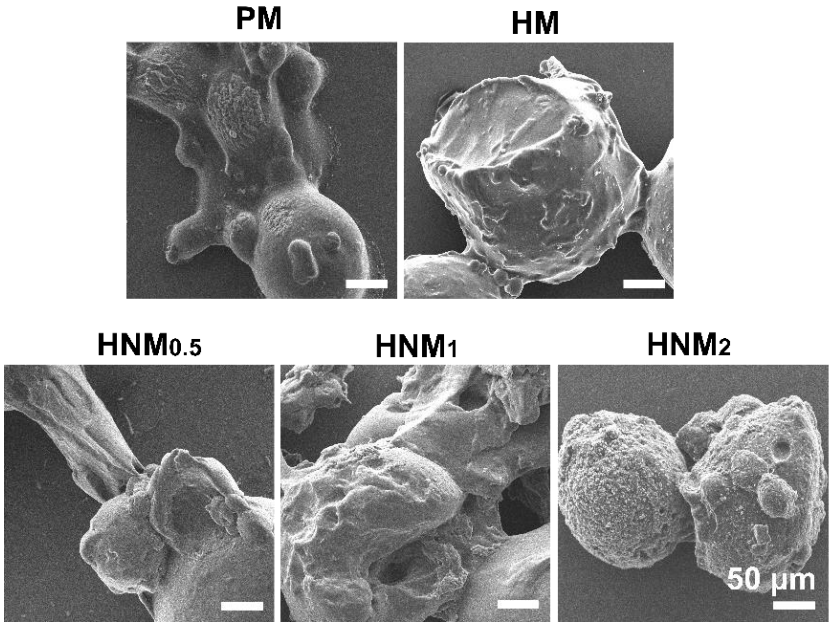

Figure 3-15 "SEM images of microgels after enzymetic degradation for 14 days."

3.6 Cytocompatibility and biological properties

"Vocal fold fibroblasts are the primary source of collagen production in vocal fold fibrosis following injury [182]. The formation of fibrosis tissue significantly changes the composition and biomechanics of the ECM in an irreversible way leading to an unsustainable phonation quality [183, 184]. Due to the problem's importance, human vocal fold fibroblasts (HVFFs) were used as the therapeutic target in this study. As a first step, the fibroblast adhesion and spreading on the microspheres were studied. Representative microscope images are shown in **Figure 3-16**a**.** Fibroblasts display a clear cytoskeleton structure and well-organized F-actin bundles. The Laponite nanoparticle can simultaneously be observed as Laponite and Hoechst link together through electrostatic interactions, giving rise to the blue color of the nanoparticles inside the

polymer matrix. Cells could be seen adhering firmly and spreading well on all microspheres, causing microspheres agglomeration. Upon attachment to nanocomposite microgels, the cells climbed on and conformed to the particles, occupying a larger surface area relative to the gel matrix alone. This behavior was attributed in part to the interaction between nanoparticles and fibroblast surface receptors [185]. The rough and porous surface topology created by the addition of Laponite to the microgels' structure may also have contributed [186]."

"In the next step, the cytotoxicity of the HNMs was investigated. To this end, MTT assays were conducted to assess the proliferation of cells seeded on different microgels. As shown in **Figure 3-16**b, all samples presented a persistent increase in cell proliferation over time. The results also reveal that the seeded cells maintained good viability and proliferation during two weeks. The addition of Laponite did not produce any evident toxicity into the cultured fibroblasts. The highest optical density was attained in the 0.5% Laponite group compared to 0%, 1%, and 2% Laponite microgels. This beneficial impact may be assigned to the porous and homogenous structure of the obtained microspheres. These results align with earlier findings, which displayed the biocompatibility of Laponite-containing gels on various cells and tissues [187, 188]. Considering the overall characteristics of the microgels and to ensure the proliferation of the cultured cells, we chose the 0.5% Laponite microgel as the default HNM in subsequent experiments."

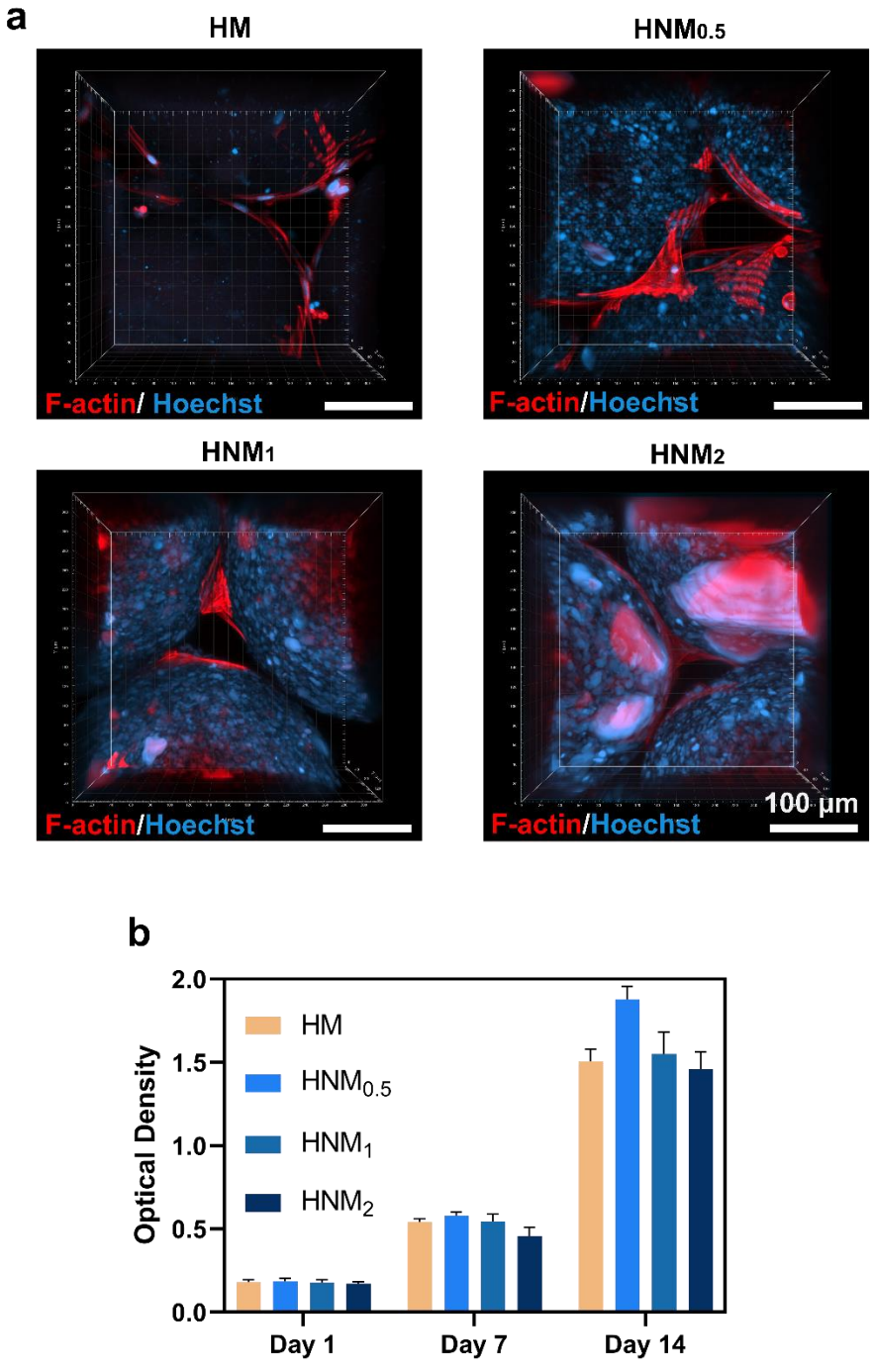

Figure 3-16 "(a) Morphology for HVFFs cultured on microgels at Day 3. (b) Proliferation of HVFFs cultured on microgels at Day 1, 7, and 14, Sample size, N = 4."

“Cell motility and migration are essential for effective and fast regeneration during any wound healing process [189]. Interconnected, micron-scale porosity allows cell migration and penetration within the 3D scaffold architecture. Given the biocompatibility of the nanocomposite gels and the micropores created by inter-microgel space, it can be assumed that the HNMs could support cultured fibroblasts' motility. We performed live time-lapse imaging over 8 h to track and quantify cell movement within a 3D space (**Figure 3-17**a). Within the $HNM_{0.5}$, cells move around microspheres at the average speed of ~ 0.004 um/s and displacement of ~ 52 um (**Figure 3-17**b). These values were very close to those for cells cultured on a tissue culture plate (TCP, ~ 0.004 um/s and ~ 58 um). Cells encapsulated in nonporous hydrogels with a similar composition, on the other hand, performed 'dancing-on-the-spot' movements, i.e., small movements back and forth, without actually migrating away from their original starting point. These findings indicate that the nanocomposite microgels do not hinder microscale movements of cells and thus promote cellular motility.”

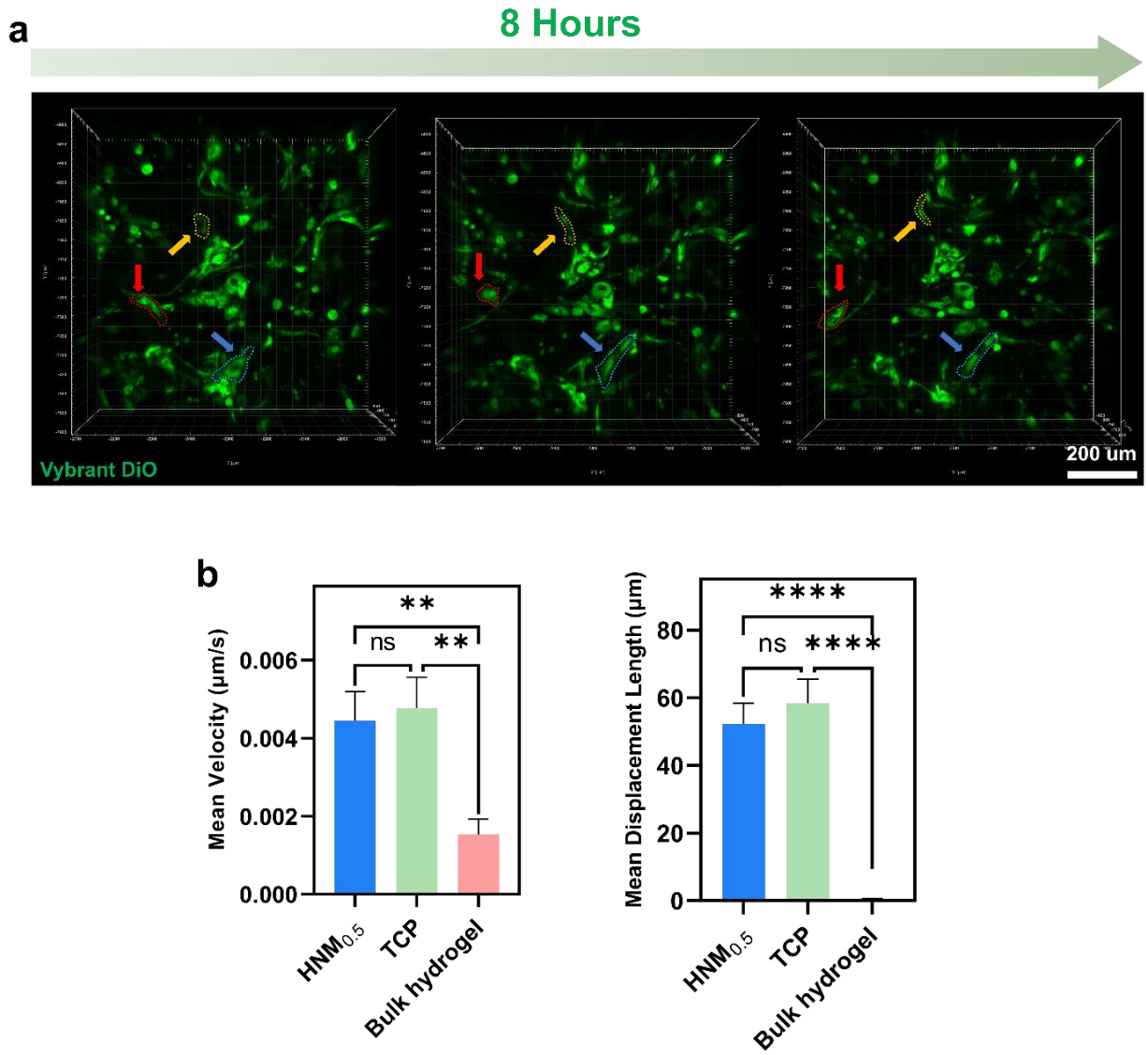

Figure 3-17 "(a) Live imaging of HVFFs moving through the micropores in $HNM_{0.5}$. Three mobile cells are marked with blue, red, and yellow arrows. (b) Comparison of the average speed and displacement of cultured HVFFs among $HNM_{0.5}$, TCP, and bulk hydrogel." ** represents $P < 0.01$, **** $P < 0.0001$, n.s. means $P \geq 0.05$, Sample size, $N = 3$.

"Various cell types involving macrophages express the primary receptor CD44, which interacts with hyaluronic acid via the hyaluronic acid-binding domain (BX7B motif) [190]. This interaction necessitates 3 to 4 hyaluronic acid repeating units (hexasaccharide or octasaccharide)

for binding [191]. Moreover, primary alcohol and carboxylic acid groups take part in the interactions between hyaluronic acid and BX7B motif. Methacrylation, on the other hand, targets the primary alcohols or carboxylic acids in hyaluronic acid disaccharides [191, 192]. Thus, a high level of hyaluronic acid macromers modification may have an adverse effect on their binding to CD44, which could recruit macrophages. Based on previous studies, lower methacrylation of around 20% does not significantly change HA's binding to CD44 [191]. To verify the ability of distinct microgel compositions to attract nearby macrophages, THP-1 cells were imaged after 12 hours of stimulation with macrophage differentiation factor (**Figure 3-18**). The attached macrophages were divided into three crowds according to their position in the culture system: "TCP"—cells attached to the tissue culture plate far away from the microgels; "Border"—cells attached to the microgels on the exposed edges to the floating THP-1; and "Middle"—cells penetrated the microgels far away from the edge boundary."

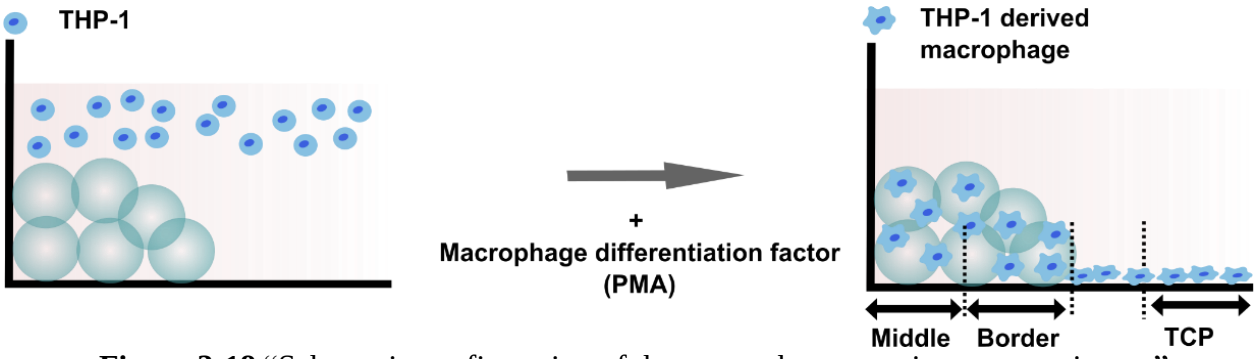

Figure 3-18 "Schematic configuration of the macrophage recruitment experiment."

"As shown in **Figures 3-19**a, b, the density of cells attached to the dish at the border edges in all of the microgel-containing groups was similar to that of TCP group. Low cellular density (~ 5475 cells/mm^3) was detected in the scaffold region near the border of PM **Figure 3-19**c. The density was further diminished toward the center of the scaffold (~ 3605 cells/mm^2). But the cell density at the border (~ 8365 cells/mm^3) and inside (~ 6473 cells/mm^3) of the HM scaffolds was ~ 1.5-2 folds higher than those in the pure samples. This suggests the promotion of recruitment of differentiated macrophages in HAMA-incorporated microgels. No significant differences in cell density were found between the HM and HNM$_{0.5}$ samples (border: ~ 8284 cells/mm^3, middle: ~

6193 cells/mm^3). The finding indicates that the addition of nanoparticles did not hinder the attraction of the macrophages to hyaluronic acid chains."

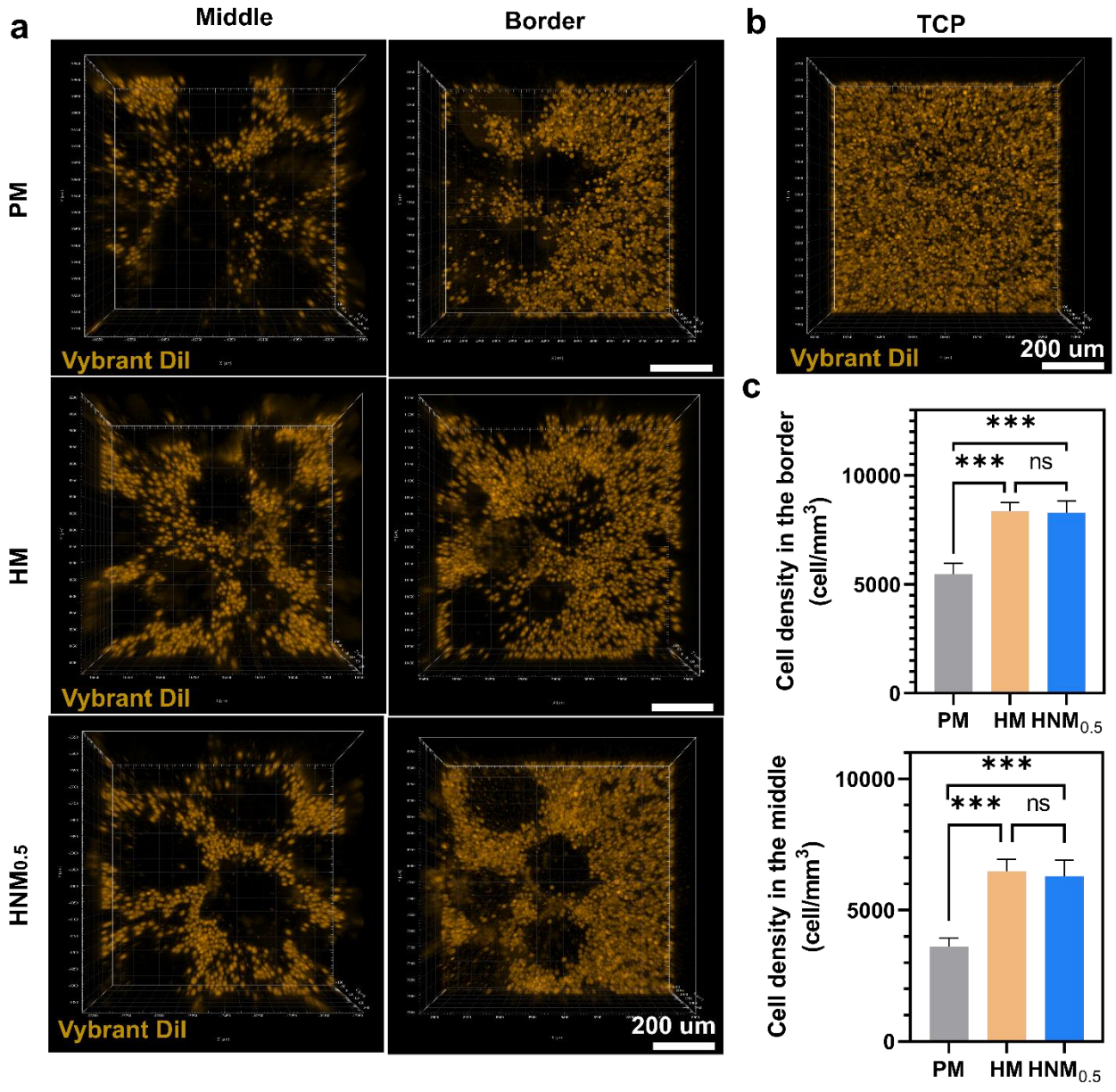

Figure 3-19 "(a) Confocal images showing macrophage distribution within PM, HM, $HNM_{0.5}$, and (b) TCP after 12 hours. (c) Comparison of cell density at the border and in the middle of microgels." *** represents $P < 0.001$, n.s. means $P \geq 0.05$, Sample size, $N = 3$.

3.7 Macrophage/fibroblast co-culture

"THP-1 differentiated macrophages were added to the IL-10-loaded HNMs ($HNM_{x+IL-10}$) using a transwell system to mimic the resident macrophages and their role in wound healing (**Figure 3-20**)."

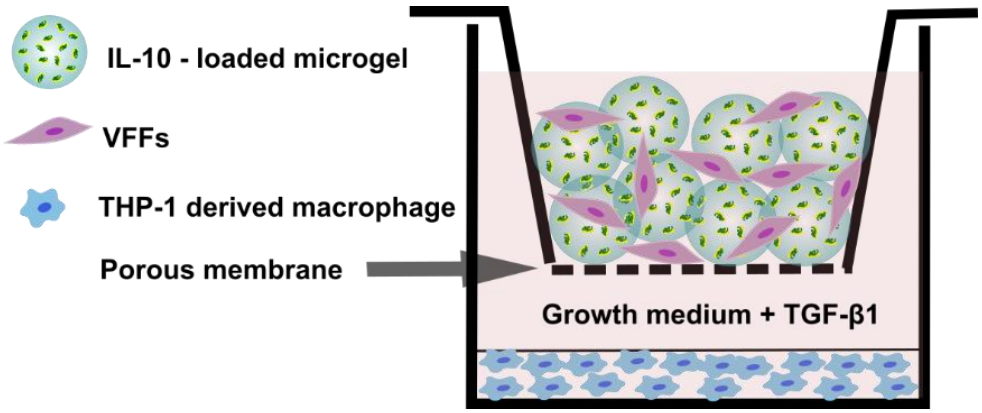

Figure 3-20 "Schematic of macrophage and HVFFs co-culture configuration."

"The secretion of IL-10 is commonly used as an indicator for diverse M2 macrophage phenotypes [193]. IL-10 is also known to be highly expressed by M2c.[194] That is why we evaluated the cellular source of IL-10 in supernatants of the co-cultures after two days of the microgels removal. A high supernatant IL-10 level of around 2 ng/mL was observed in macrophages treated with IL-10-loaded HNMs (**Figure 3-21**). The measured values of IL-10 concentration are in line with former in vitro [195] cell culture, and in vivo studies [196]. A previous survey quantified the IL-10 production of IL-10 stimulated macrophages and detected quantities, 50 pg/mL for 1 × 104 cells/ml, similar to those in our setup, ≈2000 pg/mL for 5 × 105 cells/ml [66]. Moreover, IL-10 concentrations of 1200 – 5000 pg/mL induced de-differentiation of myofibroblasts through opposing the effect of TGF-β1 [63, 66]. Supernatants from co-cultures without IL-10-loading exhibited a significantly lower IL-10 concentration in either TGF-β1-induced or unstimulated microgels. This finding was predictable as TGF-β1 is supposed to induce myofibroblast differentiation and increase collagen-I formation but not cause

enhanced IL-10 secretion by the macrophages. These results also confirm that paracrine signaling from fibroblasts does not affect the IL-10-production of macrophages [66].”

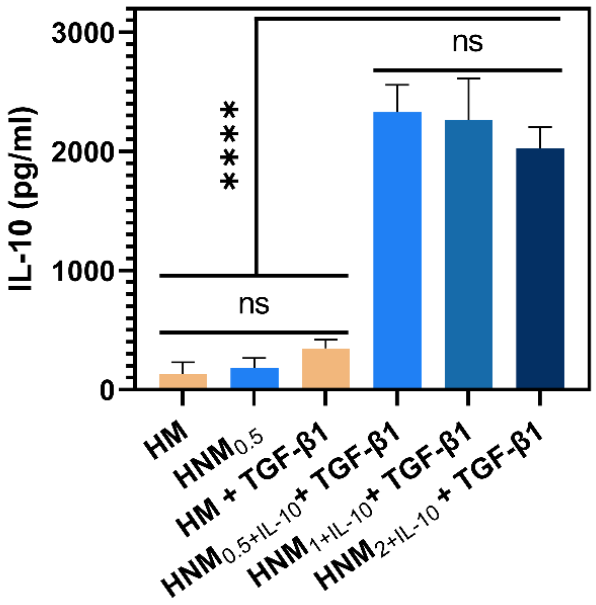

Figure 3-21 “Cellular production of IL-10 by macrophages in co-culture with fibroblasts.” **** represents $P < 0.0001$, n.s. means $P \geq 0.05$, Sample size, $N = 4$.

“Immunofluorescence staining was used to identify alternatively activated macrophages (M2c) with the antibody against the M2c marker, CD163 (**Figure 3-22**a) [197]. Confocal imaging data were also quantified to be comparable and informative. Image segmentation is a process in which the parts of an image that correspond to distinct objects are identified (for example, the identification of a specific marker in cellular images) [198, 199]. Therefore, we evaluated the intensity sum values for the green channel in each group by an object-based 3D-surface segmentation method using Imaris” (**Figure 3-22**b). “Macrophages co-cultured with IL-10-loaded microgels had exceptionally bright and ~ 3-fold higher CD163 intensity than the IL-10 free groups. Our data suggested that the released IL-10 polarized M0 into M2c.”

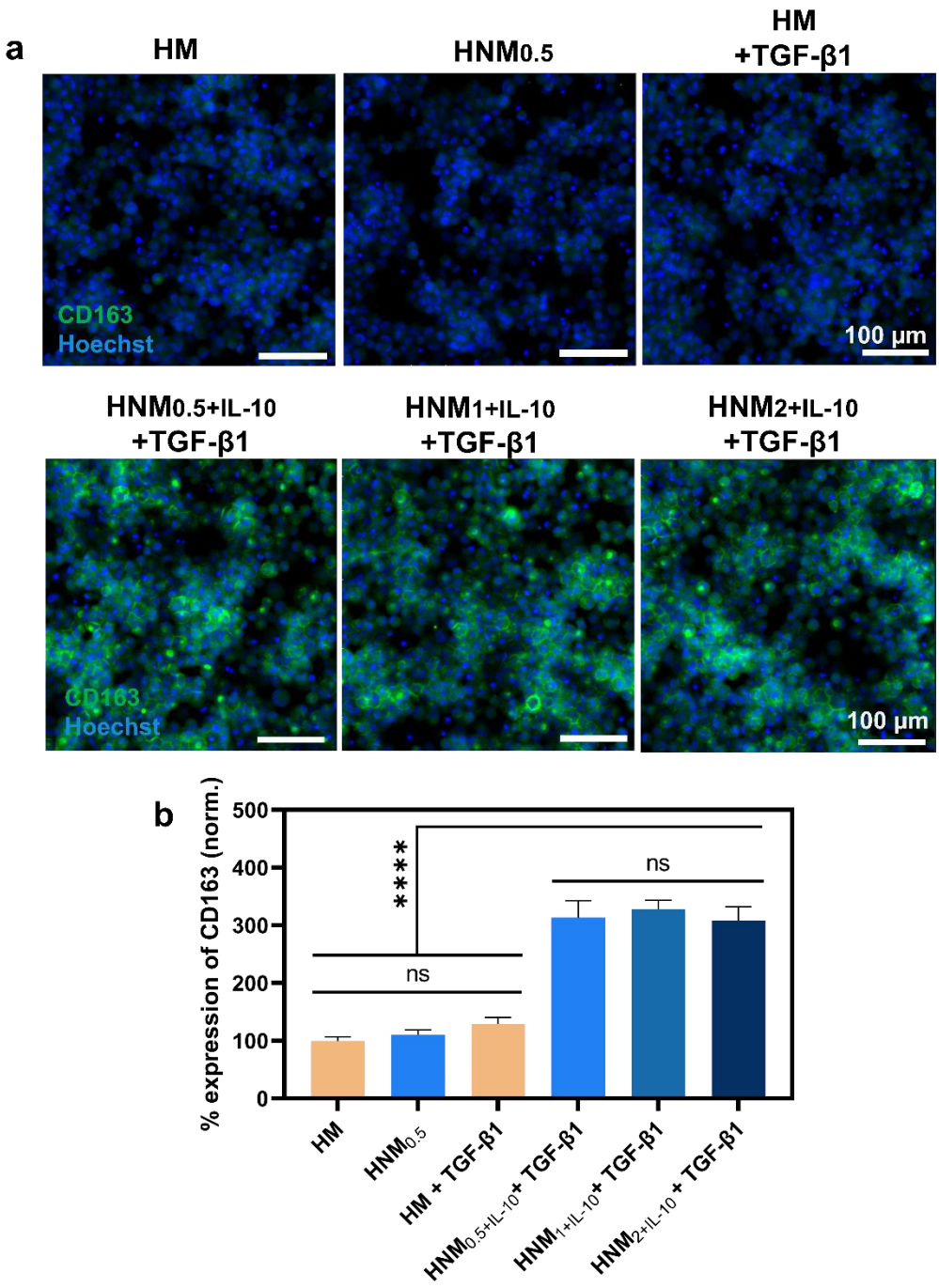

Figure 3-22 "(a) Confocal imaging showing expression of CD163 in co-cultured macrophages after 8 days. (b) Quantifications of CD163 expression by the macrophages in different groups (the

HM signal was set as 100%).” **** represents $P < 0.0001$, n.s. means $P \geq 0.05$, Sample size, N = 4.

“Pro-fibrotic cytokine TGF-β1 is upregulated in various stages of wound healing. When exposed to TGF-β1, fibroblasts increase collagen-I deposition, creating scar tissue and fibrosis.[73] Therefore, it is essential to investigate whether the continuous release of IL-10 could neutralize the pro-fibrotic effects of TGF-β1 in HVFFs. The effect of the IL-10 loaded and non-loaded microgels were studied through immunocytochemical staining of collagen-l in fibroblasts after 8 days of co-culture with macrophages (**Figure 3-23**a, b). Collagen production of unstimulated healthy HVFFs grown on HM and $HNM_{0.5}$ scaffolds was assessed as a control. The results were quantified through the segmentation of the collagen-I channel (**Figure 3-23**c). At baseline, stimulation with TGF-β1 alone contributed to a considerable increase in cytoplasmic collagen-I. Fibroblasts treated with IL-10 in combination with TGF-β1 displayed ~ 2-folds lower collagen-I expression than TGF-β1 stimulation alone. No significant differences were noticed in the levels of collagen-I production neither among the three IL-10 -containing microgels nor between these groups and controls. Our findings indicate that the IL-10 -loaded HNMs reduced TGF-β1 mediated collagen-I production through the paracrine influence of IL-10 secreted from M2c in the co-culture system.”

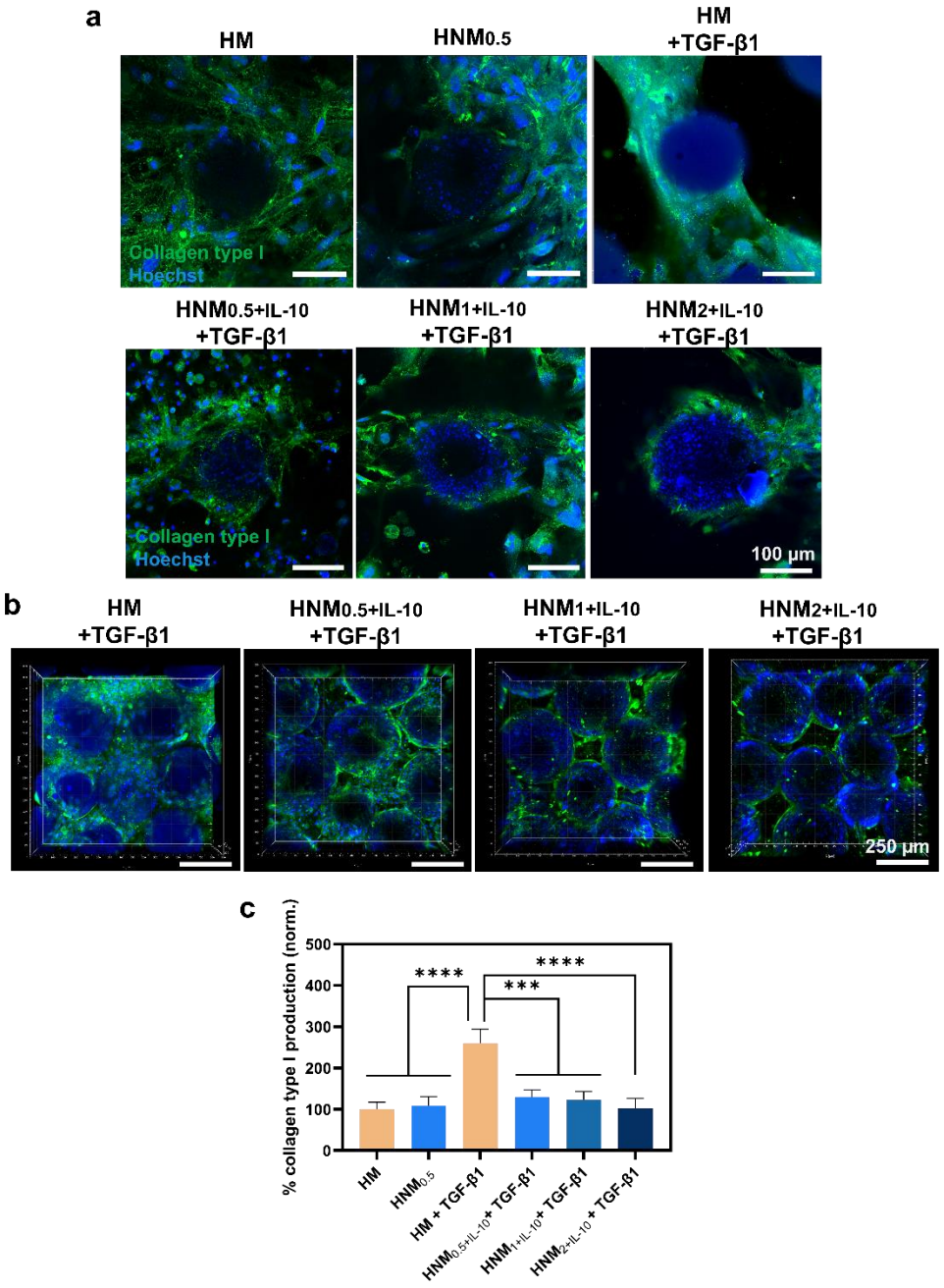

Figure 3-23 "(a) high and (b) low magnification confocal images of Collagen-I secretion by HVFFs after 8 days of culture on different microgels. (c) Quantifications of collagen-I production by the HVFFs in different groups (the HM signal was set as 100%)." *** represents $P < 0.001$, **** represents $P < 0.000$, Sample size, $N = 4$.

3.8 Discussion

Several studies examined the delivery of immunomodulatory cytokines agents, such as IFN-γ, IL-4, anti-TGF-β, and IL-10 and their effect on modulating macrophage activity (**Table 3-2)**. However, the resulting drug-releasing hydrogels are either nanoporous or non-injectable. Moreover, the protein molecules are usually physically entrapped into the hydrogel network. Covalently conjugating the protein to the polymer backbone has been explored to prevent the burst release but at the expense of reduced bioactivity.

Table 3-2 Immunomodulatory biomaterials with biological cytokine release.

Scaffold	**Biomolecule**	**Loading method**	**Microporous**	**Injectable**	**Observed effect**	**Refs.**
Decellularized bone	IFNg/IL-4	Physical entrapment/ Chemical crosslinking	Yes	No	Vascularization	[60]
Agarose hydrogel	IFNg/IL-4	Physical entrapment	No	No	Nerve regeneration	[200]
Heparin-modified gelatin microsphere	IL-4	Reversible binding	Yes	Yes	Bone regeneration	[201]
Hyaluronic acid hydrogel	IL-10/ anti TGF-β	Physical entrapment	No	Yes	Reduction of renal fibrosis	[71]

Hyaluronic acid-heparin	IL-10	Physical entrapment, Hydrogel/Microgel Composites	No	Yes	improve cardiac scar thickness	[72]
Hyaluronic acid-heparin hydrogel	IL-10	Physical entrapment	No	Yes	reversal of pulmonary fibrosis	[73]
Pressed Poly(lactide-co-glycolide) microspheres	IL-10 gene vector	Physical entrapment	Yes	No	Modulation of leukocyte infiltration and phenotype	[202]
Alginate nanoparticles	IL-10 plasmid	Physical entrapment	NA	Yes	treatment of arthritis	[203]
Freeze-dried collagen	IL-10 plasmid	Covalent bonding	Yes	No	Stem cell retention	[204]
poly (ethylene) glycol	IL-10/AT-RvD1	Chemical crosslinking	No	Yes	Recruitment of M2c phenotype	[67]

Previously, injectable hyaluronic acid/gelatin microgel-reinforced composite Hydrogel was developed in our group to form artificial niches with tissue mimetic viscoelasticity and biological cues for cell migration [205]. In another study, injectable glycol chitosan/collagen composite hydrogel was synthesized in which the fibrillar structures supported cell adhesion [206].

Another version of these hydrogels was fabricated through dispersing carbon nanotubes within the glycol chitosan matrix. It was observed that even small concentrations of carbon nanotube promoted cell migration towards hydrogels [120]. In this work, we designed and synthesized injectable Hyaluronic Acid/Gelatin Microgel as a carrier for IL-10. We developed a particle-based composite structure to achieve sustained release of protein molecules from Laponite nanoparticles (**Figure 3-24**).

"The design of HNM proceeded according to the following requirements: i) sustained IL-10 release, ii) cytocompatibility, and iii) macrophage attraction. Sustained drug release from hydrogels was achieved by incorporating Laponite nanoparticles into the hybrid polymer network. These discoid nanoparticles carry a high negative charge on their surfaces and a pH-dependent charge on their edges (negative at pH > 9). Due to this and their high specific surface area, Laponite nanoplatelets can establish strong electrostatic interactions with polymer chains and generate a stable nanoscale platelet dispersion. Specifically, Laponite's "House of Cards" nano-structures manifest the excellent ability to adsorb and/or sustainably release drugs or growth factors [207]."

"To date, several studies have reported the successful retention and tunable bioactive release of various proteins after loading into the interlayer space of Laponite [14]. In the acidic milieu of the wound site, Laponite biodegrades into biocompatible and even bioactive products, including Mg^{2+}, Si(OH)4, Na^{+}, and Li^{+} [172, 208, 209]. The release of Mg^{2+} into the wound site has been revealed to ameliorate the inflammatory reaction and increase cellular attachment, proliferation, and healing rate [210, 211]. Moreover, the presence of alkaline substances following dissolution shows pH-buffering capabilities, which can protect pH-sensitive drugs in an acidic environment [210, 212]. Unlike many drug-loaded hydrogels in which a chemical reaction is required to stabilize the proteins into a polymer network, HNMs provide bioactive sustained release into the injury through the physical adsorption of IL-10 molecules into the well-dispersed Laponite nanoplatelets. We also demonstrated that incorporating Laponite nanosheets into the polymer matrix improves the microgels' stiffness and stretchability and increases their degradation rate."

“We hypothesized that the granular hydrogels could combine the benefits of tissue-like structure and interconnected microporosity to satisfy the second criteria. We selected GelMA, which is produced by modification of the lysine and hydroxyllysine amino acids of gelatin and substitution of their free amine and hydroxyl groups with methacryloyl groups in methacrylic anhydride [213, 214]. Such modified gelatin maintains biocompatibility and enzymatic cleavage as it preserves the arginine-glycine-aspartic acid (RGD) and the matrix MMP degradation peptide sequences of gelatin [214]. It acquires desirable radical polymerization through permanent chemical crosslinking because of the presence of methacryloyl groups. The resulting GelMA hydrogels have excellent thermostability for applications that require cell-responsive substrates [215, 216].”

“Hyaluronic acid is a linear hydrophilic polysaccharide consisting of alternating N-acetyl-D-glucosamine and D-glucuronic acid units, which are linked by β-1,4- and β-1,3-glucosidic bonds [217]. Hyaluronic acid is the most common native ligand for CD44, a cell surface receptor that is predominantly expressed in macrophages [218]. Hyaluronic acid has been used either indirectly as active targeting ligand decorating nanocarriers [219] or directly as carriers [220] and *in situ* hydrogels [221] to enhance cellular binding and facilitate specific drug delivery. The presence of a methacrylate moiety on the hyaluronic acid backbone creates chemically crosslinkable hydrogels with one-step synthesis and good biocompatibility. To fulfill the third requirement, we constructed a hybrid network system comprising different polymer sequences, GelMA and HAMA, covalently bonded via their methacrylate groups.

“Our hybrid hydrogel combines gelatin's mechanical features and cell-interactive functional groups [181] with the unique viscoelasticity [222] and macrophage binding affinity [223] of hyaluronic acid. These new hydrogel microspheres facilitate fibroblast attachment and motility through inter-sphere spaces and also exhibit higher macrophage infiltration and a greater extent of M2c macrophage polarization compared to control groups with no functional components.”

“Co-culture studies of macrophages and fibroblasts treated with TGF-β1 show significantly lower collagen- I production in the IL-10 - releasing sample than in the drug-free group. It should

be noted that in-vitro assays are incapable of replicating all the complex processes mediated by many factors and cell types in the human body during wound healing. In addition, the use of cells from two separate human donors eliminated the possibility of a direct co-culture due to the phagocytic function of macrophages. As a result, the lack of juxtacrine signalling reduced the efficacy of fibroblast-macrophage crosstalk in co-culture."

"Overall, our *in vitro* results are highly encouraging and support the primary goal of this research – the initial development of macrophage recruiting IL-10 -loaded microgels with the potential to attenuate fibrosis through modulation of pro-regenerative macrophage phenotype. These findings support the potential benefits of these microgels when used as drug-releasing substrates for regenerative therapy."

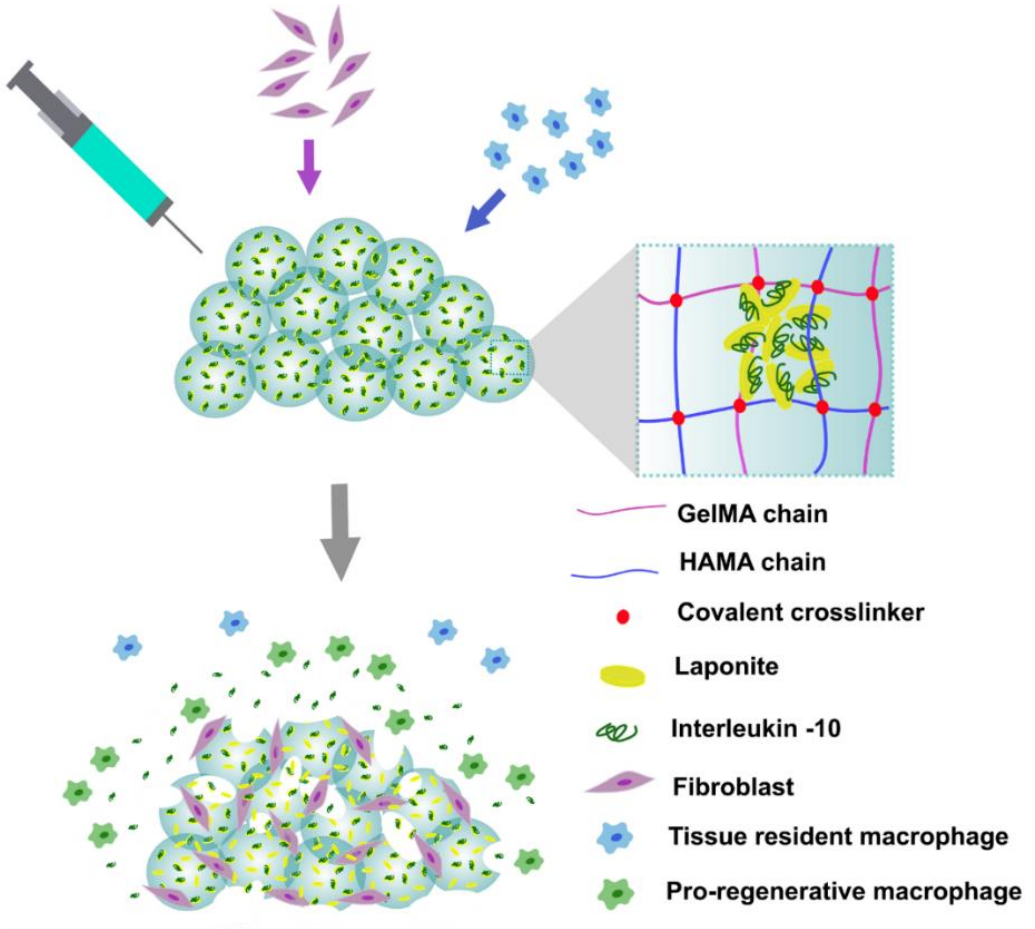

Figure 3-24 Design of hybrid nanocomposite microgels (HNMs).

Chapter 4 Injectable, pore-forming, double-network hydrogels with immunoregulatory properties

This chapter presents a novel strategy to fabricate porous double-network (PDN) hydrogels with various pore sizes. The fabricated PDNs were subjected to physical, rheological, and biological tests. The pore size of the hydrogels was measured based on two different imaging techniques to evaluate the porous structure and measure the pore size and porosity of the PDNs. Then, the effect of porosity on the cellular performance of PDNs, such as fibroblast adhesion and proliferation, was investigated. The regulatory effect of the porous structure on the adhesion and pro-healing phenotype differentiation of encapsulated macrophages was assessed. Furthermore, the adhesion performance and hemostasis capability of the PDNs were tested through adhesion energy testing and the rat tail bleeding model. The findings in this chapter shed light on the design of novel injectable immunomodulatory biomaterials for wound healing applications.

4.1 Synthesis of hydrogels

To fabricate PDNs, different formulations of polymer precursor and the related gelling agent were prepared: First, a polymer precursor contained chitosan and gelatin in a diluted acetic acid solution at 37˚C. Second, a relevant gelling agent comprising sodium bicarbonate and mTG was used. Once mixing is initiated, the sodium bicarbonate in the gelling agent elevates the pH of the mixture from acidic to physiological and induces the chitosan phase separation to form the dissipative network [224]. Concurrently, mTG enzymatically crosslinks the gelatin to create the covalently crosslinked stretchy network. The process is chemical-free and cell-friendly. Cell suspension can be added to the mixture prior to injection. We designated the developed hydrogels as PDNnx, where n and x represent the w/v percentage of gelatin content and the mTG/gelatin ratio degree, respectively. The concentration of chitosan for all the PDNs was 1.5%. Nanoporous single-network (NSN) hydrogels made of 5% mTG-crosslinked pure gelatin and porous single-network (PSN) hydrogels made up of 1.5% pure chitosan were used as controls. Gelatin-based

porous single-network (Gel-PSNx,) containing porous 5% mTG-crosslinked pure gelatin were also prepared as the additional controls where z represents the w /v percentage of sacrificing material.

4.2 Microstructure

The PDNs feature an interconnected microporous structure. We fabricated gels with green fluorescent FITC-labeled gelatin and red fluorescent Rhodamine B-labeled chitosan to reveal the distribution of both polymer networks. The three kinds of hydrogels (NSN, PSN, and PDN) were synthesized and visualized with confocal microscopy in a wet state (**Figure 4-1**a). This process does not require air-drying or lyophilization treatment. We also examined the porous structures using SEM (**Figure 4-1**b). Dehydration of the gel specimens was performed using a CO_2 supercritical dryer to avoid drying artifacts. No pores were detected in NSN. This result is as expected since the mesh size of most conventional hydrogels is around 10 nm, far beyond the resolution limit of a confocal microscope. Alternatively, PSN and the PDNs exhibited micrometer-sized pores emerging from the pH change-induced phase separation of chitosan. These results indicated the formation of an interconnected microporous space inside PDNs, confirming the pore-forming capability of the double-network scaffolds.

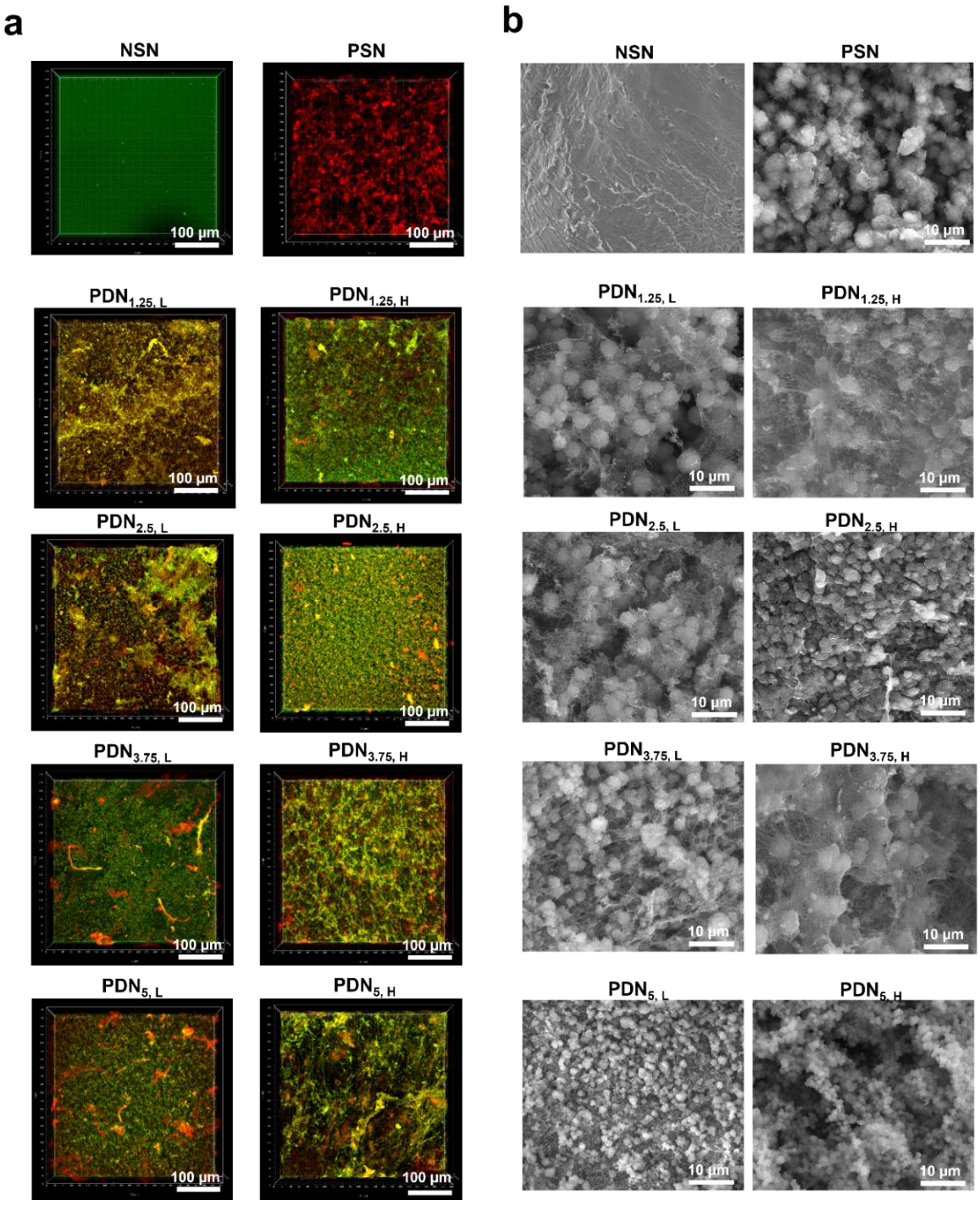

Figure 4-1 Confocal (a) and SEM (b) images showing the porous structures of NSN, PSN, and PDNs.

The porous structure of PSN and PDNs was also proved by the fluorescence intensity distribution (**Figure 4-2**a). One single peak was detected for NSN, confirming a homogenous network. The PSN and PDNs exhibited a broad intensity distribution that involved zones with low and no fluorescence representing chitosan-rich and -depleted regions, respectively [224]. Moreover, the PDNs show excellent integration of the two components at the micro-scale, with both gelatin and chitosan networks segregated into a porous network (**Figure 4-2**b).

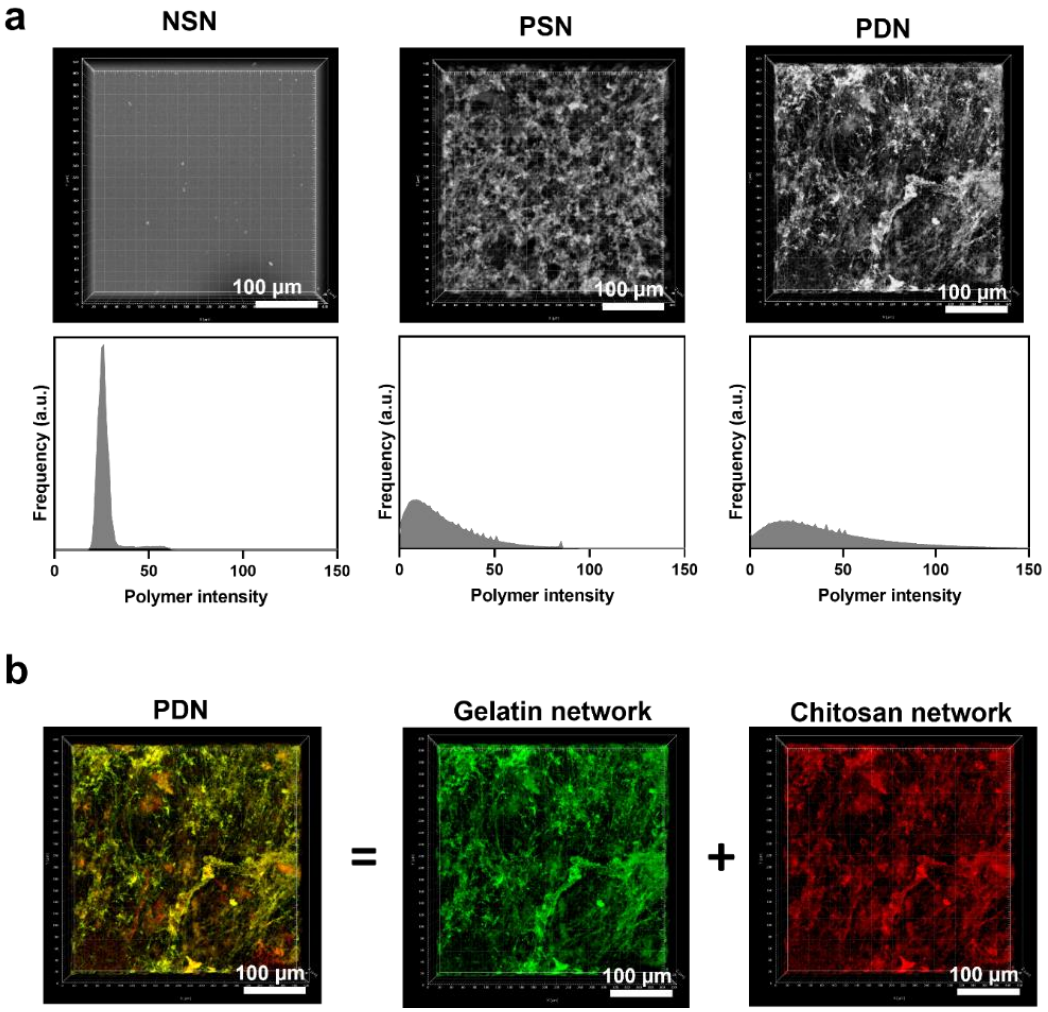

Figure 4-2 Characterization of porous double-network hydrogels (PDNs). (a) Confocal images (top) and fluorescent signal distribution (bottom) of hydrogels. (b) Confocal images show the gelatin phase (green) and chitosan phase (red) within the PDN.

The pore percentage calculation was done by quantifying how much space the polymer network occupies within the gel and subtracting this value from the entire gel volume. Both the pore size and porosity were tuned by altering the amount of the secondary network polymer – gelatin, and its crosslinker, mTG. The average pore size ranged between 6 to 65 μm, which is in the range of cell length (**Figure 4-3**a). The porosity can be adjusted over a range of ~ 21-71% (**Figure 4-3**b). The concentration of gelatin and mTG up to 2.5 % gelatin is conversely proportional to the average pore size and porosity. A reduction in gelatin resulted in slower gelation of the secondary network, to a rate much lower than that of the phase separation of chitosan. As a result, the gelatin molecules have enough time to exit the already formed chitosan network and create a less porous structure. The proportion of the polymer-poor phase is consequently decreased, resulting in smaller pore size and porosity.

Interestingly, a further increase in the gelatin concentration increases pore size and porosity. The largest pore size and porosity were achieved in samples with the highest concentration of gelatin and mTG. This trend may be the result of an interplay between the rate of phase separation and the covalent crosslinking kinetics. As gelatin and mTG concentrations are increased, they speed up the crosslinking of gelatin, hence reducing the mobility of the gelatin chains right after the phase separation of chitosan. This results in the entrapment of gelatin chains within the chitosan network and the creation of a net-like structure. The results demonstrate how the timing of the gelation and phase separation processes can be manipulated to obtain the desired porous structures.

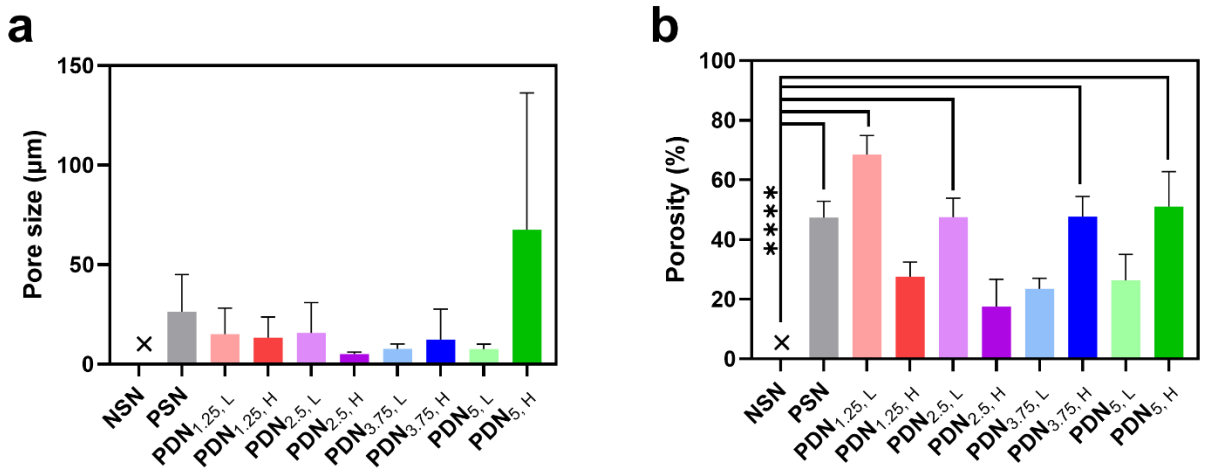

Figure 4-3 (a) Pore size and (b) porosity of NSN, PSN, and PDNs. **** represents $P < 0.0001$.

4.3 Gelation kinetics and stiffness

The gelation of PDNs proceeds through three unified processes: initial solidification, phase separation, and crosslinking. The latter involves both chitosan and gelatin crosslinking. The initial solidification occurs immediately upon mixing, preventing dilution of the gel solution by body fluids. Subsequently, phase separation takes place within seconds. The gelatin also starts to form a covalently crosslinked network immediately. The relative timing of phase separation and gelatin crosslinking is a determining factor leading to interconnected and mechanically stable pores with varying shapes and sizes. Phase separation begins before and independently of crosslinking at low gelatin concentrations. The mobility of gelatin chains at low concentrations is good when phase separation occurs because they have not yet been immobilized by chemical bonds. On the other hand, the phase separates during the crosslinking process of concentrated gelatin. The simultaneous kinetics of the phase separation and relatively fast covalent crosslinking secure gelatin chains' entrapment before they can escape the forming chitosan network. This is crucial to the generation of a larger polymer-poor phase for the desired porous structure.

The modulus-time diagrams are illustrated in **Figure 4-4**a. The storage modulus (G′) and loss modulus (G″) increased while the hydrogels were cured during the time-sweep rheometry tests. All of the gels formed rapidly, and no crossover of the G' and G" time histories was observed. After two hours, the G' values indicative of the storage energy and the elastic properties of gels were much greater than those of G", denoting the energy dissipation and viscosity property. This trend is typical of highly crosslinked polymeric networks. Chitosan formed a stabilized gel in 30 min near 2.5 ka, while gelatin formed a stable gel with similar stiffness in 80 minutes. By combining the two polymer networks, the G' of PDNs stabilized to reach a plateau at varying time periods between 60 and 100 minutes. Furthermore, it is shown that the addition of gelatin up to 2.5 % caused a decrease in the storage moduli (**Figure 4-4**b). It could be concluded that lower amounts of gelatin interrupted the chitosan matrix and its properties without forming any strong secondary network. This effect is much more obvious in $PDN_{1.25,\ H}$, and $PDN_{2.5,\ H}$, in which the greater mTG concentration results in faster gelatin crosslinking and delays the formation of a continuous chitosan network. The addition of a further amount of gelatin (3.75% and 5%), however, causes the storage moduli to increase markedly. These results support the formation of an integrated secondary network which could also create stable hydrogen bonds with the original network. The high polymer content could also contribute to the concentration effect on matrix stiffness.

Further increase of the mTG concentration resulted in a slight decrease of G' in 3.75% and 5% gelatin samples. A high mTG concentration could provide more covalent crosslinks within and between the chains, and could enhance the porous structure of the resulted gels[225]. Surprisingly, the structural integrity of the hydrogels was not disrupted by their highly porous network. This observation may be linked to the microphase separation, which mainly concentrates chitosan in the solid phase to form a strong polymer network. Moreover, the storage moduli were measured at a small strain of 0.1%. Pore collapse occurs mainly for large strain deformations. Therefore, the synergy between those effects slightly decreased the stiffness of the $PDN_{3.75,\ H}$ and $PDN_{5,\ H}$ despite their high porosity.

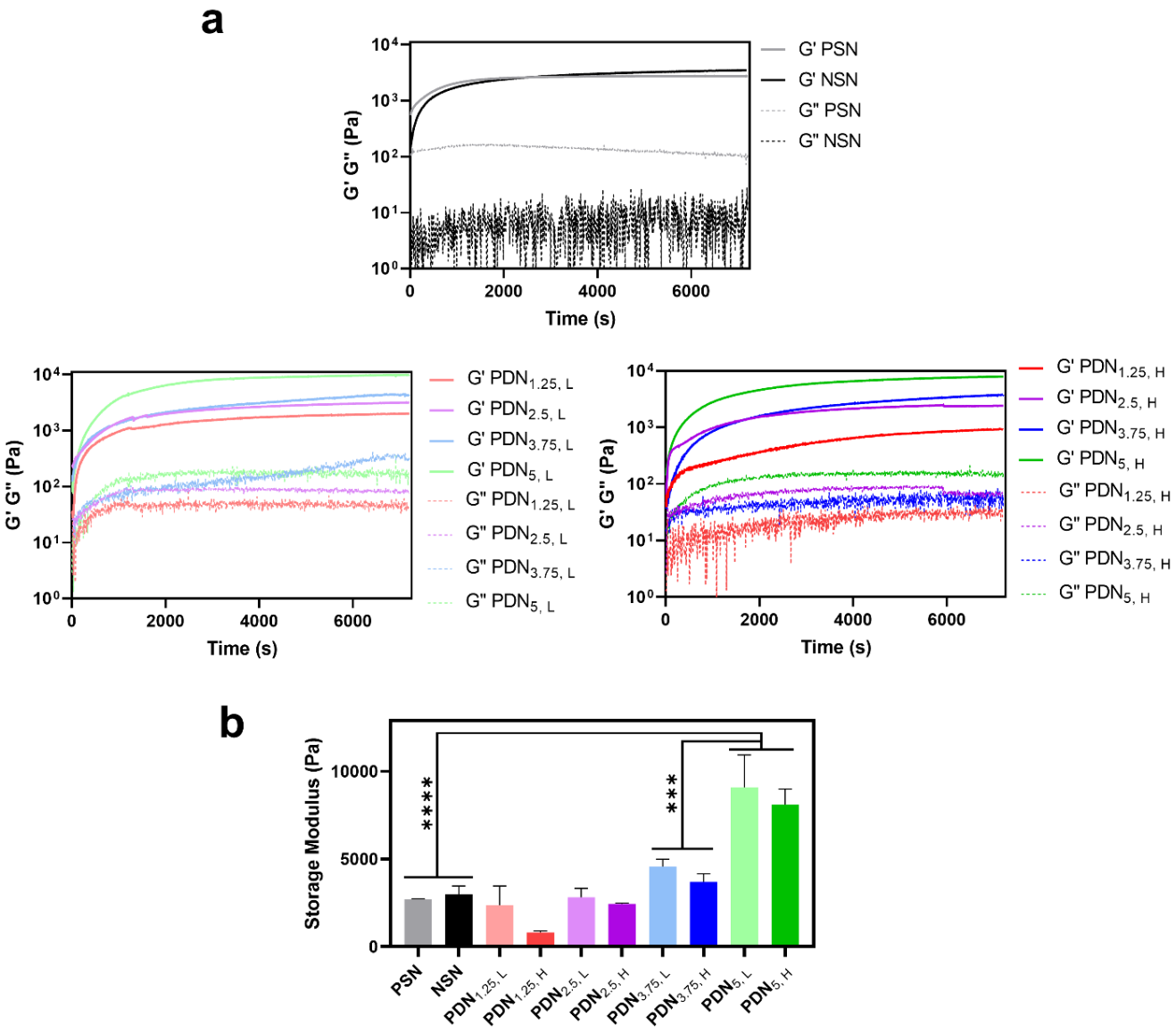

Figure 4-4 Viscoelastic properties of NSN, PSN, and PDNs. (a) Gelation kinetics of different hydrogels. (b) Storage moduli of different samples were calculated from gelation tests. *** represents $P < 0.001$, **** $P < 0.0001$, Sample size, $N = 4$.

4.4 Cytocompatibility

Injectable hydrogels for regenerative therapy must have excellent cytocompatibility. They must stimulate cell growth. The effective control of vocal fold wound healing is important in preventing the formation of scarring and their impaired vibratory structure [41, 226]. Meanwhile, human vocal fold fibroblasts (HVFFs) are one of the main cell types and the primary source of collagen production in vocal fold tissue [227]. Based on this view and with the aim of using the PDNs as a potential scaffold for wound healing applications, the biological characteristics of the different hydrogel compositions were evaluated with HVFFs.

The HVFFs adhesion and spreading within the hydrogels were studied as a first step. Representative microscope images are shown in **Figure 4-5**a. After incubation for 72 h, HVFFs display a clear cytoskeleton structure within the 3D porous matrices of PSN and PDNs. Those cultured in NSN show weak actin staining around the cell nuclei except for a few cells near the surface. This is likely because the nanoporous gel network imposes strong mechanical constraints that impede the proper organization of the F-actin cytoskeleton. The chitosan-containing groups show a stained background associated with the electrostatic interaction between chitosan and Hoechst, as evidenced by the blue color of the polymer matrix. **Figures 4-5**b,c show a substantial difference in cell circularity and density between the porous gels. The PSN has a greater average circularity value higher and a smaller average cell density than the PDN samples, implying poor cell attachment and proliferation. This result was predictable since chitosan lacks cell-binding motifs to modulate direct cell anchorage [228]. In contrast, the gelatin chains contain abundant repeated motifs such as RGD sequences that support integrin-mediated cell adhesion and spreading [229]. Therefore, the HVFFs within almost all PDNs were well spread, displaying the typical elongated morphology of fibroblasts. The $PDN_{5,H}$ cases offered the highest cell elongation and density, indicating that the presence of larger pore size and porosity may facilitate attachment and growth of HVFFs.

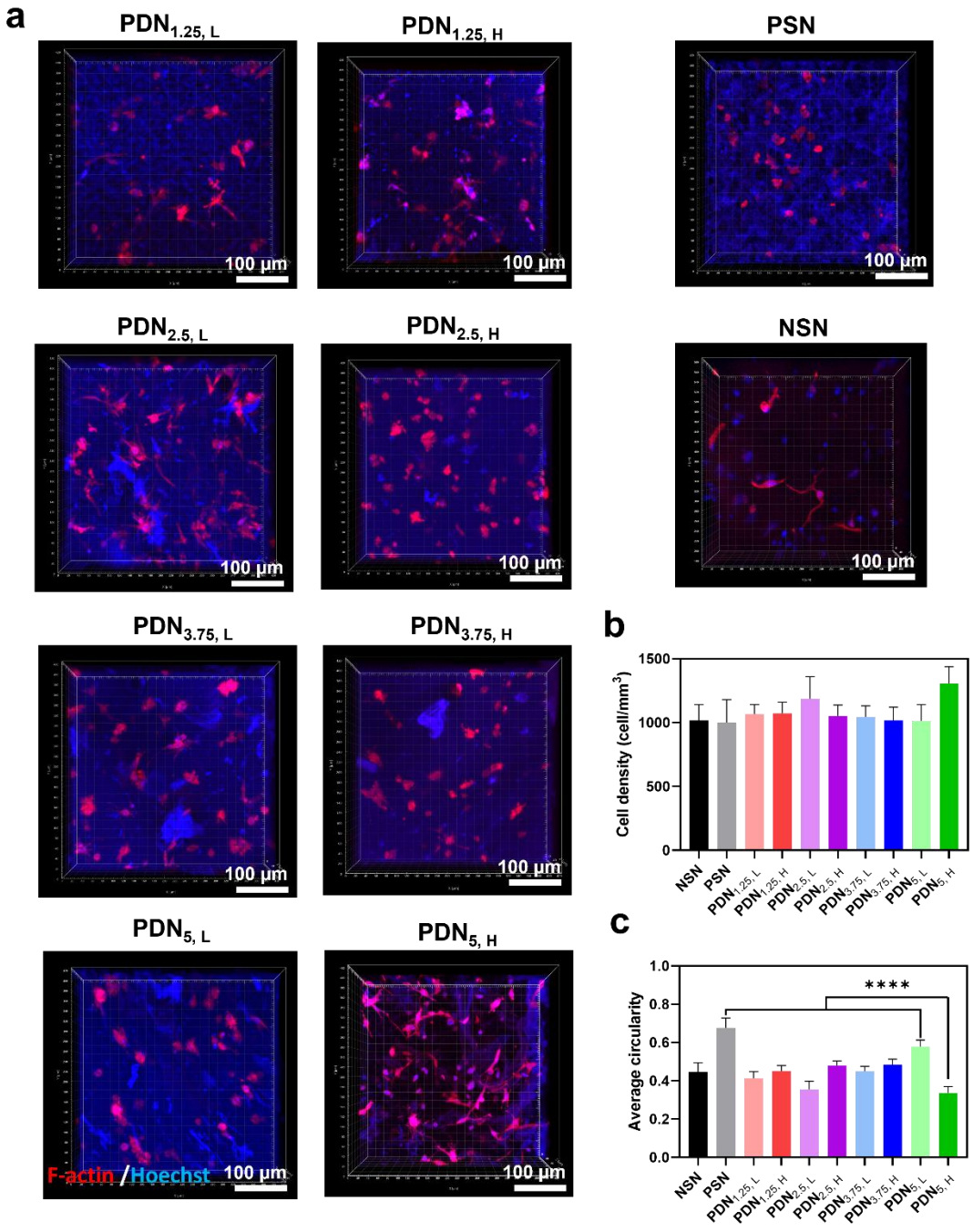

Figure 4-5 (a) Morphology for HVFFs encapsulated inside different hydrogels on Day 7. F-actin is shown in red and nuclei in blue. (b) Cell density and (c) Circularity of cells cultured within different hydrogels. **** represents $P < 0.0001$, Sample size, $N = 3$.

The cytotoxicity of the hydrogels was investigated. To this end, LIVE/DEAD assays were conducted to evaluate the viability and proliferation of HVFFs after 14 days of encapsulation within the hydrogels (**Figure 4-6**a). Based on the results, all the NSN, PSN, and PDNs were found to be cytocompatible. As shown in **Figure 4-6**b, all samples presented cell viability of more than 75% after two weeks. The cell proliferation rate for PDNs was substantially higher than that of PSN and NSN (**Figure 4-6**c). Fibroblasts grew fast within the highly porous matrix of $PDN_{5,H}$ and occupied 70–80% of the entire volume of the 3D structure with almost no dead cells. These results, consistent with the findings of the cell morphology study, indicate the importance of both the gelatin network and the porous structure in modulating cell spreading and growth, thereby improving the final biological behavior of the hydrogel.

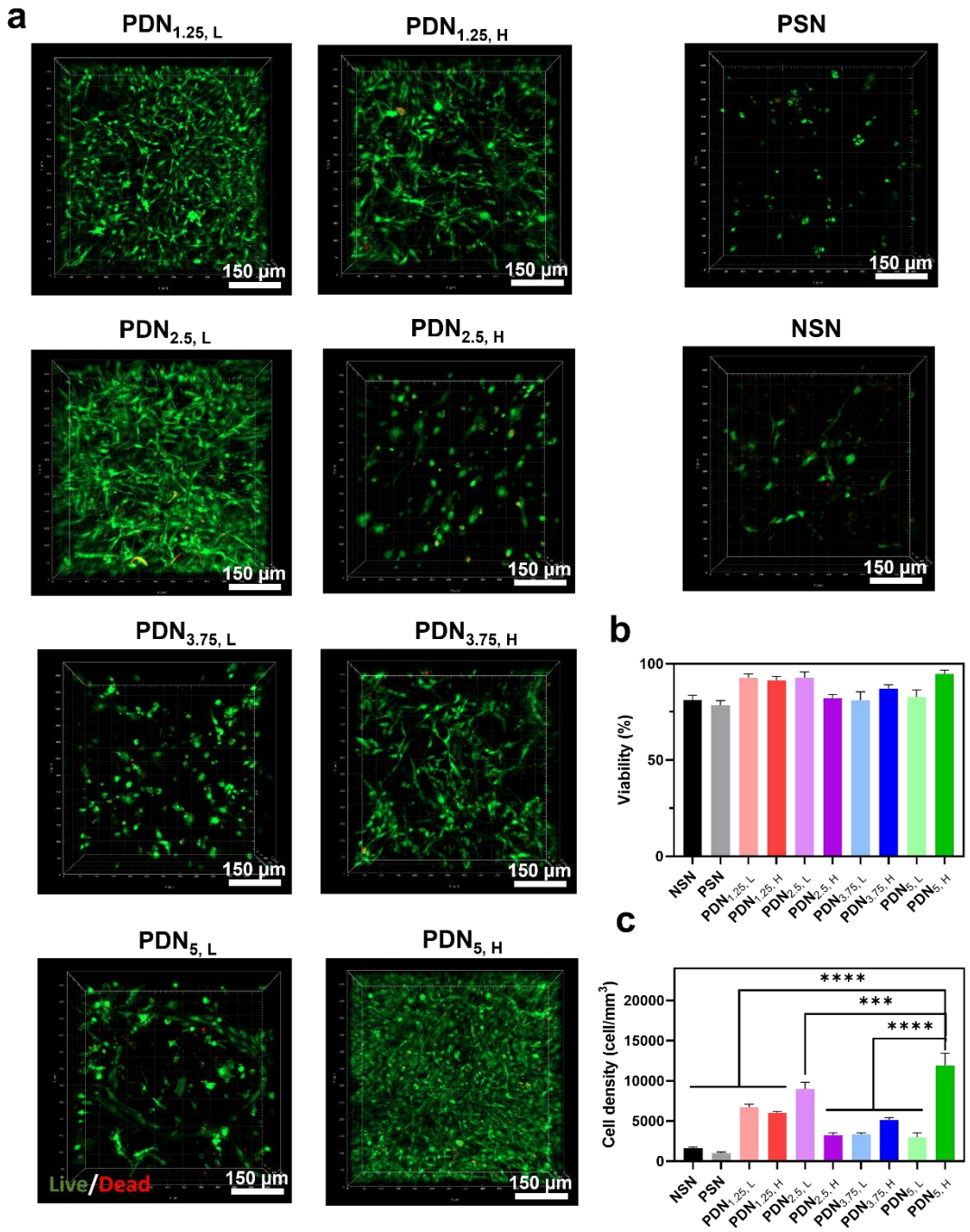

Figure 4-6 (a) Viability of HVFFs encapsulated inside different hydrogels on Day 14. Live cells are shown in green and dead cells in red. (b) Cell viability and (c) density cultured within different hydrogels. *** represents $P < 0.001$, **** $P < 0.0001$, Sample size, $N = 3$.

4.5 Macrophage morphology and M2 marker expression

Having proved the cytocompatibility of the hydrogels, next their capability to support macrophage spreading and polarization was assessed *in vitro*. Immunofluorescence staining was used to compare the morphology and polarization of macrophages after six days of encapsulation within different hydrogels. The signal of the M2 characteristic CD206 was also quantified using an object-based 3D-surface segmentation method using Imaris. As shown in **Figure 4-7**a, macrophages encapsulated within the NSN presented a round pancake-like morphology, while the cells encapsulated within the PSN and PDNs looked flatter and more irregular. Based on the graph shown in **Figure 4-7**b, the degree of cell elongation was higher when encapsulated within the hydrogels with a larger average pore size. A similar result was obtained from the expression of CD206 that was most intense in PSN and $PDN_{5,\,H}$ (**Figure 4-7**c). These findings suggest a strong correlation between the pore size of the hydrogel, macrophage elongation, and M2 phenotype polarization. In scaffolds with large pores, macrophages orient themselves more easily, develop a more natural and spread-out morphology, and acquire the tissue reparative roles performed by the M2s [108]. Previous surveys showed a similar trend with a progressive expression of the M2 markers as the porosity of the scaffolds was increased. These results also align with earlier studies, in which macrophage elongation was reported to promote polarization toward a pro-healing, M2 phenotype [108].

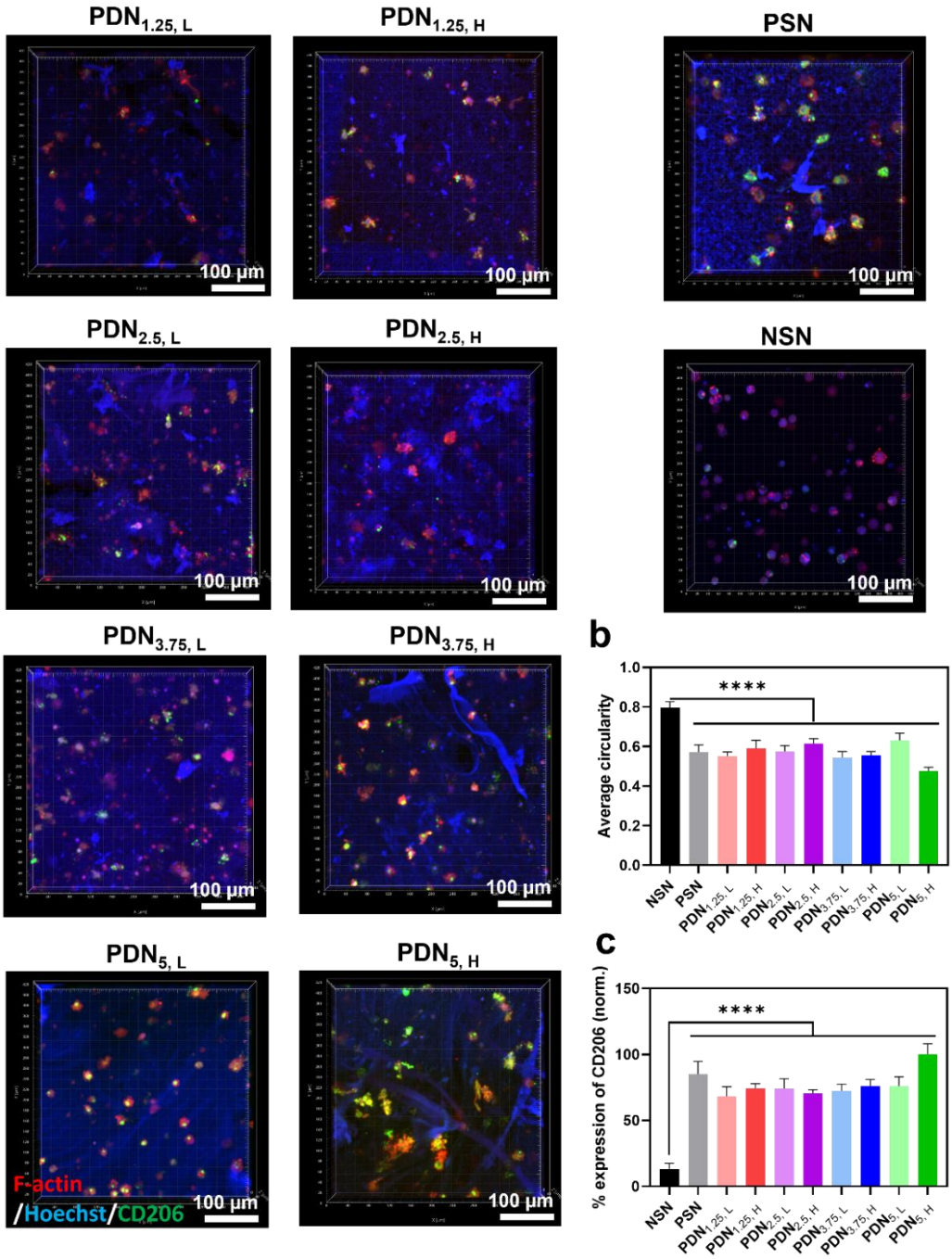

Figure 4-7 (a) Confocal imaging showing cell morphology and CD206 expression by macrophages after 6 days of encapsulation. (b) circularity of macrophages and (c) Quantifications of CD206 expression in different groups (the $PDN_{5, H}$ signal was set as 100%). **** represents $P < 0.0001$, Sample size, $N = 3$.

To further decouple the effect of hydrogel composition effect from those of porosity, gelatin-based PSN with various pore sizes was prepared. To this end, a gelatin solution was mixed with different volumes of PEO solution. The resulted two-phase emulsion is cytocompatible and allows the generation of interconnected micropores upon enzymatic crosslinking. As shown in **Figure 4-8**a-f**,** hydrogels were generated with porosity varying from 55% to 65% and different pore size ranges of 3-42, 4-61, and 4-165 μm. As expected, an increase of the porosity in Gelatin-PSN scaffolds resulted in a decreased circularity and increased cell elongation and expression of the M2 marker. The Gelatin-PSN with the largest pore size showed the highest expression of CD206 but still lower than their counterparts on PDNs, $PDN_{5,\ H}$. These results suggest that in addition to microporosity, the chitosan network also influences macrophage adhesion and polarization. Our findings align with the other studies that demonstrated chitosan's anti-inflammatory activity and its derivatives both *in vitro* and *in vivo*.

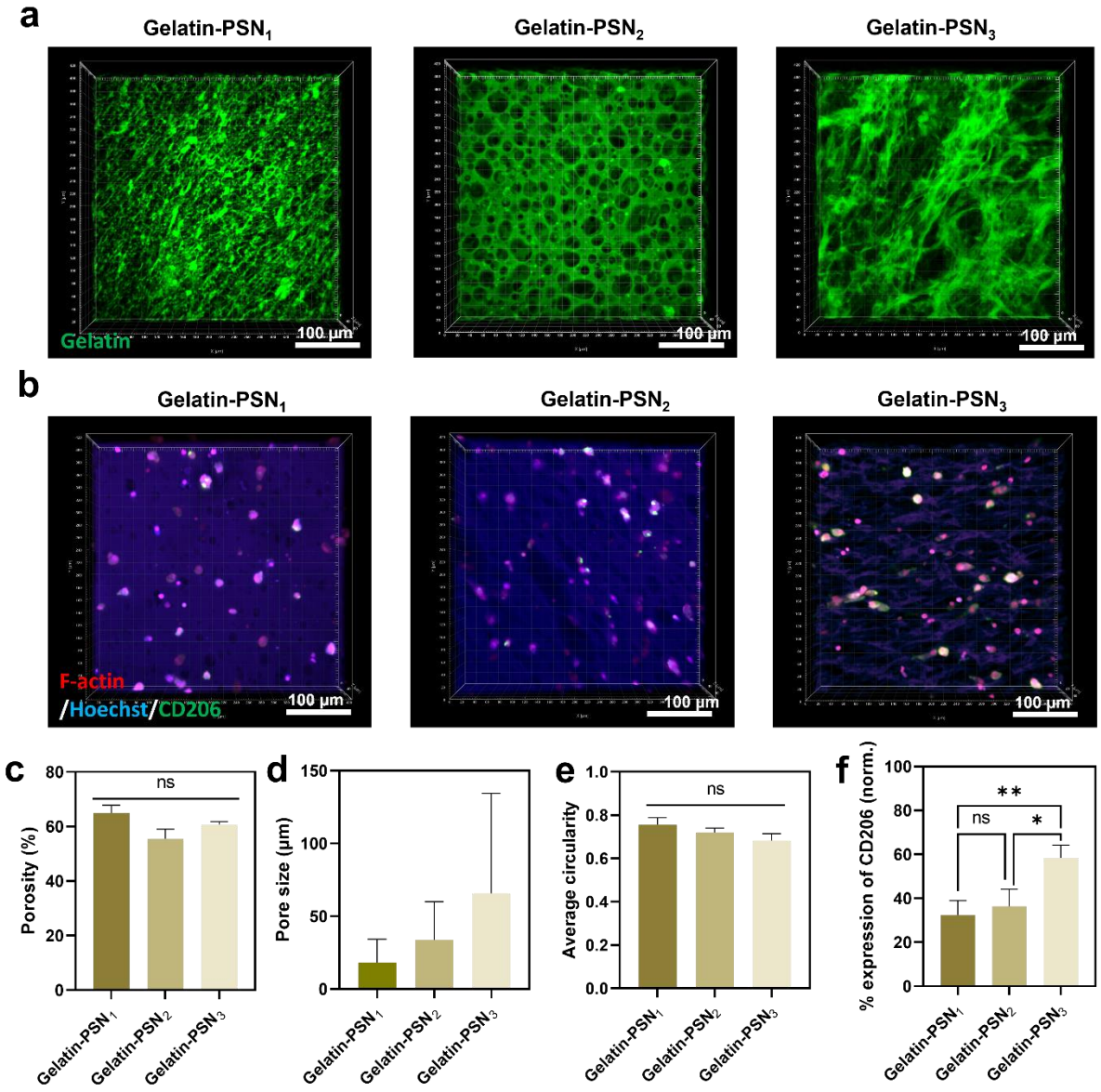

Figure 4-8 (a) Confocal images showing the porous structures of various Gelatin-PSNs. (b) Confocal imaging showing cell morphology and CD206 expression by macrophages after 6 days of encapsulation. (c) Pore size and (d) porosity of various Gelatin-PSNs. (e) Average circularity of macrophages and (f) Quantifications of CD206 expression in different groups (the $PDN_{5,\ H}$ signal was set as 100%). * represents $P < 0.05$, ** $P < 0.01$, n.s. means $P \geq 0.05$, Sample size, $N = 3$.

4.6 Swelling and biodegradability

Swelling behavior is a major factor determining the physical stability of the hydrogels. Thus, the swelling profile of the PDNs was evaluated at various time points throughout seven days of incubation in PBS at 37˚C. All hydrogels maintained their original sizes with less than 10% volume change over one week (**Figure 4-9**a). These results show that the PDNs are mechanically robust and maintain their shape despite their highly porous structure. Good physical stability helps hydrogels preserve their original volume in a liquid environment, which is necessary to avoid unwanted stress on the surrounding tissues [224]. Our results demonstrated that PDNs showed increasingly lower swelling ratios for hydrogel composition containing higher gelatin concentrations. Moreover, the swelling ratio decreased with increased crosslinks at a constant polymer concentration. The tunable swellability achieved by the PDNs is advantageous for their potential range of applications in regenerative medicine. In addition, a reduced swelling ratio of the PDNs at higher gelatin concentrations could possibly improve their adhesive ability *in vivo* [230].

Degradability is another important feature of hydrogels used for wound healing applications. We investigated the *in vitro* degradation of the hydrogels under the action of collagenase and lysozyme, which are potentially present in wound fluid. The NSN was degraded completely after 24 h. On the other side, both PSN and PDN showed a slow degradation profile over an extended period. Gelatin is a known substrate for collagenase, which could cleave collagen fibrils between Gly and Ile/Leu [231], while lysozyme degrades chitosan through specific hydrolysis of β (1→4) glycosidic linkages.[232] The crosslinked gelatin still degraded rapidly because of the large amount of hydrophilic amino and carboxyl groups in the gelatin backbone (**Figure 4-9**b) [232]. The hydrolysis of chitosan was very slow because of the high density of amino groups, which creates complex hydrogen bonding, resulting in a semi-crystalline structure [233]. The degradation profiles of the PDN in this study revealed that chitosan stabilized the double network structure and inhibited the disintegration of the hydrogel during enzymatic degradation [234]. Another plausible explanation for this could be the static electric forces between

chitosan and gelatin, limiting exposure of collagenase-specific sites on gelatin, thus decreasing its degradation rate [231]. Such a slow degradation profile is helpful for proper wound healing, as a period of 2-8 weeks is required for the cells within the scaffold to deposit adequate ECM for the formation of new tissue [117]. Where needed, the degradation process of the PDN can be accelerated by using oxidized chitosan [235].

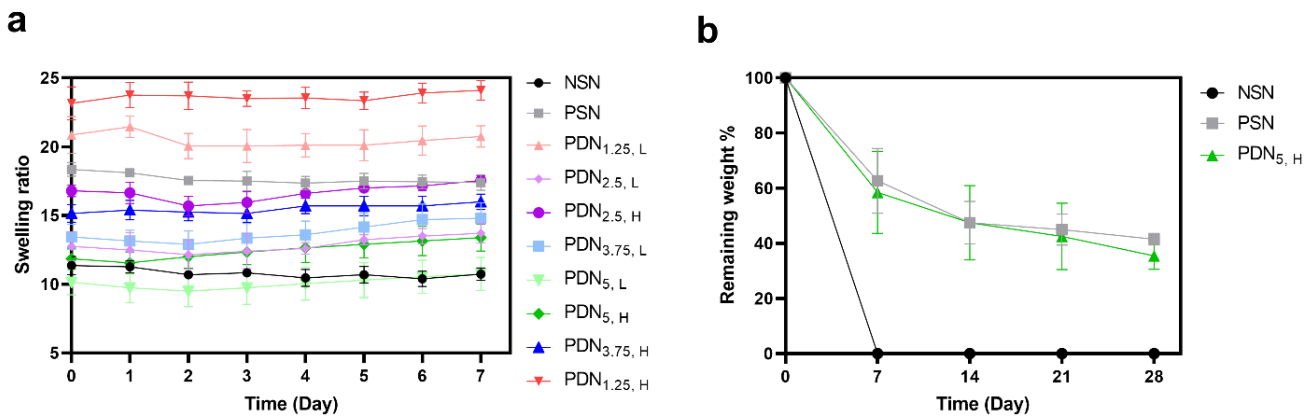

Figure 4-9 Physical stability of PDNs. (a) Swelling ratio of different hydrogels immersed in PBS for 7 days. (b) Biodegradation assay showing the remaining weight of different hydrogels when exposed to an enzyme solution over time, Sample size, N = 4.

Traditional strategies such as sutures, staples, and mechanical fasteners allow immediate closure of the wound but are often accompanied by high localized stress, thereby causing further tissue damage and scarring at the injury site [230]. Alternative methods for noninvasive wound closure and wound healing could facilitate surgical procedures and enhance treatment efficiency by reducing the risk of adverse effects [236]. In particular, tissue adhesives offer advantages such as lower stress concentration by eliminating mechanical mismatch, ease of implementation, enhanced cosmetic outcome, and localized delivery of therapeutic agents [230, 237]. Hence, we aimed to evaluate the adhesive capacity of PDN on various substrates, including collagen casing, porcine heart, and skin tissues (**Figure 4-10**a, b). Peeling PDN from the collagen casing generated adhesion energy of ~76 J m^{-2} (**Figure 4-10**c). High adhesion performance was also achieved across the biological tissues (30-47 J m^{-2}), exceeding the values of fibrin glues and medical tapes (10-20 J m^{-2}). Strong tissue adhesion using PDN could be attributed to both coupling reagent and bridging

polymers. The coupling agent, mTG, offers a chemical-free way to couple the tissues and the PDN, both rich in the primary amine and glutamine groups [238]. Moreover, the highly motile chitosan network within the PDN matrix could act as a bridging polymer that migrates and penetrate the hydrogel-tissue interface. This mechanism ensures reliable contact between the PDN and the substrate [239, 240].

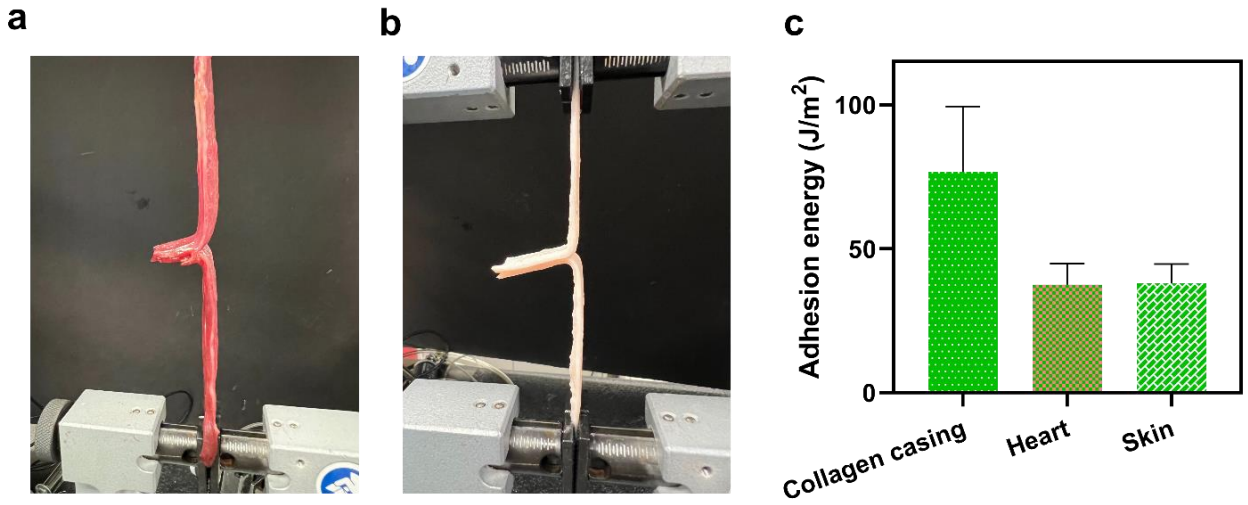

Figure 4-10 Digital photos of the peeling fronts of PDN from (a) heart and (b) skin. (c) Adhesion energy between PDN and various soft substrates, including porcine heart, skin, and collagen casing, Sample size, N = 5.

Injectable hydrogels that can simultaneously stop the bleeding and promote wound healing are beneficial for surgeries or trauma injuries. An ideal injectable hemostatic hydrogel should exhibit rapid gelation to immediately and reliably control bleeding [241, 242]. We employed a rat tail amputation hemorrhage model to evaluate the blood clotting potential of PDNs (**Figure 4-11**a). **Figure 4-11**b shows that the injury untreated with hydrogel took 540 ± 201 s to achieve hemostasis, which is similar to the previously reported hemostatic time on the rat tail amputation model (~ 650 s) [243]. When PDN hydrogel was treated on the injured site, the time for hemostasis obtained was reduced to 138 ± 137 s. No significant difference was detected between the PDN group and the standard gauze treatment group (240 ± 37 s). The mass of blood loss was also less when the PDN (152 ± 140 mg) or surgical gauze (329 ± 220) mg was applied compared to the no-treatment

group (3210 ± 2150 mg) (**Figure 4-11**c). The decreased blood hemostasis time and mass of blood loss for the hydrogel are due to the hemostatic sealing and bioadhesion ability of PDN. Chitosan has inherent hemostatic ability. Charged amino groups on chitosan interact with negatively charged proteins and glycolipids on the surface of red blood cells, causing the adhesion and aggregation of blood cells and therefore providing the PDN with the efficient blood-clotting ability [244, 245]. Moreover, PDN is highly porous, contributing to a large contact area for the interaction with the blood components, thereby accelerating the clotting cascade. Furthermore, the red blood cells and platelets can be trapped within the PDN network. Consequently, the large open pores become obstructed by the blood clotting to avoid transmembrane leakage.

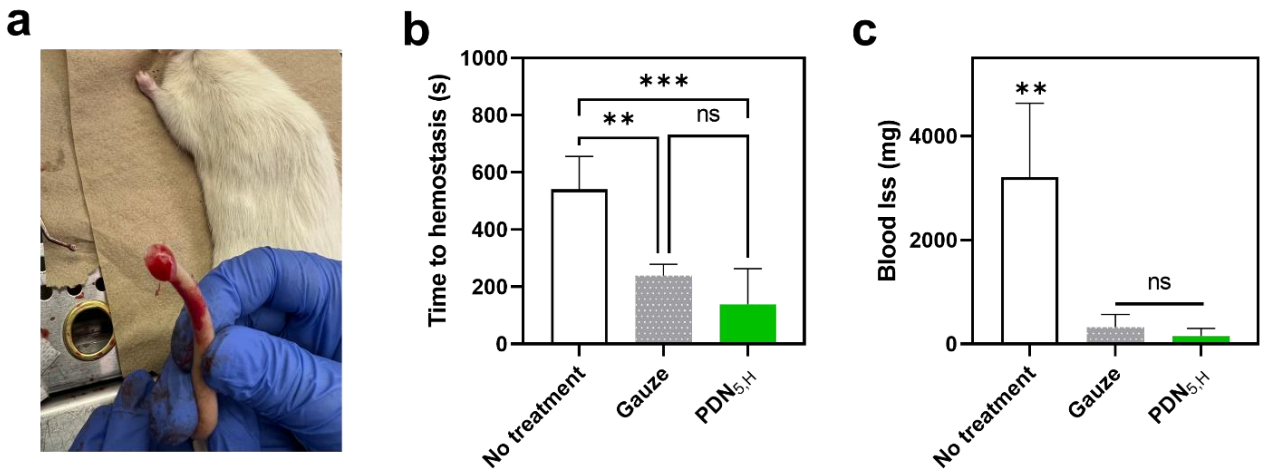

Figure 4-11 (a) Digital photo showing hemostasis ability of PDN. (b) Time to hemostasis and (c) blood loss comparison. ** represents $P < 0.01$, *** $P < 0.001$, n.s. means $P \geq 0.05$.

4.7 Discussion

Recently, a variety of biomaterials have been reported to affect macrophage shape and polarization thanks to their tunable pore size (**Table 4-1**). However, those porous structures are preformed before placement into the body and therefore demands invasive surgical procedure. Moreover, production of these preformed structures usually requires lengthy and complicated

fabrication procedures, such as lyophilization, cryogelation, or 3D printing, as well as awareness about the size and shape of the injection site to design structures that match the irregular cavities.

Table 4-1 Pore size impacts on macrophage behavior.

Scaffold	**Pore generating method**	**Injectable**	**Pore range**	**Desired effect**	**Optimal pore range (μm)**	**Refs.**
Polydioxanone film	Electrospinning	No	14.73 ± 0.62 10.57 ± 0.72 0.96 ± 0.09	M2 polarization	14.73 ± 0.62	[108]
collagen/chitosan hydrogel	lyophilization	No	360 ± 116 160 ± 48	M2 polarization/ angiogenesis	360 ± 116	[109]
Poly(68/32 [15/85 D/L]) lactide-ϵ-caprolactone hydrogel	3D printing /thermally induced phase separation	No	29 ± 0.5 21 ± 0.3 8 ± 0.1	M2 polarization/thinner fibrotic capsule	29 ± 0.5	[79]
Poly (2-hydroxyethyl methacrylate) hydrogel	Sphere templating	No	60 34	Reduced fibrosis/ increased vascularization	34	[106]
poly(ε-caprolactone) fibers	melt electrowriting	No	102.9 ± 3.3 80.7 ± 2.8 59.5 ± 2.0 49.8 ± 1.4 40.0 ± 0.6	Macrophage elongation/ M2 polarization	40.0 ± 0.6	[246]
Poly(95L/5DL)lactic acid - Chitosan hydrogels	3D printing	No	600 ± 93 380 ± 60 165 ± 5	Macrophage elongation /M2 polarization	165 ± 5	247]

Chitosan-containing hydrogels have been developed in previous studies by our research team. Printable hydrogel scaffolds were developed with the PEG/chitosan formulation. The resulting scaffolds were microporous (14-18 μm) and had tunable viscoelasticity that can match that of biological tissues [117]. The combination of chitosan and glycol chitosan networks resulted in the development of Injectable Perusable tough hydrogels. The scaffolds were microporous and maintained physical integrity under prolonged, high-frequency mechanical stimulations in biomimetic perfusion bioreactors [224]. Ionotronic tough adhesives were made from chitosan and poly acryl amide components. The resulted gels also showed high ionic conductivity and stability in electrolyte solutions suggesting their applications as wearable devices and sensor sealants [239]. Liquid-infused microstructured bioadhesives were synthesized with a similar formulation, and through freeze-drying, the obtained hydrogels. The bioadhesives showed an average pore size between 5 and 100 μm and were capable of rapidly absorbing interfacial fluids and active blood clotting [248]. In this study, in situ pore-forming biomaterials are prepared from two natural bioactive polymers that can be injected in liquid form through small-sized needles and go through a sol-gel transition into microporous hydrogels at physiological condition.

The design of PDN was based on the requirements of cytocompatibility, in-situ pore-forming, and immune regulation effect (**Figure 4-12**). We proposed that the phase separation of two natural biopolymers at physiological pH and temperature could guarantee cytocompatibility and generate interconnected micropores upon injection. The first biopolymer is chitosan, a natural cationic polysaccharide with phase separation behavior upon pH alteration. Chitosan has been shown to mitigate the host inflammatory response. Chitosan and its derivatives are commonly used in bioadhesives [249], wound dressing [250], tissue engineering [251], drug delivery [252], and bioprinting[117, 253]. Raising the pH of the acidic chitosan solution to a value higher than its pKa, 6.5, gives rise to continuous polymer-rich and polymer-poor phases [117]. As the polymer-rich phase crosslinks, the polymer-poor phase, primarily consisting of solvent, forms an interconnected network of micro-sized spacings. *In situ* pore formation takes place under physiological conditions, without the inclusion of any chemical agent, and is applicable for cell

encapsulation and delivery [254, 255]. Meantime, the primary amine groups [NH_3^+] of the chitosan become deprotonated and change into [NH_2], which can react with the hydroxyl groups [OH] of the chitosan [256]. This self-crosslinking behavior can strengthen the polymer-rich phase and the created dissipative network [224].

We generated the secondary network with a covalently crosslinked bioactive polymer. Theoretically, we can utilize any polymer that does not interrupt the phase separation of the primary network. In the present study, we fabricated a double network of chitosan and gelatin. Gelatin is a protein acquired from the denaturation of collagen, which is the major protein constituent of many vital tissues in the body [257, 258]. The selection of gelatin decreases the concerns of immunogenicity and pathogen transmission linked with collagen [259]. Moreover, gelatin is far less expensive than collagen [260] and can be readily tailored to achieve polymer networks with a range of mechanical stability and stiffness, being also a great candidate for regulating cell behavior and *in vivo* transplantation [261].

Transglutaminases are innocuous enzymes widely used in the food industry-approved for human intake by the U.S. Food and Drug Administration [262]. The function of transglutaminases involves the catalysis of the reaction between ϵ-amino groups of lysine residues and γ-carboxyamide groups of glutaminyl residues, resulting in the formation of intramolecular and intermolecular ε-(γ-glutaminyl)-lysine isopeptide bonds and formation of a permanent network of polypeptides [262, 263]. These enzymes are involved in generating stable, barrier-like structures such as skin, hair, and blood clots. To date, eight isoforms of transglutaminases have been identified in humans [264, 265]. The requirement for Ca^{2+} ions binding for mammalian transglutaminase reactions has been proved in *in vitro* assays and *in situ* on tissue slices [266]. Unlike these tissue transglutaminases, microbial transglutaminase (mTG) is Ca^{2+} independent, making it amenable to various gel-formation conditions [267, 268]. Moreover, mTG maintains its high-level activity over a broad range of temperatures (37˚C-50˚C) and pH values (~90% between 5 and 8), which makes it compliant with a wide variety of biomaterial fabrication techniques [262]. Gelatin can be crosslinked by mTG and form a stable hydrogel within minutes at body temperature

[262]. Finally, the resulting double network contains many hydrogen bonds and other intermolecular interactions that could dissociate during deformation to dissipate energy [269].

The mechanical characteristics of the PDNs were also evaluated. It was found that the PDN had controlled and fast gelation to avoid mixing with body fluids. The relative timing of phase separation and gelatin crosslinking is a determining factor in the formation of strong and interconnected pores with varying shapes and sizes. The viscoelastic properties of the developed PDNs were also comparable to that of the native soft tissues. The porous structure of the PDN was evaluated using two different imaging methods, and all of them confirmed the existence of cell-sized pores, leading to high viability values for the PDNs. It was demonstrated that the larger pores improved cell adhesion and proliferation.

Immediately after insertion, a biomaterial is subjected to the body's immune response, governed by the activity of tissue-resident macrophages and the monocytes entering the bloodstream at the implantation site. A rapidly induced and temporal inflammation phase is necessary for healing. The precise timing of M1 to M2 transition is crucial to avoid excessive inflammatory response and consequently is among the principal considerations in the design and fabrication of novel biomaterials. In addition to biochemical cues such as cytokines or substrate composition that direct macrophage polarization, macrophages are prone to differentiate spontaneously in response to mechanical signals such as stiffness, 2D topography, or 3D microstructure of the biomaterials [246]. Hence, in the present study, we evaluated the effect of different pore sizes on the cytokine-free differentiation of monocyte-derived macrophages. The results show that porous double-network scaffolds with an average pore size of ~65 μm are advantageous for promoting both the elongation and differentiation towards the pro-healing M2 type of human macrophages. Our findings also proved the influence of the anti-inflammatory effect of the chitosan network on M2 macrophage polarization. Furthermore, their unique composition and rapid gelation allowed the structured hydrogels to achieve strong tissue adhesion and promoted rapid hemostasis following tissue injury.

It is anticipated that the reported design principle and the material system could facilitate the clinical translation of these injectable immunomodulatory hydrogels as space-filling biomaterials to promote wound healing.

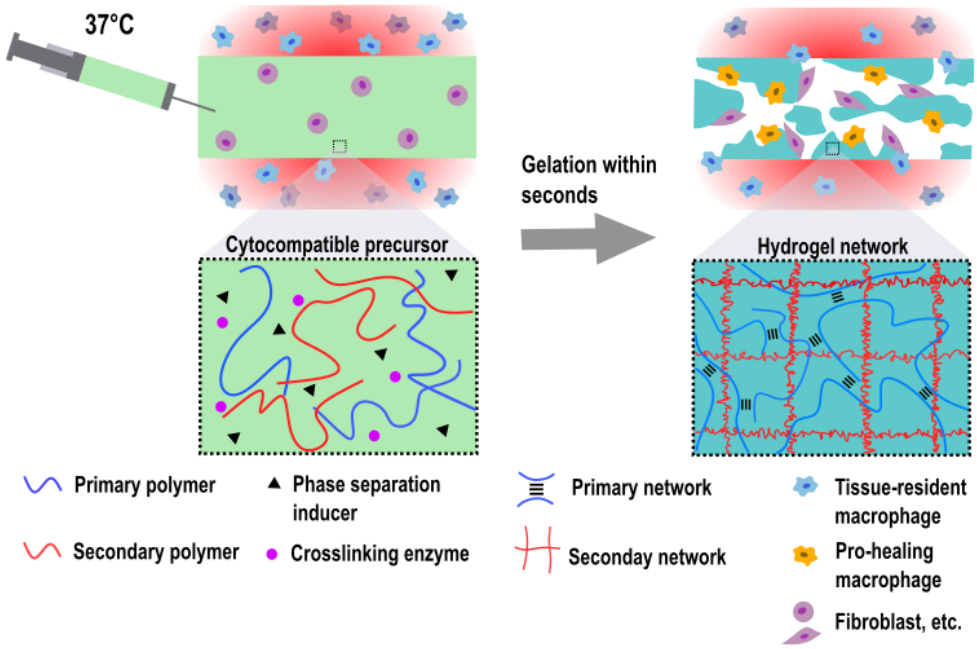

Figure 4-12 Design of porous double network hydrogels (PDNs).

Chapter 5 Conclusions and perspectives

This chapter is focused on summarizing the main conclusions of the thesis regarding the design and biofabrication of immunomodulatory multiphase hydrogels for regenerative therapy. The outcome of using HNMs as a cytokine-releasing substrate is discussed, and the immune regulating function of the PDNs is elaborated. The last part of this chapter outlines the future potential research avenues in the field of study. The sentences in quotations are verbatim of the author's publications (reference [1]).

5.1 Conclusions

5.1.1 Hybrid nanocomposite microgels

"In this work, we developed a novel IL-10 -loaded nanocomposite microgel system as an improved drug delivery platform to combat fibrosis. Synthesized with a facile water-oil emulsion approach, the resulting microgels can have well-defined shapes, dispersity, and tissue-mimetic mechanics. The incorporation of Laponite into the polymeric microgels enabled a tunable degradation rate and sustained drug delivery. The Laponite-loaded microgels were auspicious in attracting macrophages as well as promoting fibroblasts spreading, motility, and proliferation. The sustained, bioactive release of IL-10 regulated co-cultured macrophage activation while counteracting TGF-β1-driven collagen production by fibroblasts grown on the scaffold, thereby inhibiting the fibrosis formation. Combined with the microgel injectability, these results present these multifunctional hydrogel beads as a promising cell-instructive system in wound healing applications."

5.1.2 Porous double network gels

The present study has developed a new class of multi-functional injectable hydrogels for wound healing applications. Porous double network hydrogels were fabricated from two natural biopolymers, chitosan and gelatin. The synergistic gelation of the two biopolymers enabled modulation of various properties of the hydrogels, including rheological properties, swellability

and porosity. The *in-situ* forming of porous structures was beneficial for cell adhesion and proliferation. The combined effect of the microporous network and hydrogel composition induced macrophage elongation and differentiation toward the pro-healing M2 phenotype. The hydrogels elicited tissue-adhesiveness and hemostatic efficacy comparable to existing bioadhesives and hemostatic agents. Taken together, the proposed material and technology have the potential to govern future biomaterial designs for enhanced tissue regeneration and wound healing.

5.2 Prospectives and future directions

5.2.1 Microfluidics

Hydrogel beads with diameters ranging from 45 nm to 1680 µm have found many useful drug delivery and cell therapy applications. In the batch emulsion technique, the hydrogel precursor solution is emulsified in a continuous oil phase to create droplets, becoming gel to form hydrogel microspheres. However, the batch emulsion technology limits the complexity of the structure of the obtained microgels. Moreover, the obtained microgels are polydisperse, and there are large differences between batches. Separating the formed microgels based on their size would also result in a low yield. The current gold standard for fabricating microspheres is the oil-based microfluidic techniques. In this method, the pre-hydrogel solution, e.g., sodium alginate, flows in an oil phase, and the microgels form by adjusting the flow rates of the pre-hydrogel solution and the oil phase. Microfluidic-based methods provide better control over microparticles' size, composition, and structure than alternative fabrication methods, such as batch emulsions, electrohydrodynamic spraying, and lithography techniques [270]. One possible direction that can be followed in future studies would be to design and manufacture microfluidic chips for the production of a series of drug-loaded nanocomposite microgels with adjustable size and shape.

5.2.2 Microporous annealed particle

The granular gels suffer inherently from their dynamic nature, limiting their application in load-bearing applications. Recent studies have demonstrated the efficacy of a class of injectable particle hydrogels—termed “microporous annealed particle” in creating a stable, interconnected

structure that necessitates degradation to change the organization of the particle network [134, 271, 272]. One possible improvement to the current drug releasing system is to move toward the fabrication of HNMs with surface functional groups that can form an inter-particle network after injection. By utilizing non-toxic crosslinking methods, such as enzymatic, biorthogonal chemical, or visible light crosslinking applied in vivo, HNMs could form an integrated scaffold with strengthened structure and prolonged structure biodegradation time. Annealed HNM would have the advantages of injectability, microporosity with tunable pore size, and mechanical stability.

5.2.3 Cytokine release studies

The body's immune response to biomaterials is proceeded through the interactions between various immune cells (i.e., macrophages, neutrophils, and lymphocytes) and repairing cells (i.e., fibroblasts, endothelial cells, and keratinocytes). These cells interact with each other through the production of protein signalling, namely cytokines or growth factors with the ability to instruct target cells. These protein molecules can influence cellular functions, including differentiation, proliferation, activation, apoptosis and even induction of cytokine release [273]. Thus, further examination of the released cytokines and growth factors is crucial to evaluate the anti-inflammatory function of the encapsulated macrophages *in vitro* to ensure the implementation of the PDNs in biological environments.

5.2.4 Animal studies

Many parameters are associated with body immune response that can not be recapitulated by the in vitro experiments. Firstly, macrophage monoculture models do not consider the function of other immune cells, such as neutrophils, mast cells, and dendritic cells, and their cell-to-cell interactions. Secondly, the ECM and serum molecules are not present in vitro studies, which could significantly affect how the biomaterials are identified and presented to the immune system [274]. Therefore, animal studies are needed for translating injectable hydrogels to clinical use.

Bibliography

1. Mohammadi, S., et al., *Immunomodulatory Microgels Support Proregenerative Macrophage Activation and Attenuate Fibroblast Collagen Synthesis.* Advanced Healthcare Materials, 2022: p. 2102366.
2. Gurtner, G.C., et al., *Wound repair and regeneration.* Nature, 2008. **453**(7193): p. 314-321.
3. Kutty, J.K. and K. Webb, *Tissue engineering therapies for the vocal fold lamina propria.* Tissue Engineering Part B: Reviews, 2009. **15**(3): p. 249-262.
4. Khatib, L., D.L. Cass, and N.S. Adzick, *Updates in fetal wound healing and scar prevention*, in *Pediatric oculoplastic surgery*. 2018, Springer. p. 45-58.
5. Julier, Z., et al., *Promoting tissue regeneration by modulating the immune system.* Acta biomaterialia, 2017. **53**: p. 13-28.
6. Erickson, J.R. and K. Echeverri, *Learning from regeneration research organisms: The circuitous road to scar free wound healing.* Developmental biology, 2017.
7. Sridharan, R., et al., *Biomaterial based modulation of macrophage polarization: a review and suggested design principles.* Materials Today, 2015. **18**(6): p. 313-325.
8. Sun, G., Y.I. Shen, and J.W. Harmon, *Engineering Pro‐Regenerative Hydrogels for Scarless Wound Healing.* Advanced Healthcare Materials, 2018. **7**(14): p. 1800016.
9. Cuchiara, M.P., et al., *Multilayer microfluidic PEGDA hydrogels.* Biomaterials, 2010. **31**(21): p. 5491-5497.
10. Wang, Y., et al., *Foreign body reaction to implantable biosensors: effects of tissue trauma and implant size.* Journal of diabetes science and technology, 2015. **9**(5): p. 966-977.
11. Carnicer-Lombarte, A., et al., *Foreign body reaction to implanted biomaterials and its impact in nerve neuroprosthetics.* Frontiers in Bioengineering and Biotechnology, 2021: p. 271.
12. Piantanida, E., et al., *Design of nanocomposite injectable hydrogels for minimally invasive surgery.* Accounts of chemical research, 2019. **52**(8): p. 2101-2112.
13. Chao, Y., Q. Chen, and Z. Liu, *Smart injectable hydrogels for cancer immunotherapy.* Advanced Functional Materials, 2020. **30**(2): p. 1902785.
14. Koshy, S.T., et al., *Injectable nanocomposite cryogels for versatile protein drug delivery.* Acta biomaterialia, 2018. **65**: p. 36-43.
15. Zhou, H., et al., *Injectable biomaterials for translational medicine.* Materials Today, 2019. **28**: p. 81-97.
16. Zhao, Y., et al., *An injectable strong hydrogel for bone reconstruction.* Advanced Healthcare Materials, 2019. **8**(17): p. 1900709.
17. Ridiandries, A., J. Tan, and C.A. Bursill, *The role of chemokines in wound healing.* International journal of molecular sciences, 2018. **19**(10): p. 3217.
18. Viidik, A. and F. Gottrup, *Mechanics of healing soft tissue wounds*, in *Frontiers in biomechanics*. 1986, Springer. p. 263-279.
19. Guo, S.a. and L.A. DiPietro, *Factors affecting wound healing.* Journal of dental research, 2010. **89**(3): p. 219-229.
20. Ellis, S., E.J. Lin, and D. Tartar, *Immunology of wound healing.* Current dermatology reports, 2018. **7**(4): p. 350-358.
21. Mercandetti, M. and A. Cohen, *Wound healing and repair.* E Medicine (cited 2002 Oct 7). Available from URL: http://www. eMedicine. com. Inc, 2017.

22. Reinke, J. and H. Sorg, *Wound repair and regeneration.* European surgical research, 2012. **49**(1): p. 35-43.
23. Sonnemann, K.J. and W.M. Bement, *Wound repair: toward understanding and integration of single-cell and multicellular wound responses.* Annual review of cell and developmental biology, 2011. **27**: p. 237-263.
24. Dekoninck, S. and C. Blanpain, *Stem cell dynamics, migration and plasticity during wound healing.* Nature cell biology, 2019. **21**(1): p. 18-24.
25. Pugliese, E., et al., *Wound healing and scar wars.* Advanced drug delivery reviews, 2018.
26. Kawasumi, A., et al., *Wound healing in mammals and amphibians: toward limb regeneration in mammals.* New Perspectives in Regeneration, 2012: p. 33-49.
27. Keane, T.J., C.-M. Horejs, and M.M. Stevens, *Scarring vs. functional healing: Matrix-based strategies to regulate tissue repair.* Advanced drug delivery reviews, 2018. **129**: p. 407-419.
28. Gottrup, F., *Healing of incisional wounds in stomach and duodenum: a biomechanical study.* The American Journal of Surgery, 1980. **140**(2): p. 296-301.
29. Nilsson, T., *Closure of the abdominal wound with single-layer and double-layer technique. Animal studies.* Acta Chirurgica Scandinavica, 1981. **147**(6): p. 399-403.
30. Ghosh, B., et al., *Optical Coherence Tomography Reveals Mechanobiologically Stable Self-Organizing Di-Fork Architecture of Mice Cutaneous Scars i, ii.* bioRxiv, 2017: p. 181545.
31. Fan, Y., et al., *Quantitative and Qualitative Evaluation of Supercontinuum Laser-Induced Cutaneous Thermal Injuries and Their Repair With OCT Images.* Lasers in Surgery and Medicine, 2020.
32. Ghosh, B., et al., *Structural mechanics modeling reveals stress-adaptive features of cutaneous scars.* Biomechanics and Modeling in Mechanobiology, 2020: p. 1-7.
33. Hadjipanayi, E., V. Mudera, and R. Brown, *Close dependence of fibroblast proliferation on collagen scaffold matrix stiffness.* Journal of tissue engineering and regenerative medicine, 2009. **3**(2): p. 77-84.
34. Wynn, T.A., *Integrating mechanisms of pulmonary fibrosis.* Journal of Experimental Medicine, 2011. **208**(7): p. 1339-1350.
35. Larson, D.E., *Mayo Clinic family health book*. 1990: W. Morrow.
36. Thannickal, V.J., et al., *Mechanisms of pulmonary fibrosis.* Annu. Rev. Med., 2004. **55**: p. 395-417.
37. Dolhnikoff, M., T. Mauad, and M.S. Ludwig, *Extracellular matrix and oscillatory mechanics of rat lung parenchyma in bleomycin-induced fibrosis.* American journal of respiratory and critical care medicine, 1999. **160**(5): p. 1750-1757.
38. Ebihara, T., et al., *Changes in extracellular matrix and tissue viscoelasticity in bleomycin–induced lung fibrosis: Temporal aspects.* American journal of respiratory and critical care medicine, 2000. **162**(4): p. 1569-1576.
39. Cavalcante, F.S., et al., *Mechanical interactions between collagen and proteoglycans: implications for the stability of lung tissue.* Journal of applied physiology, 2005. **98**(2): p. 672-679.
40. Bates, J.H., et al., *Linking parenchymal disease progression to changes in lung mechanical function by percolation.* American journal of respiratory and critical care medicine, 2007. **176**(6): p. 617-623.

41. Friedrich, G., et al., *Vocal fold scars: current concepts and future directions. Consensus report of the Phonosurgery Committee of the European Laryngological Society.* European Archives of Oto-Rhino-Laryngology, 2013. **270**(9): p. 2491-2507.
42. Thibeault, S.L., et al., *Hyaluronan levels in acute vocal fold scar.* The Laryngoscope, 2004. **114**(4): p. 760-764.
43. Tateya, T., et al., *Histologic characterization of rat vocal fold scarring.* Annals of Otology, Rhinology & Laryngology, 2005. **114**(3): p. 183-191.
44. Rousseau, B., et al., *Characterization of chronic vocal fold scarring in a rabbit model.* Journal of Voice, 2004. **18**(1): p. 116-124.
45. Rousseau, B., et al., *Characterization of vocal fold scarring in a canine model.* The Laryngoscope, 2003. **113**(4): p. 620-627.
46. Moore, J. and S. Thibeault, *Insights into the role of elastin in vocal fold health and disease.* Journal of Voice, 2012. **26**(3): p. 269-275.
47. Svistushkin, M.V., et al., *Collagen fibrillar structures in vocal fold scarring and repair using stem cell therapy: a detailed histological, immunohistochemical and atomic force microscopy study.* Journal of microscopy, 2019. **274**(1): p. 55-68.
48. Asgari, M., et al., *In vitro fibrillogenesis of tropocollagen type III in collagen type I affects its relative fibrillar topology and mechanics.* Scientific reports, 2017. **7**(1): p. 1-10.
49. Thibeault, S.L., et al., *Histologic and rheologic characterization of vocal fold scarring.* Journal of Voice, 2002. **16**(1): p. 96-104.
50. Kim, S.Y. and M.G. Nair, *Macrophages in wound healing: activation and plasticity.* Immunology and cell biology, 2019. **97**(3): p. 258-267.
51. Wynn, T.A., A. Chawla, and J.W. Pollard, *Macrophage biology in development, homeostasis and disease.* Nature, 2013. **496**(7446): p. 445-455.
52. Godwin, J.W., A.R. Pinto, and N.A. Rosenthal, *Macrophages are required for adult salamander limb regeneration.* Proceedings of the National Academy of Sciences, 2013. **110**(23): p. 9415-9420.
53. Wynn, T.A. and L. Barron. *Macrophages: master regulators of inflammation and fibrosis*. in *Seminars in liver disease*. 2010. © Thieme Medical Publishers.
54. Scatena, M., et al., *Macrophages: The bad, the ugly, and the good in the inflammatory response to biomaterials*, in *The immune response to implanted materials and devices*. 2017, Springer. p. 37-62.
55. Krzyszczyk, P., et al., *The Role of Macrophages in Acute and Chronic Wound Healing and Interventions to Promote Pro-wound Healing Phenotypes.* Frontiers in physiology, 2018. **9**.
56. Das, A., et al., *Monocyte and macrophage plasticity in tissue repair and regeneration.* The American journal of pathology, 2015. **185**(10): p. 2596-2606.
57. Gensel, J.C. and B. Zhang, *Macrophage activation and its role in repair and pathology after spinal cord injury.* Brain research, 2015. **1619**: p. 1-11.
58. Novak, M.L. and T.J. Koh, *Macrophage phenotypes during tissue repair.* Journal of leukocyte biology, 2013. **93**(6): p. 875-881.
59. Spiller, K.L., et al., *The role of macrophage phenotype in vascularization of tissue engineering scaffolds.* Biomaterials, 2014. **35**(15): p. 4477-4488.
60. Spiller, K.L., et al., *Sequential delivery of immunomodulatory cytokines to facilitate the M1-to-M2 transition of macrophages and enhance vascularization of bone scaffolds.* Biomaterials, 2015. **37**: p. 194-207.

61. Hong, L.T.A., et al., *An injectable hydrogel enhances tissue repair after spinal cord injury by promoting extracellular matrix remodeling.* Nature communications, 2017. **8**(1): p. 1-14.
62. Sindrilaru, A. and K. Scharffetter-Kochanek, *Disclosure of the culprits: macrophages—versatile regulators of wound healing.* Advances in wound care, 2013. **2**(7): p. 357-368.
63. Sapudom, J., et al., *Fibroblast fate regulation by time dependent TGF-β1 and IL-10 stimulation in biomimetic 3D matrices.* Biomaterials science, 2017. **5**(9): p. 1858-1867.
64. Martin, K.E. and A.J. García, *Macrophage phenotypes in tissue repair and the foreign body response: implications for biomaterial-based regenerative medicine strategies.* Acta Biomaterialia, 2021.
65. King, A., et al., *Regenerative wound healing: the role of interleukin-10.* Advances in wound care, 2014. **3**(4): p. 315-323.
66. Ullm, F., et al., *3D scaffold-based macrophage fibroblast coculture model reveals IL-10 dependence of wound resolution phase.* Advanced biosystems, 2020. **4**(1): p. 1900220.
67. Sok, M.C.P., et al., *Dual delivery of IL-10 and AT-RvD1 from PEG hydrogels polarize immune cells towards pro-regenerative phenotypes.* Biomaterials, 2021. **268**: p. 120475.
68. Saxena, A., et al., *Interleukin-10 paradox: A potent immunoregulatory cytokine that has been difficult to harness for immunotherapy.* Cytokine, 2015. **74**(1): p. 27-34.
69. Minshawi, F., et al., *The generation of an engineered interleukin-10 protein with improved stability and biological function.* Frontiers in immunology, 2020. **11**: p. 1794.
70. Shen, H., et al., *A DAMP-scavenging, IL-10-releasing hydrogel promotes neural regeneration and motor function recovery after spinal cord injury.* Biomaterials, 2022. **280**: p. 121279.
71. Rodell, C.B., et al., *Local immunotherapy via delivery of interleukin-10 and transforming growth factor β antagonist for treatment of chronic kidney disease.* Journal of Controlled Release, 2015. **206**: p. 131-139.
72. Chen, M.H., et al., *Injectable supramolecular hydrogel/microgel composites for therapeutic delivery.* Macromolecular bioscience, 2019. **19**(1): p. 1800248.
73. Shamskhou, E.A., et al., *Hydrogel-based delivery of Il-10 improves treatment of bleomycin-induced lung fibrosis in mice.* Biomaterials, 2019. **203**: p. 52-62.
74. Kang, J.I. and K.M. Park, *Advances in gelatin-based hydrogels for wound management.* Journal of Materials Chemistry B, 2021. **9**(6): p. 1503-1520.
75. Chandorkar, Y. and B. Basu, *The foreign body response demystified.* ACS Biomaterials Science & Engineering, 2018. **5**(1): p. 19-44.
76. Zhang, D., et al., *Dealing with the foreign-body response to implanted biomaterials: strategies and applications of new materials.* Advanced Functional Materials, 2021. **31**(6): p. 2007226.
77. Kou, P.M. and J.E. Babensee, *Macrophage and dendritic cell phenotypic diversity in the context of biomaterials.* Journal of biomedical materials research Part A, 2011. **96**(1): p. 239-260.
78. Anderson, J.M., A. Rodriguez, and D.T. Chang. *Foreign body reaction to biomaterials*. in *Seminars in immunology*. 2008. Elsevier.
79. Camarero-Espinosa, S., et al., *3D Printed Dual-Porosity Scaffolds: The Combined Effect of Stiffness and Porosity in the Modulation of Macrophage Polarization.* Advanced Healthcare Materials, 2022. **11**(1): p. 2101415.

80. Mariani, E., et al., *Biomaterials: foreign bodies or tuners for the immune response?* International journal of molecular sciences, 2019. **20**(3): p. 636.
81. Davenport Huyer, L., et al., *Advanced strategies for modulation of the material–macrophage interface.* Advanced Functional Materials, 2020. **30**(44): p. 1909331.
82. Sadtler, K., et al., *Divergent immune responses to synthetic and biological scaffolds.* Biomaterials, 2019. **192**: p. 405-415.
83. Beningo, K.A. and Y.-l. Wang, *Fc-receptor-mediated phagocytosis is regulated by mechanical properties of the target.* Journal of cell science, 2002. **115**(4): p. 849-856.
84. Blakney, A.K., M.D. Swartzlander, and S.J. Bryant, *Student award winner in the undergraduate category for the society of biomaterials 9th World Biomaterials Congress, Chengdu, China, June 1–5, 2012: The effects of substrate stiffness on the in vitro activation of macrophages and in vivo host response to poly (ethylene glycol)‐based hydrogels.* Journal of Biomedical Materials Research Part A, 2012. **100**(6): p. 1375-1386.
85. Okamoto, T., et al., *Reduced substrate stiffness promotes M2-like macrophage activation and enhances peroxisome proliferator-activated receptor γ expression.* Experimental cell research, 2018. **367**(2): p. 264-273.
86. Friedemann, M., et al., *Instructing human macrophage polarization by stiffness and glycosaminoglycan functionalization in 3D collagen networks.* Advanced healthcare materials, 2017. **6**(7): p. 1600967.
87. McWhorter, F.Y., et al., *Modulation of macrophage phenotype by cell shape.* Proceedings of the National Academy of Sciences, 2013. **110**(43): p. 17253-17258.
88. Luu, T.U., et al., *Micro-and nanopatterned topographical cues for regulating macrophage cell shape and phenotype.* ACS applied materials & interfaces, 2015. **7**(51): p. 28665-28672.
89. Wojciak-Stothard, B., et al., *Guidance and activation of murine macrophages by nanometric scale topography.* Experimental cell research, 1996. **223**(2): p. 426-435.
90. Chen, S., et al., *Characterization of topographical effects on macrophage behavior in a foreign body response model.* Biomaterials, 2010. **31**(13): p. 3479-3491.
91. Vaine, C.A., et al., *Tuning innate immune activation by surface texturing of polymer microparticles: the role of shape in inflammasome activation.* The Journal of Immunology, 2013. **190**(7): p. 3525-3532.
92. Paul, N.E., et al., *Topographical control of human macrophages by a regularly microstructured polyvinylidene fluoride surface.* Biomaterials, 2008. **29**(30): p. 4056-4064.
93. Ainslie, K.M., et al., *In vitro immunogenicity of silicon-based micro-and nanostructured surfaces.* ACS nano, 2008. **2**(5): p. 1076-1084.
94. Kianoush, F., et al., *R egulation of RAW264. 7 macrophage polarization on smooth and rough surface topographies by galectin‐3.* Journal of Biomedical Materials Research Part A, 2017. **105**(9): p. 2499-2509.
95. Walkey, C.D., et al., *Nanoparticle size and surface chemistry determine serum protein adsorption and macrophage uptake.* Journal of the American Chemical Society, 2012. **134**(4): p. 2139-2147.
96. Zandstra, J., et al., *Microsphere size influences the foreign body reaction.* Eur Cell Mater, 2014. **28**(28): p. 335-347.
97. Kusaka, T., et al., *Effect of silica particle size on macrophage inflammatory responses.* PloS one, 2014. **9**(3): p. e92634.

98. Padmore, T., et al., *Quantitative analysis of the role of fiber length on phagocytosis and inflammatory response by alveolar macrophages.* Biochimica et Biophysica Acta (BBA)-General Subjects, 2017. **1861**(2): p. 58-67.
99. Sanders, J., C. Stiles, and C. Hayes, *Tissue response to single-polymer fibers of varying diameters: Evaluation of fibrous encapsulation and macrophage density.* Journal of biomedical materials research, 2000. **52**(1): p. 231-237.
100. Sanders, J., S. Bale, and T. Neumann, *Tissue response to microfibers of different polymers: polyester, polyethylene, polylactic acid, and polyurethane.* Journal of Biomedical Materials Research: An Official Journal of The Society for Biomaterials, The Japanese Society for Biomaterials, and The Australian Society for Biomaterials and the Korean Society for Biomaterials, 2002. **62**(2): p. 222-227.
101. Champion, J.A. and S. Mitragotri, *Shape induced inhibition of phagocytosis of polymer particles.* Pharmaceutical research, 2009. **26**(1): p. 244-249.
102. Veiseh, O., et al., *Size-and shape-dependent foreign body immune response to materials implanted in rodents and non-human primates.* Nature materials, 2015. **14**(6): p. 643-651.
103. Matlaga, B.F., L.P. Yasenchak, and T.N. Salthouse, *Tissue response to implanted polymers: the significance of sample shape.* Journal of biomedical materials research, 1976. **10**(3): p. 391-397.
104. Bota, P.C., et al., *Biomaterial topography alters healing in vivo and monocyte/macrophage activation in vitro.* Journal of Biomedical Materials Research Part A, 2010. **95**(2): p. 649-657.
105. Sussman, E.M., et al., *Porous implants modulate healing and induce shifts in local macrophage polarization in the foreign body reaction.* Annals of biomedical engineering, 2014. **42**(7): p. 1508-1516.
106. Madden, L.R., et al., *Proangiogenic scaffolds as functional templates for cardiac tissue engineering.* Proceedings of the National Academy of Sciences, 2010. **107**(34): p. 15211-15216.
107. Chen, M., et al., *Substrate stiffness modulates bone marrow-derived macrophage polarization through NF-κB signaling pathway.* Bioactive materials, 2020. **5**(4): p. 880-890.
108. Garg, K., et al., *Macrophage functional polarization (M1/M2) in response to varying fiber and pore dimensions of electrospun scaffolds.* Biomaterials, 2013. **34**(18): p. 4439-4451.
109. Yin, Y., et al., *Pore size-mediated macrophage M1-to-M2 transition influences new vessel formation within the compartment of a scaffold.* Applied Materials Today, 2020. **18**: p. 100466.
110. Jiang, S., et al., *Cryoprotectant enables structural control of porous scaffolds for exploration of cellular mechano-responsiveness in 3D.* Nature communications, 2019. **10**(1): p. 1-14.
111. Nichol, J.W., et al., *Cell-laden microengineered gelatin methacrylate hydrogels.* Biomaterials, 2010. **31**(21): p. 5536-5544.
112. Seidlits, S.K., et al., *The effects of hyaluronic acid hydrogels with tunable mechanical properties on neural progenitor cell differentiation.* Biomaterials, 2010. **31**(14): p. 3930-3940.
113. Irmak, G.l., T.r.T. Demirtaş, and M.e. Gümüşderelioğlu, *Highly methacrylated gelatin bioink for bone tissue engineering.* ACS Biomaterials Science & Engineering, 2018. **5**(2): p. 831-845.

114. Yousefi, F., S. Kandel, and N. Pleshko, *Infrared spectroscopic quantification of methacrylation of hyaluronic acid: a scaffold for tissue engineering applications.* Applied spectroscopy, 2018. **72**(10): p. 1455-1466.
115. Zdilla, M.J., et al., *Circularity, solidity, axes of a best fit ellipse, aspect ratio, and roundness of the foramen ovale: a morphometric analysis with neurosurgical considerations.* The Journal of craniofacial surgery, 2016. **27**(1): p. 222.
116. Yang, Z., et al., *Covalent grafting of hyperbranched poly-L-lysine on Ti-based implants achieves dual functions of antibacteria and promoted osteointegration in vivo.* Biomaterials, 2021. **269**: p. 120534.
117. Bao, G., et al., *Triggered micropore-forming bioprinting of porous viscoelastic hydrogels.* Materials horizons, 2020. **7**(9): p. 2336-2347.
118. Abozeid, S.M., R.M. Hathout, and K. Abou-Aisha, *Silencing of the metastasis-linked gene, AEG-1, using siRNA-loaded cholamine surface-modified gelatin nanoparticles in the breast carcinoma cell line MCF-7.* Colloids and Surfaces B: Biointerfaces, 2016. **145**: p. 607-616.
119. Hathout, R.M. and A.A. Metwally, *Gelatin nanoparticles*, in *Pharmaceutical Nanotechnology*. 2019, Springer. p. 71-78.
120. Ravanbakhsh, H., G. Bao, and L. Mongeau, *Carbon nanotubes promote cell migration in hydrogels.* Scientific reports, 2020. **10**(1): p. 1-10.
121. Eke, G., et al., *Development of a UV crosslinked biodegradable hydrogel containing adipose derived stem cells to promote vascularization for skin wounds and tissue engineering.* Biomaterials, 2017. **129**: p. 188-198.
122. Vigata, M., et al., *Gelatin methacryloyl hydrogels control the localized delivery of albumin-bound paclitaxel.* Polymers, 2020. **12**(2): p. 501.
123. Duconseille, A., et al., *Gelatin structure and composition linked to hard capsule dissolution: A review.* Food hydrocolloids, 2015. **43**: p. 360-376.
124. Chen, Y.C., et al., *Functional human vascular network generated in photocrosslinkable gelatin methacrylate hydrogels.* Advanced functional materials, 2012. **22**(10): p. 2027-2039.
125. Schuurmans, C.C., et al., *Hyaluronic acid and chondroitin sulfate (meth) acrylate-based hydrogels for tissue engineering: Synthesis, characteristics and pre-clinical evaluation.* Biomaterials, 2021. **268**: p. 120602.
126. Niloy, K.K., et al., *Methacrylated hyaluronic acid–based hydrogels maintain Stemness in human dental pulp stem cells.* Regenerative Engineering and Translational Medicine, 2019: p. 1-11.
127. Bencherif, S.A., et al., *Influence of the degree of methacrylation on hyaluronic acid hydrogels properties.* Biomaterials, 2008. **29**(12): p. 1739-1749.
128. Chandrasekharan, A., et al., *In situ photocrosslinkable hyaluronic acid‐based surgical glue with tunable mechanical properties and high adhesive strength.* Journal of polymer Science part A: polymer Chemistry, 2019. **57**(4): p. 522-530.
129. Taheri, S., et al., *Injectable, Pore‐Forming, Perfusable Double‐Network Hydrogels Resilient to Extreme Biomechanical Stimulations.* Advanced Science, 2021: p. 2102627.
130. Mohammadi, S., et al., *Graphene oxide-enriched poly (ε-caprolactone) electrospun nanocomposite scaffold for bone tissue engineering applications.* Journal of Bioactive and Compatible Polymers, 2017. **32**(3): p. 325-342.

131. Ravanbakhsh, H., et al., *Composite inks for extrusion printing of biological and biomedical constructs.* ACS Biomaterials Science & Engineering, 2020.
132. Shafiei, S.S., S. Mohammadi, and F. Moztarzadeh, *Poly (ε-caprolactone)/layered double hydroxide microspheres-aggregated nanocomposite scaffold for osteogenic differentiation of mesenchymal stem cell.* Materials Today Communications, 2020. **23**: p. 100913.
133. Boekema, B.K., et al., *Effect of pore size and cross-linking of a novel collagen-elastin dermal substitute on wound healing.* Journal of Materials Science: Materials in Medicine, 2014. **25**(2): p. 423-433.
134. Riley, L., L. Schirmer, and T. Segura, *Granular hydrogels: emergent properties of jammed hydrogel microparticles and their applications in tissue repair and regeneration.* Current opinion in biotechnology, 2019. **60**: p. 1-8.
135. Qazi, T.H. and J.A. Burdick, *Granular hydrogels for endogenous tissue repair.* Biomaterials and Biosystems, 2021. **1**: p. 100008.
136. Truong, N.F., et al., *Microporous annealed particle hydrogel stiffness, void space size, and adhesion properties impact cell proliferation, cell spreading, and gene transfer.* Acta biomaterialia, 2019. **94**: p. 160-172.
137. Caldwell, A.S., et al., *Clickable microgel scaffolds as platforms for 3D cell encapsulation.* Advanced healthcare materials, 2017. **6**(15): p. 1700254.
138. Yamada, K., H. Emori, and K. Nakazawa, *Time-evolution of bubble formation in a viscous liquid.* Earth, planets and space, 2008. **60**(6): p. 661-679.
139. Sanghvi, S.P. and J.G. Nairn, *Effect of viscosity and interfacial tension on particle size of cellulose acetate trimellitate microspheres.* Journal of microencapsulation, 1991. **9**(2): p. 215-227.
140. Hejmady, P., et al., *A processing route to spherical polymer particles via controlled droplet retraction.* Powder Technology, 2021. **388**: p. 401-411.
141. Pálková, H., et al., *Laponite-derived porous clay heterostructures: I. Synthesis and physicochemical characterization.* Microporous and Mesoporous Materials, 2010. **127**(3): p. 228-236.
142. Zhang, S., et al., *Fabrication of Microspheres from High-Viscosity Bioink Using a Novel Microfluidic-Based 3D Bioprinting Nozzle.* Micromachines, 2020. **11**(7): p. 681.
143. Attaluri, A., et al., *Nanoparticle distribution and temperature elevations in prostatic tumours in mice during magnetic nanoparticle hyperthermia.* International Journal of Hyperthermia, 2011. **27**(5): p. 491-502.
144. Heimel, P., et al., *Iodine-enhanced micro-CT imaging of soft tissue on the example of peripheral nerve regeneration.* Contrast media & molecular imaging, 2019. **2019**.
145. Ondruš, J., et al., *A novel approach to imaging engorged ticks: Micro-CT scanning of Ixodes ricinus fed on blood enriched with gold nanoparticles.* Ticks and Tick-borne Diseases, 2021. **12**(1): p. 101559.
146. Attaluri, A., R. Ma, and L. Zhu, *Using microCT imaging technique to quantify heat generation distribution induced by magnetic nanoparticles for cancer treatments.* Journal of heat transfer, 2011. **133**(1).
147. Ashton, J.R., J.L. West, and C.T. Badea, *In vivo small animal micro-CT using nanoparticle contrast agents.* Frontiers in pharmacology, 2015. **6**: p. 256.
148. Moisenovich, M., et al. *Novel 3D-microcarriers from recombinant spidroin for regenerative medicine.* in *Doklady Biochemistry and Biophysics*. 2015. Springer.

149. Highley, C.B., et al., *Jammed microgel inks for 3D printing applications.* Advanced Science, 2019. **6**(1): p. 1801076.
150. Menut, P., et al., *Does size matter? Elasticity of compressed suspensions of colloidal-and granular-scale microgels.* Soft Matter, 2012. **8**(1): p. 156-164.
151. Town, A.R., et al., *Dual-stimuli responsive injectable microgel/solid drug nanoparticle nanocomposites for release of poorly soluble drugs*. Nanoscale, 2017. **9**(19): p. 6302-6314.
152. Ye, F., et al., *Real-time UV imaging of piroxicam diffusion and distribution from oil solutions into gels mimicking the subcutaneous matrix*. European journal of pharmaceutical sciences, 2012. **46**(1-2): p. 72-78.
153. Gao, Q., et al., *Needle-free injection: Dental infiltration anesthesia.* International Journal of Pharmaceutics, 2021. **604**: p. 120765.
154. Chaudhuri, O., et al., *Effects of extracellular matrix viscoelasticity on cellular behaviour.* Nature, 2020. **584**(7822): p. 535-546.
155. Lee, J.H., et al., *Highly tough, biocompatible, and magneto-responsive Fe 3 O 4/Laponite/PDMAAm nanocomposite hydrogels.* Scientific reports, 2019. **9**(1): p. 1-13.
156. Mohammadi, S., et al., *Graphene oxide–enriched double network hydrogel with tunable physico-mechanical properties and performance.* Reactive and Functional Polymers, 2016. **106**: p. 120-131.
157. Shin, H., B.D. Olsen, and A. Khademhosseini, *The mechanical properties and cytotoxicity of cell-laden double-network hydrogels based on photocrosslinkable gelatin and gellan gum biomacromolecules.* Biomaterials, 2012. **33**(11): p. 3143-3152.
158. Borzacchiello, A., et al., *Effect of hyaluronic acid amide derivative on equine synovial fluid viscoelasticity.* Journal of Biomedical Materials Research Part A: An Official Journal of The Society for Biomaterials, The Japanese Society for Biomaterials, and The Australian Society for Biomaterials and the Korean Society for Biomaterials, 2010. **92**(3): p. 1162-1170.
159. Kuo, C. and W. Lan, *Gel spinning of synthetic polymer fibres*, in *Advances in filament yarn spinning of textiles and polymers*. 2014, Elsevier. p. 100-112.
160. Chouhan, D.K., et al., *Laponite-graphene oxide hybrid particulate filler enhances mechanical properties of cross-linked epoxy.* Journal of Polymer Research, 2018. **25**(2): p. 1-12.
161. Golafshan, N., et al., *Nanohybrid hydrogels of laponite: PVA-Alginate as a potential wound healing material.* Carbohydrate polymers, 2017. **176**: p. 392-401.
162. Du, J., et al., *A facile approach to prepare strong poly (acrylic acid)/LAPONITE® ionic nanocomposite hydrogels at high clay concentrations.* RSC advances, 2015. **5**(74): p. 60152-60160.
163. Baniasadi, M. and M. Minary-Jolandan, *Alginate-collagen fibril composite hydrogel.* Materials, 2015. **8**(2): p. 799-814.
164. Hajjarian, Z., et al., *Laser speckle rheology for evaluating the viscoelastic properties of hydrogel scaffolds.* Scientific reports, 2016. **6**(1): p. 1-12.
165. Megone, W., N. Roohpour, and J. Gautrot, *Impact of surface adhesion and sample heterogeneity on the multiscale mechanical characterisation of soft biomaterials.* Scientific reports, 2018. **8**(1): p. 1-10.
166. Xue, Y., et al., *Synthesis of hyaluronic acid hydrogels by crosslinking the mixture of high-molecular-weight hyaluronic acid and low-molecular-weight hyaluronic acid with 1, 4-butanediol diglycidyl ether.* RSC Advances, 2020. **10**(12): p. 7206-7213.

167. Utech, S. and A.R. Boccaccini, *A review of hydrogel-based composites for biomedical applications: enhancement of hydrogel properties by addition of rigid inorganic fillers.* Journal of materials science, 2016. **51**(1): p. 271-310.
168. Aray, Y., et al., *Electrostatics for exploring the nature of water adsorption on the laponite sheets' surface.* The Journal of Physical Chemistry B, 2003. **107**(34): p. 8946-8952.
169. Kamshad, M., et al., *Use of spectroscopic and zeta potential techniques to study the interaction between lysozyme and curcumin in the presence of silver nanoparticles at different sizes.* Journal of Biomolecular Structure and Dynamics, 2019. **37**(8): p. 2030-2040.
170. Hosseini, F., et al., *Bentonite nanoclay-based drug-delivery systems for treating melanoma.* Clay Minerals, 2018. **53**(1): p. 53-63.
171. Li, J. and D.J. Mooney, *Designing hydrogels for controlled drug delivery.* Nature Reviews Materials, 2016. **1**(12): p. 1-17.
172. Wang, C., et al., *An injectable heparin-Laponite hydrogel bridge FGF4 for spinal cord injury by stabilizing microtubule and improving mitochondrial function.* Theranostics, 2019. **9**(23): p. 7016.
173. San Román, M.S., et al., *Drug release from layered double hydroxides and from their polylactic acid (PLA) nanocomposites.* Applied clay science, 2013. **71**: p. 1-7.
174. Tammaro, L., et al., *Incorporation of active nano-hybrids into poly (ε-caprolactone) for local controlled release: antifibrinolytic drug.* Applied Clay Science, 2009. **43**(3-4): p. 350-356.
175. Xu, Q., et al., *Injectable hyperbranched poly (β-amino ester) hydrogels with on-demand degradation profiles to match wound healing processes.* Chemical science, 2018. **9**(8): p. 2179-2187.
176. Ullm, S., et al., *Biocompatibility and inflammatory response in vitro and in vivo to gelatin-based biomaterials with tailorable elastic properties.* Biomaterials, 2014. **35**(37): p. 9755-9766.
177. Amer, L.D. and S.J. Bryant, *The in vitro and in vivo response to MMP-sensitive poly (ethylene glycol) hydrogels.* Annals of biomedical engineering, 2016. **44**(6): p. 1959-1969.
178. Vandooren, J., et al., *Gelatin degradation assay reveals MMP-9 inhibitors and function of O-glycosylated domain.* World journal of biological chemistry, 2011. **2**(1): p. 14.
179. Laronha, H. and J. Caldeira, *Structure and function of human matrix metalloproteinases.* Cells, 2020. **9**(5): p. 1076.
180. Piluso, S., A. Lendlein, and A.T. Neffe, *Enzymatic action as switch of bulk to surface degradation of clicked gelatin-based networks.* Polymers for Advanced Technologies, 2017. **28**(10): p. 1318-1324.
181. Camci-Unal, G., et al., *Synthesis and characterization of hybrid hyaluronic acid-gelatin hydrogels.* Biomacromolecules, 2013. **14**(4): p. 1085-1092.
182. Erndt-Marino, J.D., et al., *In vitro evaluation of a basic fibroblast growth factor-containing hydrogel toward vocal fold lamina propria scar treatment.* Journal of Biomedical Materials Research Part B: Applied Biomaterials, 2018. **106**(3): p. 1258-1267.
183. Li, L., et al., *Tissue engineering-based therapeutic strategies for vocal fold repair and regeneration.* Biomaterials, 2016. **108**: p. 91-110.
184. Graupp, M., et al., *The unsolved chapter of vocal fold scars and how tissue engineering could help us solve the problem.* European Archives of Oto-Rhino-Laryngology, 2016. **273**(9): p. 2279-2284.

185. Topuz, F., et al., *Nanosilicate embedded agarose hydrogels with improved bioactivity.* Carbohydrate polymers, 2018. **201**: p. 105-112.
186. Li, M., et al., *Wrinkling non-spherical particles and its application in cell attachment promotion.* Scientific reports, 2016. **6**(1): p. 1-9.
187. Topuz, F., et al., *One-step fabrication of biocompatible multifaceted nanocomposite gels and nanolayers.* Biomacromolecules, 2017. **18**(2): p. 386-397.
188. Liu, Y., et al., *Injectable dopamine-modified poly (ethylene glycol) nanocomposite hydrogel with enhanced adhesive property and bioactivity.* ACS applied materials & interfaces, 2014. **6**(19): p. 16982-16992.
189. Cheng, F. and J.E. Eriksson, *Intermediate filaments and the regulation of cell motility during regeneration and wound healing.* Cold Spring Harbor perspectives in biology, 2017. **9**(9): p. a022046.
190. Misra, S., et al., *Interactions between hyaluronan and its receptors (CD44, RHAMM) regulate the activities of inflammation and cancer.* Frontiers in immunology, 2015. **6**: p. 201.
191. Kwon, M.Y., et al., *Influence of hyaluronic acid modification on CD44 binding towards the design of hydrogel biomaterials.* Biomaterials, 2019. **222**: p. 119451.
192. Bhattacharya, D., et al., *Impact of structurally modifying hyaluronic acid on CD44 interaction.* Journal of Materials Chemistry B, 2017. **5**(41): p. 8183-8192.
193. Mantovani, A., et al., *The chemokine system in diverse forms of macrophage activation and polarization.* Trends in immunology, 2004. **25**(12): p. 677-686.
194. Ouyang, W., et al., *Regulation and functions of the IL-10 family of cytokines in inflammation and disease.* Annual review of immunology, 2011. **29**: p. 71-109.
195. Edwards, J.P., et al., *Biochemical and functional characterization of three activated macrophage populations.* Journal of leukocyte biology, 2006. **80**(6): p. 1298-1307.
196. Ferrer, R.A., et al., *Dermal fibroblasts promote alternative macrophage activation improving impaired wound healing.* Journal of Investigative Dermatology, 2017. **137**(4): p. 941-950.
197. Yuan, A., et al., *Opposite effects of M1 and M2 macrophage subtypes on lung cancer progression.* Scientific reports, 2015. **5**(1): p. 1-12.
198. Moen, E., et al., *Deep learning for cellular image analysis.* Nature methods, 2019. **16**(12): p. 1233-1246.
199. Tamrin, M.O. and M. Cheriet. *Simultaneous detection of regular patterns in ancient manuscripts using GAN-Based deep unsupervised segmentation*. in *International Conference on Pattern Recognition*. 2021. Springer.
200. Mokarram, N., et al., *Effect of modulating macrophage phenotype on peripheral nerve repair.* Biomaterials, 2012. **33**(34): p. 8793-8801.
201. Hu, Z., et al., *Immunomodulatory ECM-like microspheres for accelerated bone regeneration in diabetes mellitus.* ACS applied materials & interfaces, 2018. **10**(3): p. 2377-2390.
202. Gower, R.M., et al., *Modulation of leukocyte infiltration and phenotype in microporous tissue engineering scaffolds via vector induced IL-10 expression.* Biomaterials, 2014. **35**(6): p. 2024-2031.
203. Jain, S., T.-H. Tran, and M. Amiji, *Macrophage repolarization with targeted alginate nanoparticles containing IL-10 plasmid DNA for the treatment of experimental arthritis.* Biomaterials, 2015. **61**: p. 162-177.

204. Holladay, C.A., et al., *Recovery of cardiac function mediated by MSC and interleukin-10 plasmid functionalised scaffold.* Biomaterials, 2012. **33**(5): p. 1303-1314.
205. Heris, H.K., et al., *Investigation of the viability, adhesion, and migration of human fibroblasts in a hyaluronic acid/gelatin microgel‐reinforced composite hydrogel for vocal fold tissue regeneration.* Advanced healthcare materials, 2016. **5**(2): p. 255-265.
206. Latifi, N., et al., *A tissue-mimetic nano-fibrillar hybrid injectable hydrogel for potential soft tissue engineering applications.* Scientific reports, 2018. **8**(1): p. 1-18.
207. Tomás, H., C.S. Alves, and J. Rodrigues, *Laponite®: A key nanoplatform for biomedical applications?* Nanomedicine: Nanotechnology, Biology and Medicine, 2018. **14**(7): p. 2407-2420.
208. Dawson, J.I., et al., *Clay gels for the delivery of regenerative microenvironments.* Advanced Materials, 2011. **23**(29): p. 3304-3308.
209. Dawson, J.I. and R.O. Oreffo, *Clay: new opportunities for tissue regeneration and biomaterial design.* Advanced Materials, 2013. **25**(30): p. 4069-4086.
210. Gaharwar, A.K., et al., *2D nanoclay for biomedical applications: Regenerative medicine, therapeutic delivery, and additive manufacturing.* Advanced Materials, 2019. **31**(23): p. 1900332.
211. Ghadiri, M., W. Chrzanowski, and R. Rohanizadeh, *Antibiotic eluting clay mineral (Laponite®) for wound healing application: an in vitro study.* Journal of Materials Science: Materials in Medicine, 2014. **25**(11): p. 2513-2526.
212. Tang, L., et al., *LAPONITE® nanorods regulating degradability, acidic-alkaline microenvironment, apatite mineralization and MC3T3-E1 cells responses to poly (butylene succinate) based bio-nanocomposite scaffolds.* RSC advances, 2018. **8**(20): p. 10794-10805.
213. Yoon, H.J., et al., *Cold water fish gelatin methacryloyl hydrogel for tissue engineering application.* PloS one, 2016. **11**(10): p. e0163902.
214. Zhu, M., et al., *Gelatin methacryloyl and its hydrogels with an exceptional degree of controllability and batch-to-batch consistency.* Scientific reports, 2019. **9**(1): p. 1-13.
215. Sun, M., et al., *Synthesis and properties of gelatin methacryloyl (GelMA) hydrogels and their recent applications in load-bearing tissue.* Polymers, 2018. **10**(11): p. 1290.
216. Bartnikowski, M., *Design and characterisation of scaffolds for osteochondral regeneration*. 2015, Queensland University of Technology.
217. Dicker, K.T., et al., *Hyaluronan: a simple polysaccharide with diverse biological functions.* Acta biomaterialia, 2014. **10**(4): p. 1558-1570.
218. Rios de la Rosa, J.M., et al., *The CD44‐mediated uptake of hyaluronic acid‐based carriers in macrophages.* Advanced healthcare materials, 2017. **6**(4): p. 1601012.
219. Hayward, S.L., C.L. Wilson, and S. Kidambi, *Hyaluronic acid-conjugated liposome nanoparticles for targeted delivery to CD44 overexpressing glioblastoma cells.* Oncotarget, 2016. **7**(23): p. 34158.
220. Auzenne, E., et al., *Hyaluronic acid-paclitaxel: antitumor efficacy against CD44 (+) human ovarian carcinoma xenografts.* Neoplasia, 2007. **9**(6): p. 479-486.
221. Cai, Y., et al., *A hyaluronic acid-based hydrogel enabling CD44-mediated chondrocyte binding and gapmer oligonucleotide release for modulation of gene expression in osteoarthritis.* Journal of Controlled Release, 2017. **253**: p. 153-159.

222. Kazemirad, S., H.K. Heris, and L. Mongeau, *Viscoelasticity of hyaluronic acid-gelatin hydrogels for vocal fold tissue engineering.* Journal of Biomedical Materials Research Part B: Applied Biomaterials, 2016. **104**(2): p. 283-290.
223. Choi, K.Y., et al., *Hyaluronic acid–based activatable nanomaterials for stimuli-responsive imaging and therapeutics: beyond CD44-mediated drug delivery.* Advanced Materials, 2019. **31**(34): p. 1803549.
224. Taheri, S., et al., *Injectable, Pore-Forming, Perfusable Double-Network Hydrogels Resilient to Extreme Biomechanical Stimulations.* Advanced Science, 2022. **9**(2): p. 2102627.
225. Chen, H., et al., *Strong fish gelatin hydrogels double crosslinked by transglutaminase and carrageenan.* Food Chemistry, 2022. **376**: p. 131873.
226. Ohno, S., et al., *Transforming growth factor β3 for the prevention of vocal fold scarring.* The Laryngoscope, 2012. **122**(3): p. 583-589.
227. Chen, X. and S.L. Thibeault, *Biocompatibility of a synthetic extracellular matrix on immortalized vocal fold fibroblasts in 3-D culture.* Acta biomaterialia, 2010. **6**(8): p. 2940-2948.
228. Asghari Sana, F., et al., *Spreading, proliferation and differentiation of human dental pulp stem cells on chitosan scaffolds immobilized with RGD or fibronectin.* Cytotechnology, 2017. **69**(4): p. 617-630.
229. Su, K. and C. Wang, *Recent advances in the use of gelatin in biomedical research.* Biotechnology letters, 2015. **37**(11): p. 2139-2145.
230. Annabi, N., et al., *Engineering a sprayable and elastic hydrogel adhesive with antimicrobial properties for wound healing.* Biomaterials, 2017. **139**: p. 229-243.
231. Agarwal, T., et al., *Gelatin/carboxymethyl chitosan based scaffolds for dermal tissue engineering applications.* International journal of biological macromolecules, 2016. **93**: p. 1499-1506.
232. Saha, R., et al., *A bilayered skin substitute developed using an eggshell membrane crosslinked gelatin–chitosan cryogel.* Biomaterials Science, 2021. **9**(23): p. 7921-7933.
233. Lim, C., D.S. Hwang, and D.W. Lee, *Intermolecular interactions of chitosan: Degree of acetylation and molecular weight.* Carbohydrate Polymers, 2021. **259**: p. 117782.
234. Whu, S.W., et al., *In vitro and in vivo evaluation of chitosan–gelatin scaffolds for cartilage tissue engineering.* Materials Science and Engineering: C, 2013. **33**(5): p. 2855-2863.
235. Vold, I.M. and B.E. Christensen, *Periodate oxidation of chitosans with different chemical compositions.* Carbohydrate research, 2005. **340**(4): p. 679-684.
236. Zhang, S., et al., *A novel corneal adhesive based on functionally coupled PEG-lysozyme hydrogel for wound closure after surgical eye surgery.* Chinese Chemical Letters, 2022.
237. Ma, Z., G. Bao, and J. Li, *Multifaceted design and emerging applications of tissue adhesives.* Advanced Materials, 2021. **33**(24): p. 2007663.
238. Fernandez, J.G., et al., *Direct bonding of chitosan biomaterials to tissues using transglutaminase for surgical repair or device implantation.* Tissue Engineering Part A, 2017. **23**(3-4): p. 135-142.
239. Bao, G., et al., *Ionotronic Tough Adhesives with Intrinsic Multifunctionality.* ACS Applied Materials & Interfaces, 2021. **13**(31): p. 37849-37861.
240. Yang, J., R. Bai, and Z. Suo, *Topological adhesion of wet materials.* Advanced Materials, 2018. **30**(25): p. 1800671.

241. Huang, W.C., et al., *A Biodegradable Multifunctional Film as a Tissue Adhesive for Instant Hemostasis and Wound Closure.* Macromolecular Rapid Communications, 2022: p. 2200031.
242. Mehdizadeh, M. and J. Yang, *Design strategies and applications of tissue bioadhesives.* Macromolecular bioscience, 2013. **13**(3): p. 271-288.
243. Pan, M., et al., *Porous chitosan microspheres containing zinc ion for enhanced thrombosis and hemostasis.* Materials Science and Engineering: C, 2018. **85**: p. 27-36.
244. Aguilar, A., et al., *Application of chitosan in bone and dental engineering.* Molecules, 2019. **24**(16): p. 3009.
245. Ma, Y., et al., *Liquid bandage harvests robust adhesive, hemostatic, and antibacterial performances as a first-aid tissue adhesive.* Advanced Functional Materials, 2020. **30**(39): p. 2001820.
246. Tylek, T., et al., *Precisely defined fiber scaffolds with 40 μm porosity induce elongation driven M2-like polarization of human macrophages.* Biofabrication, 2020. **12**(2): p. 025007.
247. Almeida, C.R., et al., *Impact of 3-D printed PLA-and chitosan-based scaffolds on human monocyte/macrophage responses: unraveling the effect of 3-D structures on inflammation.* Acta biomaterialia, 2014. **10**(2): p. 613-622.
248. Guangyu Bao, Q.G., Massimo Cau, Nabil Ali-Mohamad, Mitchell Strong, Shuaibing Jiang, Zhen Yang, Amin Valiei, Zhenwei Ma, Marco Amabili, Zu-Hua Gao, Luc Mongeau, Christian Kastrup, Jianyu Li, *Liquid-infused microstructured bioadhesives halt non-compressible hemorrhage.* Nature Communications, 2022.
249. Li, J., et al., *Tough adhesives for diverse wet surfaces.* Science, 2017. **357**(6349): p. 378-381.
250. Dai, T., et al., *Chitosan preparations for wounds and burns: antimicrobial and wound-healing effects.* Expert review of anti-infective therapy, 2011. **9**(7): p. 857-879.
251. Ravanbakhsh, H., et al., *Carbon nanotube composite hydrogels for vocal fold tissue engineering: biocompatibility, rheology, and porosity.* Materials Science and Engineering: C, 2019. **103**: p. 109861.
252. Wang, L., et al., *UV-crosslinkable and thermo-responsive chitosan hybrid hydrogel for NIR-triggered localized on-demand drug delivery.* Carbohydrate Polymers, 2017. **174**: p. 904-914.
253. Bao, G., *Biofabrication in Tissue Engineering.* Racing for the Surface, 2020: p. 289-312.
254. Chiu, Y.-L., et al., *pH-triggered injectable hydrogels prepared from aqueous N-palmitoyl chitosan: in vitro characteristics and in vivo biocompatibility.* Biomaterials, 2009. **30**(28): p. 4877-4888.
255. Monette, A., et al., *Chitosan thermogels for local expansion and delivery of tumor-specific T lymphocytes towards enhanced cancer immunotherapies.* Biomaterials, 2016. **75**: p. 237-249.
256. Mahmoudzadeh, M., et al., *Physicochemical, pharmaceutical and biological approaches toward designing optimized and efficient hydrophobically modified chitosan-based polymeric micelles as a nanocarrier system for targeted delivery of anticancer drugs.* Journal of Drug Targeting, 2013. **21**(8): p. 693-709.
257. Sandhu, S.V., et al., *Collagen in health and disease.* Journal of Orofacial research, 2012: p. 153-159.

258. Nikkhah, M., et al., *Gelatin‐based biomaterials for tissue engineering and stem cell bioengineering.* Biomaterials from nature for advanced devices and therapies, 2016: p. 37-62.
259. Koudehi, M.F., et al., *Preparation and evaluation of novel nano-bioglass/gelatin conduit for peripheral nerve regeneration.* Journal of Materials Science: Materials in Medicine, 2014. **25**(2): p. 363-373.
260. Ito, A., et al., *Transglutaminase-mediated gelatin matrices incorporating cell adhesion factors as a biomaterial for tissue engineering.* Journal of bioscience and bioengineering, 2003. **95**(2): p. 196-199.
261. Echave, M.C., et al., *Recent advances in gelatin-based therapeutics.* Expert opinion on biological therapy, 2019. **19**(8): p. 773-779.
262. Yung, C., et al., *Transglutaminase crosslinked gelatin as a tissue engineering scaffold.* Journal of Biomedical Materials Research Part A: An Official Journal of The Society for Biomaterials, The Japanese Society for Biomaterials, and The Australian Society for Biomaterials and the Korean Society for Biomaterials, 2007. **83**(4): p. 1039-1046.
263. Liu, Y., et al., *Tunable physical and mechanical properties of gelatin hydrogel after transglutaminase crosslinking on two gelatin types.* International journal of biological macromolecules, 2020. **162**: p. 405-413.
264. Meng, Q., et al., *Transglutaminase orthologues in medaka fish-biochemical characterization and establishment of gene-deficient mutants.* Analytical Biochemistry, 2020. **604**: p. 113610.
265. Zhou, X., et al., *Cloning and characterization of a histone deacetylase, HDAC9.* Proceedings of the National Academy of Sciences, 2001. **98**(19): p. 10572-10577.
266. Ahvazi, B., et al., *Three-dimensional structure of the human transglutaminase 3 enzyme: binding of calcium ions changes structure for activation.* The EMBO journal, 2002. **21**(9): p. 2055-2067.
267. Kieliszek, M. and A. Misiewicz, *Microbial transglutaminase and its application in the food industry. A review.* Folia microbiologica, 2014. **59**(3): p. 241-250.
268. Zhu, Y. and J. Tramper, *Novel applications for microbial transglutaminase beyond food processing.* Trends in biotechnology, 2008. **26**(10): p. 559-565.
269. Xu, C., et al., *High‐Strength, Thermally Activated Shape Memory Hydrogels Based on Hydrogen Bonding between MAAc and NVP*. Macromolecular Chemistry and Physics, 2018. **219**(10): p. 1700636.
270. Zhao, Z., et al., *Injectable microfluidic hydrogel microspheres for cell and drug delivery.* Advanced Functional Materials, 2021. **31**(31): p. 2103339.
271. Mealy, J.E., et al., *Injectable granular hydrogels with multifunctional properties for biomedical applications.* Advanced Materials, 2018. **30**(20): p. 1705912.
272. Cheng, W., et al., *Granular hydrogels for 3D bioprinting applications.* View, 2020. **1**(3): p. 20200060.
273. Vasconcelos, D.P., et al., *Macrophage polarization following chitosan implantation.* Biomaterials, 2013. **34**(38): p. 9952-9959.
274. Fong, D. and C.D. Hoemann, *Chitosan immunomodulatory properties: perspectives on the impact of structural properties and dosage*. 2017, Future Science. p. FSO225.